A Theoretical Analysis on Magnetic Control Systems in Aircraft, and Spacecraft

a project presented to
The Faculty of the Department of Aerospace Engineering
San Jose State University

in partial fulfillment of the requirements for the degree

Master of Science in Aerospace Engineering

by

Tomoaki M. Clark

March 2024

approved by

Dr Periklis Papadopoulos

Faculty Advisor

ABSTRACT

This project explores the feasibility and advantages of integrating magnetic actuators and controllers into modern aircraft control systems, offering a novel alternative to conventional and electromechanical mechanisms. Traditional systems, while advanced, remain susceptible to hardware failures, software glitches, and environmental disturbances that compromise reliability and safety. By employing electromagnetic control elements, this project proposes a solution that enhances input precision, reduces failure points, and improves response time. Detailed analytical methods were employed, including the derivation of an aircraft's equations of motion based on Newton's laws, which incorporate both translational and rotational dynamics alongside aerodynamic stability parameters and a comprehensive six-degrees-of-freedom model. These equations were subsequently linearized using a perturbation model and implemented in MATLAB for simulation strict flight conditions.

A baseline control system was established using a combination of PID, LQR, and dynamic inversion controllers to regulate the aileron, rudder, and elevator responses. Following system optimization, magnetic controllers were integrated into the simulation framework, with parameters systematically tailored for each control surface, yielding demonstrable improvements in system responsiveness and stabilization time. Recent literature further supports the potential of magnetic actuation, highlighting reduced system weight, enhanced durability, and superior precision compared to traditional control methods, a trend increasingly noted in both manned and unmanned aerial vehicle applications. This project extends that research by not only validating the theoretical benefits through simulation but also by addressing the practical challenges of physical implementation.

In addition to simulation-based validation, the study discusses the importance of high-fidelity testing methodologies such as wind tunnel experiments and high-altitude performance simulations, which are critical for confirming the real-world applicability of magnetic control systems. Future work is outlined to include the development of scaled prototypes and comprehensive dynamic testing environments to rigorously assess system performance under varied operational conditions. By providing a solid theoretical foundation coupled with promising simulation results, this research establishes a viable pathway for the integration of magnetic actuators into aerospace control systems, potentially revolutionizing aircraft safety, efficiency, and overall design innovation.

Acknowledgements

I would like to acknowledge family members and close friends whom I have lost along the way towards completing my Master of Science in Aerospace Engineering. Family and friends, such as Shigeru Suzuki, my grandfather, for inspiring me to pursue my passion in aeronautical aircraft and spacecrafts, and Alberto Rodriguez, one of many close friends, whose drive and influence for leadership pushed me to reach for my goals and dreams. I would like to thank San Jose State University for gifting me this opportunity to explore my interests in the field of aerospace engineering.

Table of Contents

List of Tables

List of Figures

List of Symbols

ϕ= Roll Angle β=Side Slip Angle p = Roll Rate r = Yaw Rate ψ= Heading Angle δr= Rudder Deflection $\delta\alpha$= Aileron Deflection

Yr= Side Force due to Yaw rate
Yp= Side Force due to roll rate
g=Gravitational Acceleration
θ= Pitch Angle q = Pitch Rate

General

h= Altitude
M= Mach Number
U_1 = Velocity of Aircraft
P_{dyn}= Dynamic Pressure
W= Weight
S= Wing Area
b= Wing Span
c= Chord length

x_c= Position of Center of Gravity
α_{trim}= Trim Angle of Attack
I_{xx}= X axis Moment of Inertia
I = Y-axis Moment of Inertia
I_{zz}= Z axis Moment of Inertia
I_{xz}= X-Z plane Moment of Inertia

Longitudinal Derivatives

X_u= Thrust Force due to Velocity
X_α= Thrust Force due to Angle of Attack
Z_u= Downwards force due to Velocity
Z_α= Downwards Force due to Angle of Attack
M_u= Pitch Moment due to Velocity
M_α= Pitch Moment due to Angle of Attack
$M_{\dot{\alpha}}$ = Pitch Moment due to Rate of Change of Angle of Attack

M_q = Pitch Moment due to Pitch Rate
$X_{\delta e}$ = Thrust Force due to Elevator Deflection
$Z_{\delta e}$ = Downwards Force due to Elevator Deflection
$Z_{\delta a}$ = Downwards Force due to Aileron Deflection
$M_{\delta e}$ = Pitch Moment due to Elevator Deflection

Lat-Dir Derivatives

Y = Side Force due to Sideslip Angle
L= Rolling Moment due to Sideslip Angle
L_p = Rolling Moment due to Roll Rate
L_r = Rolling Moment due to Yaw Rate
N = Yawing Moment due to Sideslip Angle
N_p = Yawing Moment due to Roll Rate
N_r = Yawing Moment due to Yaw rate
$Y_{\delta r}$ = Side Force due to Rudder Deflection

$L_{\delta r}$= Rolling Moment due to Rudder Deflection
$N_{\delta r}$ = Yawing Moment due to Rudder Deflection
$Y_{\delta a}$ = Side Force due to Aileron Deflection
$L_{\delta a}$ = Rolling Moment due to Aileron Deflection
$N_{\delta a}$ = Yawing Moment due to Aileron Deflection

Chapter 1: Introduction, Literature Review, and Methodology

1.1: Motivation

Modern control mechanisms operate with a collection of mechanical parts such as rods, pulleys, and cables to transmit the pilot's inputs from the control deck to the desired control surfaces. These flight mechanisms, originally designed to be hydromechanical, have over time been improved to implement the use of electric motors, digital computers, and optical cables. These control systems vary from aircraft to other aircrafts, such as helicopters using a tilting rotor to course correct the vehicle to their desired location, along with some aircrafts using weight shifting mechanics, what is commonly seen in these aircrafts are a hybrid of electrical and pneumatic control systems to provide precise feedback to the pilot. These control inputs are both implemented in larger aircraft to boost the control reactions of aircraft by simulated means to improve the actuation and error reduction of the controller output. Though it sems to be a problem that has been mitigated, there are problems such as hardware failures, environmental factors, software glitches and other complexities that can induce the likelihood of unforeseen errors in flight. Many of these problems require continuous monitoring and testing to maintain the reliability and safety of these systems, however using a new type f of control mechanism, this may mitigate many of these problems entirely. This project aims to take the control mechanisms that are often used to another degree by analyzing the use of electro-magnets to accelerate the inputs provided by the controller. This idea of magnetic controls came to mind, as providing an electrical current through magnetic latches allows for an exact precision of inputs that can be toggled directly by the pilot, reducing points of failure, and mitigating any component failure.

1.2 Literature Review

As discussed in the motivation of the project, many aircrafts use fly-by-wire systems. This allows for the pilot's inputs to be converted into signals which are interpreted by the control computers and adjust the actuators to move said control surfaces. Within these control systems there are sensors that automatically adjust and provide tactile feedback to the pilots. In fly-bywire systems, these are conversely converted into electrical signals and enable an automatic adjustment to enhance the performance of the flying vehicle. Redundancy measurements are implemented to prevent critical failures, along with multiple backup systems for a safe flight. For the references reviewed, the implementation of magnetic control systems can be separated into a list below:

- Direct actuator control with magnets
- Magnetic Suspension systems
- Magnetic Propulsion Systems
- Thermal Implementation of magnetic controls
- Damping systems with magnetic controls

1.2.1 Direct actuator Control with magnets

To further conduct research on how to implement and analyze magnetic controls in flight systems, prior research must be looked at to come up with an effective approach and proposal to solving this problem. One research article dated as far back as 1990, titled, “A magnetic Attitude Control System for precision pointing of the rolling GP-B spacecraft” published by *Acta Astronautica*. This research paper discusses the development of an algorithm built for magnetic attitude control of a spinning aircraft. This requires a real time measurement of the local magnetic field. To obtain this algorithm a Kalman filter-like estimator is used to obtain the local field by applying a dithering current to the magnetic rods. The algorithm eliminates the need for magnetometers, along with guaranteeing colocation of actuators and sensors, removing points of critical failure for measurements. As a result, the controller achieves a twenty-millisecond pointing accuracy with the algorithm without the need for measurements from the magnetometer.[1] Other forms of literature continue the application of magnets in controls, with a paper published in 2023. This presented an attitude control experiment where the authors introduce angular momentum control law (AMCL) to control a spinning spacecraft system with magnetic torques[2]. It discusses how ACMLS is different from conventional control methods, as it offers simultaneous feedback control for both parameters based on angular momentum error from the desired target. This differs from conventional methods which alternate between regulating the spin rate and spin axis orientation independently. The study delves into analyzing the steady state and asymptotic characteristics of angular momentum error, considering both unsaturated and saturated magnetic moments. A dedicated testbed consisting of magnetic torquers and geomagnetic field simulator, constructed with three Helmholtz coils is used to empirically assess the AMCL’s performance. This replicates a time variant magnetic field like what is experimented in orbit. From there the effectiveness of the AMCL, and the behavior of the testbed is evaluated using two ground experiments focusing on spine rate and spin axis orientation control.[2] The findings are then compared and analyzed against the numerical simulation results, proving the success of the desired spacecraft states. The observed steady-state and asymptotic behaviors viewed align closely with the estimations derived from numerical simulations, and overall demonstrate the capability in appropriately regulating the spin motion of a spacecraft.

Another work discusses the performance of a new magnetic control algorithm for the UPMSat-2 Satellite. This control law is derived from the B-dot methodology, enables the satellite to orient one axis normal to the orbital plane while reaching the specified angular velocity, dispensing the need for attitude determination. The authors assess the performance of this control law using the initial housekeeping data obtained since the satellite’s launch in September of 2020. The control’s operational integrity was validated with data from sun sensors and magnetometers are employed, along with thermal analysis of external satellite temperatures, ensuring adherence to the intended attitude and angular velocity parameters. From there, the experiment concludes with the proposed control law represents a straightforward and efficient alternative to managing small satellite attitude.[3] These references each use magnetic control

patterns and uses them to optimize the overall control parameters used for both spacecrafts and aircrafts, however other references use magnets for applications outside of the aerospace industry.

Additional research on direct actuator controls is also conducted, along with the use of permanent magnet synchronous motors (PMSMs) and model reference systems are used in tandem to provide high stability and response. This can be used in electric vehicles, industrial machines, and household appliances, with limitations based on motor sensitivity computational demands and stability. The researchers propose to integrate a Virtual Rotary-Axis High Frequency Signal Injection and a feed forward decoupling algorithm to improve their identification accuracy and performance, demonstrating greater stability, less disturbance, and accuracy. This decoupling algorithm has resulted in a similar model that identifies its limitations. Along with the feedforward algorithm providing a four to five percent identification accuracy in sensor-based control and an 8.1 percent increase in sensor less control. This showed that the integration of FFD algorithms provides a comprehensive system which is suitable for real world applications, increases the stability and accuracy in motor and control systems.[15] Another research article provides a three level speed control of an offshore wind turbine system with as little computation as possible; stating that conventional turbine control systems generate large inertia. This is then addressed by adding additional weighing for the torque changes into the cost function improving the performance of control and eliminating integral action. It uses modified switching state formulas based on optimal states reducing iterations from 27 to 7 thus changing the frequency without the constraint. As a result the simulations of a 1.5 MW permanent magnet synchronous generator based wind turbine demonstrates an effective speed control with differing wind profiles and improved performances compared to the conventional control methods, reducing computation, switch optimization and increase in speed prediction of high inertia systems.[16]

1.2.2 Magnetic Suspension systems

One research paper titled “Contactless control of Suspended loads for offshore installations: Proof of Concept using Magnetic Interaction” (2024) provides an implementation of magnetic control systems for motion compensation. This research article discusses the progress of contactless motion compensation by researching a magnetically controlled pendulum. This was invested and researched upon for the current offshore wind turbines being installed and positioned, requiring methods of mechanical equipment attached to lifted components by human interaction. The methods used in the article entails the interplay between the magnetic pendulum and an electromagnetic actuator, with two control modes being considered: the imposition of a desired motion to the mass and lessening the motion from a set pivot simulation. In the paper, the computational model is authenticated and calibrated through experiments and demonstrates the predictive capabilities, along with an effective governance of a broad range of frequencies and amplitudes. The control parameters are identified as they are associated with techniques such as separation distance between magnets and the controller saturation. The regional parameters for

effective control in the experiment depend on the characteristics of the excitation. Along with the force amplitude of the contactless actuator is comparable to the currently used active tugger line control systems. This experiment also provides sources for the added benefit of both attractive and repelling forces. From the paper the discoveries pave the path for further advancement of non-touch control techniques with the potential to enhance productivity of offshore wind turbine installations.[4] Another paper that applies magnets for suspension, discusses control moment gyros (CMG) which is a crucial actuator in spacecraft altitude control for its precision and substantial moment output. For highspeed rotors, magnetically suspended control moment gyros (MSCMG) are used to employ magnetic bearing support and offer frictionless operation, higher precision in operation and extend the lifespan of actuators. During CMG operation the moving gimbal effect causes a rapid increase in power consumption due to increase in control current, hybrid magnetic bearings (HMG) are used to enhance their efficiency using permanent magnets to generate bias magnetic fields and minimizing power consumption. To address this even further, gimbal angular velocity feedforward (GAVF) method, which involves establishing a model of the HMB-rotor system, deflecting the rotor using gimbal angular velocity and HMB stiffness. An adaptive compensation approach based GAVF method is then used to maintain the overall system performance under parameter fluctuations. From this the proposed method effectively reduces the power consumption during moment output, as validated through experimental and simulation results.[5] Another reference that contributes to magnetic suspension is the use of balancing objects and vehicles in a wind tunnel. The Publication by *Experimental Thermal and Fluid Science* discusses the effects of magnetic suspension and balancing system installed on a wind tunnel on a slanted cylinder afterbody. The range of critical Reynolds numbers in the dummy strut used in the first experiment shows that as the Reynolds number decreases, and the variation depends on the location of the strut in the tunnel. The size of the separation bubble and recirculation region changes depending on the location of the strut on the wake of the center plane. Weak vortices were observed to be formed behind the strut in the experiment, changing the wake structure. This change according to the researchers affects the variation of the vortices core wandering, as well as becoming a factor in power spectral density peaks observed in prior studies.

The overall results showed that characteristics in correlation to the critical Reynolds number where the aerodynamic forces and flow field chances significantly. From these results it is suggested that strut support strongly interferes with the flow around the test model and must be carefully considered. From the research its assumed that though there is a magnetic force that interacts with the wake produced in experiments, the effects generated have an overall performance increase when compared to a regular strut support.[6] Analyzing these research papers provides that the results in each paper provide a proof of concept of magnetic support systems that require less human contact and the feedforward system used can be applied to safely control both spacecrafts and aircrafts with little to no points of failure.

1.2.3 Magnetic Propulsion Systems

Next, viewing the propulsive capabilities of magnetic controls, this next paper talks about a special functionality that is viewed in a thin-film soft magnetic strip at an inclined magnetic anisotropy angle, enabling a switching of magnetic domains with a surface normal field with a certain distribution element. The switching occurs between single and multi-domains along with configurations adjacent to narrow strips. The article discusses how the magnetic permeability of AC fields experiences a significant change within the frequency ranges of 10 kHz to 10 MHz as a function of the distributed magnetic field strength. The article investigates the correspondence of alternating current permeability and the magnetic domain as a function of the intensity of the distributed field. This article confirms that as the intensity of the distributed magnetic field increases the Landu-Lifshitz-like multi-domain area, extends on a clustered narrow strip, aligns with the variations of permeability. The results in the article provide a potential application to uses such as a tunable inductor, sensors for memorizing and detecting disturbed magnetic fields generated by nanoparticles, and lastly it can be applied for electromagnetic shielding.[7] Another source applies magnets not to the direct propulsion capabilities, but the implementing a magnetic bearing. This paper presents a magnetic bearing switched reluctance motor (MBSRM) that allows for two degrees of freedom and suspension consisting of a switched reluctance motor as well as an active magnetic bearing. This motor will have a three phased armature windings and biased winding of the active magnetic bearing (ABM) which is simultaneously fed with a modified asymmetric half bridge converter. While in operation, the rotational torque in the SRM and flux creates an electromagnetic force in the active magnetic bearing concurrently. The researchers outline the operational principle and structure of the MBSRM along with the validation and formulation of suspending forces using finite element analysis. The paper additionally details the proposed half bridge converter and presents the simulation which results in both the biased winding and three phase armature windings through magnetic field circuit coupling simulation. The result of this paper shows that after a prototype is developed, and experimental results confirm the feasibility and effectiveness of the converter design.[8] These designs and implementations use the physical application of magnets to improve the performance capabilities of aircrafts however researchers have provided external methods of improving he propulsive capabilities of magnets. Published by *Aerospace Science and Technology* proposes a magnetic controlled inlet design for airbreathing hypersonic vehicles. The report discusses the implementation of electromagnetic source terms to the Euler equations of motion, developing an algorithm coupled with electromagnetic field/hypersonic flow field as a numerical design tool. The authors constructed a quasi-one-dimensional simplified model of the magnetic inlet to examine the performance under different conditions of leading shock angles and magnetic field under compression. From these experiments the researchers found that the combination of a weak leading-edge shock and strong magnetic field can obtain a better effect of compression. Three inlets were designed under the magnetic field with the induction intensity varying between 0.05, 0.08 and 0.1 tesla, allowing for the inlets to have a contraction ratio of about 1.5, and the wall chape being insensitive to the magnetic induction intensity variation. The inlets were tested at an inflow Mach number of 10 and the exit Mach number is reduced to Mach 5 or Mach 2.5,

when the magnetic induction intensity is adjusted from 0.05 to 0.1 tesla. The results presented show that there is no reflected shock in the inner channel of the inlet and the complex shock layer interaction in the inlet is relieved. Lastly the experiment showed that the energy lost in the pressure recovery can be transformed into electrical energy magneto-hydrodynamic generator (MHD) energy extraction equipment, using it to accelerate the overall nozzle flow of the designed inlet.[9] In conclusion with the performance capabilities, we can see that the implementation of inducing magnets, impacts the overall propulsive capabilities of a vehicle moving through a fluid medium at high speeds, where inputs are crucial in moment to moment interactions. This interaction in hypothesis is then increased drastic measure depending on the frequency at which magnets are implemented under higher Mach numbers.

1.2.4 Thermal Implementation of magnetic controls

In research, magnetic systems implemented in aircrafts and spacecrafts have thermal capabilities which affect the thermodynamics of aircrafts in high speeds. One paper discusses the considerable applications, published by *Applied Surface Science* in 2023. This presents a post growth annealing method aimed to manipulate the Curie Temperature and magnetic anisotropy of Cr2Te3 van der Waals ferromagnetic thin films. The as grown Cr2Te3 films display a Curie temperature of approximately 170K with an out of plane magnetic easy axis. However, through high temperature ex-situ x-situ annealing (300 – 400 °C), significant changes occur: the Curie temperature increases notably to around 300 K, and the magnetic easy axis reorients to the inplane direction. Analyses of electronic, chemical, and structural properties indicate that the expansion of the c-axis lattice constant during annealing is responsible for modulating the magnetic properties of the Cr2Te3 film. These findings highlight the efficacy of ex-situ annealing in controlling the magnetic characteristics of van der Waals ferromagnetic thin films. Moreover, the emergence of room temperature ferromagnetic ordering post-annealing, coupled with its resilience to subsequent thermal processes, suggests the potential suitability of Cr2Te3 thin films for applications in spintronic devices based on van der Waals materials.[10] Another source provides another application of magnets in thermal capabilities, where the researchers discovered a considerable applications of magnetohydrodynamic heat shield systems to complex geometries that induce a shock wave or boundary layer interaction associated with high heat loads. The MHD heat shield systems were proven to be highly effective in hypersonic blunt nose bodies, and since it lacked deep research into large size models in high enthalpy conditions the researchers attempted to experiment and apply said systems to modern hypersonic bodies. Partially ionized flows of hollow cylinders and flare coupling of these fields were numerically analyze using a thermochemical nonequilibrium solver to investigate the possibility and mechanism controls. These consisted of eleven species reaction model and a Park two temperature model based on the low magneto-Reynolds assumption. The authors stated that a fully implicit block lower-upper symmetric Gauss-Seidel algorithm was developed to address the numerical stiffness initiated by the large difference in characteristic time of grid refinement and thermochemical non-equilibrium in the boundary layer and interaction medium. This improved the accelerating rate, and the solver was validated using case solving MHD control of flow

around a typical reentry vehicle, as well as the measured hollow cylinder/flare data and double cone for a high enthalpy tunnel. From there a parametric study of high enthalpy flow over a hollow cylinder was experimented and the MHD control was separated into three categories. Ntype control led to the largest reduction in the peak value of total heat flux along a wall surface, obtained by using a uniform magnetic field. This means that the peak heat flux and peak skin friction coefficient was reduced to around twenty percent and forty-eight percent. From there two local MHD interaction parameters were introduced for the purpose of mechanical examination and can function as a reliable gauge for MHD controllability assessment. This shows that the conceptual findings illustrated the Lorentz force acting opposing to the streamline direction, prompted by external magnetic field and ionized flow emerged as a pivotal element affecting local heat flux regulation. In conclusion the outcomes of this experiment establish a groundwork for devising MHD experiment within a high enthalpy wind tunnel test.[11] In these applications, many of these tests can be referred to and applied in a morphing aircraft and applied to nonlinear dynamic traits and interferences associated with shape changing wings.[12]

1.2.5 Damping systems with magnetic controls

Lastly, this reference that was reviewed for this project provides a method of damping using magnets. This article presented by *Mechanical Systems and Signal Processing*, volume 202, discusses the discusses an innovative resolution of a magnetorheological sting support system used to combat the vulnerability of wind flow resonance. Using a combination of Euler Bernoulli Bean and Kelvin-Voigt element, a vibration reduction mechanism is explained and developed, along with the relationship between the stiffness and damping of the magnetorheological damper (MRD), the natural frequency and damping ratio characteristics being illustrated. To control the stiffness and damping feature for the system an annular squeeze feature was implemented in the MRD design accounting for the factors of low influence on sting shape, wind flow, and magnetic circuit requirements. The report also entails the optimizations made to the system considering the target magnetic field and low power consumption as the main objectives. The effectiveness of the structure design and optimization are tested on the manufactured MRD, showing the characteristics that satisfy the vibrational control of the system. The controllability and fail-safe property were then verified through wind tunnel and laboratory tests, along with the on-off control tests conducted in various impulse excitation and a resonance peak attenuated by about twenty-seven decibels, and passively attenuated at seventeen decibels. The experiment showed that magnetorheological sting support is capable of suppressing vibrations effectively.[13] In contrast to the thermal capabilities of magnets in an aircraft, damping capabilities seem to apply modern control mechanisms to magnets to reduce the generated resonance from tests. This application can be applied to not only test equipment such as wind tunnels as discussed, but as well as reduce additional structural vibrations that occur in hypersonic flight.

This next article shows that magnets used in motor systems can be used to control the vibrations using a passive device using shunt damping. This is researched upon to protect against

micro-cracks due to the low flux between the rotor, stator and airgap; researchers are able to model a procedure for electromagnetic shunt damping. The damping forces are generated from a combination of rotor movement providing a magnetic flux, and the electric currents induced in the windings provided by a device, which is then converted into heat energy. The results state that a permanent magnet thickness and several windings turns provides an optimal value of electrical resistance and thus is mathematically proven through simulations.[17] Additionally, a permanent magnet linear synchronous motor can be applied to a precision equipment, and applied to active vibrational absorption systems. Researchers state that the design is important for the special requirements for the response speed, temperature, installation and the bandwidth, and in result, the performance is effectively analyzed in combination with proposed design objectives. [18]

1.2.6 Conclusion

In conclusion to the research, there are more than a handful of applications that magnets have to aircraft, spacecrafts, and objects generating a thermodynamic property. The references provide proof of concept, simulations, and applications of magnets to real life tools and parts that can improve the capabilities of modern controls. Magnetic Actuators provided a direct line of controls applications to the instantaneous response that magnetic controls with a current will generate, along with negating many of the points of failure mechanical controls must deal with. Suspension mechanisms reduce the human error that can occur within both aeronautical and civil works of engineering. Magnetic bearings in motors, in-plane magnetization and magnetically suspended gyros provide an excellent application to propulsive capabilities of magnets, and lastly the thermal capabilities that coincide with the propulsive capabilities, inducing and effecting the shockwave and boundary layer provides additional methods of how magnetic fields impact the overall controllability and performance of a given aircraft.

1.3 Project Proposal

In the industry of aerospace engineering the constant evolution of aircraft and spacecraft performance is an innovation many companies aim to achieve. Based on the prior literature, there are still improvements that can be made in the control technologies of aerial vehicles. One point of interest that is frequently discussed is the integration of magnetic technologies into control systems. Magnetic Actuators offer a potential benefit to aircraft and spacecrafts as they would be lighter than conventional control systems, improved precision, and increased reliability in critical moments. The direction of this project aims to explore the advantages and feasibility of incorporating magnetic control switches and actuators into modern aircraft and spacecraft control systems.

Objectives:

- Investigate existing research on magnetic actuation and the application to aircraft control.
- Design and develop a prototype aircraft control system designated for magnetic actuators.

- Evaluate the reliability, efficiency, and performance of magnetic based control systems through simulation and testing.
- Assess the potential benefits and challenges of implementing magnetic actuators in commercial or military aircraft and spacecrafts.

Methodology:

- Conduct a comprehensive review of academic and industrial literature on magnetic actuation along with its relevance to aircraft control systems.
- Collaborate with professors and advisors to design a prototype aircraft control system incorporating magnetic actuators.
- Develop a functional prototype using advanced modeling and simulation tools using magnetic control systems.
- Perform tests in controlled environments to assess the reliability, efficiency, and overall performance of magnetic actuators, then compare them to traditional control methods.
- Analyze the collected data from testing to determine the advantages and limitations of magnetic actuation in aircraft control systems.

Timeline

This project is estimated to take the current year to conduct, develop, test, and analyze the integration of magnetic control systems. The current expectation of this projected timeline is listed below:

- Development of a prototype control system featuring magnetic actuators
- Comprehensive analysis of the performance and efficiency of magnetic based control systems.
- Identify the potential applications of integrating magnets into control systems.
- Provide insights of the challenges and limitations of implementing said control systems.
- Provide recommendations for further research and development in the field of magnetic actuation for aerospace applications.

Conclusion

Integrating magnetic actuators and controllers into aircrafts systems could potentially revolutionize the aerospace industry. Reducing the weight, improving the precision, and enhancing the reliability of aircraft controls systems with magnets could lead to more efficient and safer aircraft design and controllability. This, if applied correctly would provide a clear path for future exploration of magnetic technologies in the engineering industry creating new innovations for aircraft. In conclusion, this project seeks to explore the potential of magnetic actuators and control systems in aircrafts, aiming to develop a prototype, then evaluate its performance in comparison to traditional control mechanisms. The insight provided from research will contribute to the advancement of aerospace engineering and future developments in aircraft design and technology.

Chapter 2: Prototype Magnetic Aircraft Control System Design

2.1 Introduction

This section of the report will entail the approach of prototyping the design of a magnetic aircraft control system, along with what elements and systems were used to generate the right design approach for the control system. To properly approach the controls design, we need to understand the foundations of modern aircraft controls. In flight, aircraft are meant to be stable, as it will return to a steady state configuration when encountering a perturbation such as a gust of wind, or direct turbulence. The steady state configuration allows for an aircraft to correct and maneuver itself under large changes in the flight orientation. From the steady state configuration, the control system can be tuned by measuring the frequency of the output signal of a neutrally stable system, which is used to set the integral and derivative settings on the controller.

The frequency measurement of the output signal, then tuning it to operate under stable conditions is an example of classical controls, which are still used in modern aircraft to this day. However, using classical control methods alone provides no improvement to modern aircraft, as the cost function of the human or pilot inputs outweigh the total energy required to register said input. With mathematics, this can be solved with a system of equations, which can be linearized to find coefficients to get precise values for tracking the general input of any aircraft, and then applied toa non-linear full tracking system identification (SYS-ID) to optimize the computational method of approach. When analyzing these optimized controller systems, linear quadratic regulators (LQR) are utilized to provide a robust solution to modern aircraft.

Upon analyzing both classical and modern control systems, this has been observed, recorded and improved upon by engineers and designers over the last century. These optimizations of steady flight conditions start with defined system requirements such as a balance of the necessary thrust, drag, lift and weight. Balancing these four conditions allows for an aircraft to have no acceleration when in flight. Due to the purposes of many aircraft being used for different reasons, the conditions of each aircraft are different, and can cause disturbances to how an aircraft is operating. For this portion of the report the prototyping phase, this will account for using modern aircraft control systems and applying magnetic parameters which were listed in previous applications from prior research.

2.2 Problem description

Based on the steady flight conditions listed above, we can design and model a robust control system aimed to ensure stability and performance accounting for disturbances and uncertainties in the system parameter or external disturbances. We know that stability in aircraft exists in two forms: Static stability, and dynamic stability. Static stability depends on the steady state of the aircraft before and after a disturbance and dynamic stability which occurs when the control system corrects the aircraft in operation under external disturbances over a period. External disturbances that affect the stability of an aircraft can occur in all directions, however,

the two primary axes that are measured. These two axes are the longitudinal and lateral directional states, which can be measured, then controlled and optimized with any given flight characteristics of an aircraft.

To optimally design a control system for longitudinal and lateral directions, we can generate a program to view an open loop and closed loop stability analysis where the actuation of each simulated controller is near instant to provide an accurate representation of magnetic controls. For the prototype of the control system an open lop stability analysis is observed as this will determine if the aircraft is stable without any input, meaning the aircraft will return to a steady state condition after acting with a perturbation. From an open loop stability analysis, all aircraft should be longitudinally and laterally stable to ensure a smooth flight and minimize the overall work and or cost of the pilot. Then controllability of the system is determined, designed in association with the desired aircraft and then optimized.

2.3 Computational Controls Set Up

To provide the conditions needed for a control analysis, we will need the translational and rotational equations of motion needed to map the characteristics of a conventional aircraft. We can list the flight parameters needed for an aircraft, using rigid body notations.

- Linear Velocity (m/s): $\vec{V}^{E/B} = Ub_x + Vb_y + Wb_z$ (2.1)
- Angular Velocity(m/s): $\vec{\omega}^{E/B} = Pb_x + Qb_y + Rb_z$ (2.2)
- Aerodynamic Force (N): $F_A = X\hat{b}_x + Y\hat{b}_y + Z\hat{b}_z$ (2.3)
- Thrust Force (N): $\vec{F}_T = X_T\hat{b}_x + Y_T\hat{b}_y + Z_T\hat{b}_z$ (2.4)
- Aerodynamic Moment (N/m): $\vec{M}_A = \mathcal{L}\hat{b}_x + \mathcal{M}\hat{b}_y + \mathcal{N}\hat{b}_z$ (2.5)
- Thrust moment (N/m): $\vec{M}_T = \mathcal{L}_T\hat{b}_x + \mathcal{M}_T\hat{b}_y + \mathcal{N}_T\hat{b}_z$ (2.6)

Here the notation of the cartesian coordinates is represented in the B frame with respect to the Earth. With these parameters we can first define the translational Equations of motion Represented with a rigid body notation.

2.3.1 Translational Equations of Motion

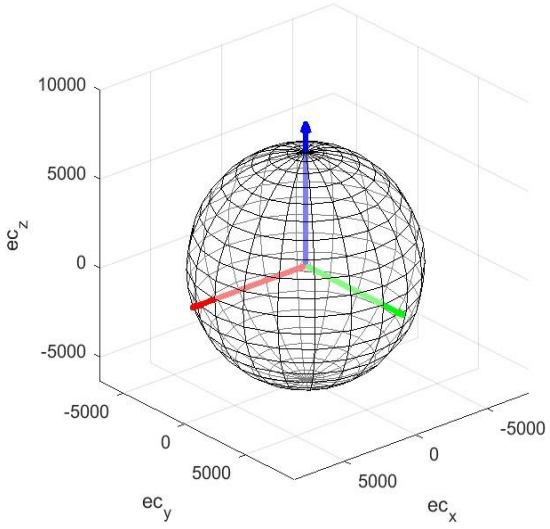

Figure 1:Reference frame of aircraft.

The equations of motion can be broken down with the sum of the forces under a symmetrical body. We can assume that in the diagram, the N frame used for reference to the body frame is the same as the Earth's Reference frame, due to the assumption of a short flight time, as well as mitigating the overall change in mass. Applying Newton's Second law, we can define a summation of forces modeled as so:

$$\sum \overrightarrow{F^B} = \frac{Ed}{dt}\left(mV^{E/B}\right) = m \cdot \frac{Bd}{dt}\left(\vec{V}^{E/B}\right) + \left(\vec{\omega}^{E/B} \times \vec{V}^{E/B}\right) \tag{2.7}$$

The additional component ($\omega^{\rightarrow E/B} \times V^{\rightarrow E/B}$) accounts for the summation of converting the total velocity from the B-frame of the aircraft to the E-frame in symmetry to the motion of the earth. We recall that in the list of parameters there is the linear and rotational velocities defined, thus can substitute the equations 2.1 and 2.2 into equation 2.7 to obtain the sum of the forces.

$$\sum F = m \cdot \left[\begin{bmatrix} \dot{U}_{b_{\hat{x}}} \\ \dot{V}_{b_{\hat{y}}} \\ \dot{W}_{b_{\hat{z}}} \end{bmatrix} + \begin{bmatrix} \hat{b}_x & \hat{b}_y & \hat{b}_z \\ P & Q & R \\ U & V & W \end{bmatrix}\right] \tag{2.8}$$

Where:
$$\begin{bmatrix} \hat{b}_x & \hat{b}_y & \hat{b}_z \\ P & Q & R \\ U & V & W \end{bmatrix} = (QW - RV)\hat{b}_x - (Pw - RU)\hat{b}_y + (PV - QU)\hat{b}_z \tag{2.9}$$

Substituting and combining like terms, we can define translational equations of motion:

$$\hat{b}_x = F_x = m(U + QW - RV)$$

$$\hat{b}_y = F_y = m(V + RU - PW) \tag{2.10}$$

$$\hat{b}_z = F_y = m(W + PV - QU)$$

2.3.2 Rotational Equations of Motion

The rotational equations of motions follow a similar process to the translational motions; however, this is computed with the sum of the moments present in the system, which is defined as so:

$$\sum \vec{M} = \frac{Ed}{dt}\left(\vec{H}^{E/\frac{B}{B_0}}\right) = \frac{Bd}{dt}\left(\vec{H}^{E/\frac{B}{B_0}}\right) + \left(\omega^{E/B} \times H^{E/\frac{B}{B_0}}\right) \tag{2.11}$$

Where H is the angular momentum acting on the body. H can be expressed as the cross product of the moment of inertial and the angular velocity acting from the earth frame to the body frame. Listed as so:

$$\vec{H}^{E/\frac{B}{B_0}} = I \times \omega^{E/B} = \begin{bmatrix} I_{xx} & \cancel{I_{xy}} & I_{xz} \\ \cancel{I_{xy}} & I_{yy} & \cancel{I_{yz}} \\ I_{xz} & \cancel{I_{yz}} & I_{zz} \end{bmatrix} \begin{bmatrix} P \\ Q \\ R \end{bmatrix} \tag{2.12}$$

Separating the cross product into a system of equations we can see that the moment of inertia in the I_{xy} and I_{yz} components are negligible as it is assumed that the aircraft is a symmetrical body, so linearizing the equation with the cross product will be simplified to the equation below:

$$\vec{H}^{E/\frac{B}{B_0}} = (I_{xx}P + I_{xz}R)\hat{b}_x + (I_{yy}Q)\hat{b}_y + (I_{xz}P + I_{zz}R)\hat{b}_z \tag{2.13}$$

$$\left(\omega^{E/B} \times H^{E/\frac{B}{B_0}}\right) = \begin{bmatrix} \hat{b}_x & \hat{b}_y & \hat{b}_z \\ P & Q & R \\ I_{xx}P + I_{xz}R & I_{yy} & I_{xz}P + I_{zz}R \end{bmatrix} \tag{2.14}$$

Once defined we can combine like terms and use the assumption that all inertial terms do not change with time, thus expanding and solving the sum of moments in the system below:

$$\begin{bmatrix} \hat{b}_x \\ \hat{b}_y \\ \hat{b}_z \end{bmatrix} = \begin{bmatrix} M_x \\ M_y \\ M_z \end{bmatrix} = \begin{bmatrix} I_{xx}\dot{P} + I_{xz}\dot{R} + (I_{zz} - I_{yy})QR + I_{xz}PQ \\ I_{yy}\dot{Q} + (I_{xx} - I_{zz})PR + I_{xz}(R^2 - P^2) \\ I_{xz}\dot{P} + I_{zz}\dot{R} + (I_{yy} - I_{xx})PQ - I_{xz}QR \end{bmatrix} \tag{2.15}$$

With the system fully defined, we see that the pitching moment is coupled with the yaw and roll moment of the aircraft. Here we can define these rotational angles using NASA's

standard Euler rotational angles, ψ for yaw angle, Θ for pitch, ϕ for roll each about the $\hat{e_z}$,e_y,& $\hat{e_x}$ frame. Using these angles, we can map out the angular velocity rate with respect to the Euler Angles to obtain the kinematic differential equations.

$$\begin{bmatrix} P \\ Q \\ R \end{bmatrix} = \begin{bmatrix} 1 & 0 & -\sin\theta \\ 0 & \cos\phi & \sin\phi\cos\theta \\ 0 & -\sin\phi & \cos\theta\cos\phi \end{bmatrix} \begin{bmatrix} \phi \\ \dot{\theta} \\ \dot{\psi} \end{bmatrix} \tag{2.16}$$

2.3.4 Linearization

Next after deriving the necessary equations of motion from our parameters. The equations must be linearized to better suit the optimal control system which will be written in the program. To start, a Perturbation equation will be implemented, to model the dynamics of an aircraft with respect to steady state conditions. We can assume these steady state flight conditions are constant thrust, constant altitude (lift is equal to weight), and constant velocity (thrust is equal to drag). We can define these perturbation terms with lowercase variables of the initial parameters, including linear velocity angular velocity, and their rates respectively.

- $U = U_1 + u$, $V = V_1 + v$ $W = W_1 + w$
- $P = P_1 + p$, $Q = Q_1 + q$, $R = R_1 + r$
- $U = U_1 + \dot{u}, V = V\dot{1} + \dot{v}, W = W_1 + \dot{w}$
- $\Psi = \Psi_1 + \psi, \Theta = \Theta_1 + \theta, \Phi = \Phi_1 + \phi$
- $X = X_1 + f_x, Y = Y_1 + f_y, Z = Z_1 + f_z$
- $X_T = X_{T1} + f_{Tx}, Y_T = Y_{T1} + f_{Ty}, Z_T = Z_{T1} + f_{Tz}$
- $L = L_1 + l, M = M_1 + m, N = N_1 + n$
- $L_T = L_{T1} + l_T, M_T = M_{T1} + m_t, N_T = N_{T1} + n_T$

We can substitute the perturbation parameters with the equations of motion along with implementing mathematical assumptions, we can assume that the product two small numbers become negligible, as well as the use of small angle approximations to simplify linear velocity rates. To compute the rest of the linearization of the equations of motion additional Steady flight conditions that are needed for further simplification would be these considerations:

- No steady State Lateral velocity ($V_1=0$)
- No steady state vertical velocity ($W_1=0$)
- No steady state roll angle ($\Phi_1 = 0$)
- No steady state angular velocity ($P_1 = Q_1 = R_1 = \Phi_1 = \Theta_1 = \Psi_1 = 0$)

With these straight flight conditions, we can also assume that the relationship between the linear velocity in the Z axis is related to the product of the angle of attack and the freestream velocity, thus modifying w to include alpha (α). Now the equations above can be simplified to negate a handful of unknown variables, providing a simplified set of equations:

$$(\dot{u}) \; -mg\theta\cos\theta_1 + f_x = m(\dot{u}) \tag{2.17}$$

$$(\dot{w}) \quad -mg\theta(\sin\theta_1)+f_z = mu_1(\dot{\alpha}-q) \tag{2.18}$$

$$m = I_{yy}(\dot{q}) \tag{2.19}$$

$$q = \theta \tag{2.20}$$

2.3.5 Dimensional Stability and Control Derivatives

With the equations of motion simplified, we need to develop the abstract terms such as f_x f_y f_z and so forth, as we want to know what they represent and make them tangible with what affects those terms. These values, to obtain them will need aircraft data such as mass, geometry, and inertial dynamics to clarify their meanings. Looking at equation 2.17.1 for example, we can see that the force f_x is affected by their angle of attack, the thrust, forward velocity, and the elevator deflection. Each of these terms can be defined as derivatives representative of each effect. We can also use the assumption that the dynamic pressure and the wing area on an aircraft remains constant throughout flight. Once computed will provide a frequency representing, the change in X with respect to the free stream velocity:

$$X_u = \frac{1}{m}\frac{dx}{du} = \frac{1}{mU_1}[\vec{q}_1 s(-C_{D_u} - 2C_{D_1})] \tag{2.21}$$

Where $C_{Du}\, and\, C_{Dl}$ represent dynamic coefficients with respect to the speed of sound and the lift of the aircraft respectively, computed with the perturbation method explained above. This calculation can be repeated for X with respect to angle of attack, elevator deflection, on all axis. Lastly these derivative substitutions will also be used to compute the pitching moment equations expressed with their rates and coefficient terms:

$$X_\alpha = \frac{1}{m}\frac{dx}{da} = \frac{1}{m}[\vec{q}_1 s(-C_{D_\alpha} - C_{l_1})] \tag{2.22}$$

$$X_{\delta e} = \frac{1}{m}\frac{dx}{d\delta e} = -\frac{1}{m}[\vec{q}_1 s C_{D_{\delta e}}] \tag{2.23}$$

$$Z_u = \frac{1}{mU_1}[\vec{q}_1 s(-C_{l_u} - 2C_{l_i})] \tag{2.24}$$

$$Z_\alpha = \frac{1}{m}[\vec{q}_1 s(-C_{l_\alpha} - C_{D_l})] \tag{2.25}$$

$$Z_{\delta e} = \frac{-1}{m} C_{l_e} \vec{q}_1 s \tag{2.26}$$

$$Z_{\dot{\alpha}} = \frac{-\vec{q}_1 s\vec{c}}{2mu_1} C_{l_{\dot{\alpha}}} \tag{2.27}$$

$$M_u = \frac{1}{I_{yy}u_1}[\vec{q}_1 s\vec{c}(C_{m_u} + 2C_{m_l})] \tag{2.28}$$

$$M_\alpha = \frac{\vec{q}_1 s\vec{c}}{I_{yy}} C_{M_\alpha} \tag{2.29}$$

$$M_{\dot{\alpha}} = \frac{\vec{q}_1 s\overrightarrow{c^2}}{2I_{yy}u_1} C_{M_{\dot{\alpha}}} \tag{2.30}$$

$$M_q = \frac{\vec{q}_1 s\overrightarrow{c^2}}{2I_{yy}u_1} C_{M_q} \tag{2.31}$$

$$M_{\delta_e} = \frac{\vec{q}_1 s\vec{c}}{I_{yy}} C_{M_{\delta_e}} \tag{2.32}$$

Finally with the stability derivatives defined (2.23-2.32), we can incorporate them into the decoupled equations representative of the rate of airspeed, angle of attack, pitch rate, and roll rate into a summation of equations. Similarly, these calculations can be repeated in the lateral directional equations of motion to obtain the decoupled equations representative of the roll rate, side slip rate, and yaw rate. The equations of motion in state space form are represented below, with the complete computation being referenced at Appendix A.

$$\begin{bmatrix} \dot{u} \\ \dot{\alpha} \\ \dot{q} \\ \dot{\theta} \end{bmatrix} = \begin{bmatrix} X_u & X_\alpha & 0 & -g \\ \frac{Z_u}{U_1} & \frac{Z_\alpha}{U_1} & 1 & 0 \\ \left(M_u + \frac{M_{\dot{\alpha}} Z_u}{U_1}\right) & \left(M_\alpha + \frac{M_{\dot{\alpha}} Z_u}{U_1}\right) & M_q + M_{\dot{\alpha}} & 0 \\ 0 & 0 & 1 & 0 \end{bmatrix} \begin{bmatrix} u \\ \alpha \\ q \\ \theta \end{bmatrix} + \begin{bmatrix} X_{\delta e} \\ \frac{Z_{\delta e}}{U_1} \\ M_{\delta e} + \frac{M_{\dot{\alpha}} Z_{\delta e}}{U_1} \\ 0 \end{bmatrix} \delta_e \tag{2.33}$$

$$\begin{bmatrix} \phi \\ \dot{p} \\ \dot{\beta} \\ \dot{\psi} \end{bmatrix} = \begin{bmatrix} 0 & 1 & 0 & 0 & 0 \\ 0 & L_P & L_\beta & L_r & 0 \\ \frac{g\cos\theta}{u_1} & \frac{Y_p}{u_1} & \frac{Y_\beta}{u_1} & \frac{Y_r}{u_1} - 1 & 0 \\ 0 & N_p & N_\beta & N_r & 0 \\ 0 & 0 & 0 & 1 & 0 \end{bmatrix} \begin{bmatrix} \phi \\ p \\ \beta \\ \psi \end{bmatrix} + \begin{bmatrix} 0 & 0 \\ L_{\delta_r} & L_{\delta_\alpha} \\ \frac{Y_{\delta_r}}{u_1} & \frac{Y_{\delta_\alpha}}{u_1} \\ 0 & 0 \end{bmatrix} \begin{bmatrix} \delta_r \\ \delta_\alpha \end{bmatrix} \tag{2.34}$$

2.4 Open Loop Stability Analysis of Prototype Control System

Providing the stability characteristics of an aircraft can be computed with programming software, which for this instance we will use MATLAB and Simulink to arrange the mathematical derivatives to a state space from that will allow for the necessary inputs of an aircraft, then output matrices to determine both lateral and longitudinal stability. To start, we can define the stability derivatives for designing a generalized control system below:

$$\dot{\vec{x}} = A\vec{x} + B\vec{u} \tag{2.35}$$

$$\vec{y} = C\vec{x} + D\vec{u} \tag{2.36}$$

To define each letter in the stability derivatives, each represents a matrix used to define the control system for easier computations to be done by a computer. For this instance, in the first

equation, the $\dot{x}$ variable represents the overall velocity input of a given aircraft in motion; the letter A represents the stability matrix used to provide which dimensions provide the exact forces in both the longitudinal and lateral directions, multiplied by a one column x vector. B represents the control matrix representing the control variables in the provided direction, along with the product of the u vector. The y equation below, is the output equation of a generalized control system where c is the identity matrix used to compute the initial displacement and simplify the primary output into a single column value. Lastly the D matrix is the feed forward matrix which is represented as a null matrix to optimize the control solution. For the primary input equation, the stability and input matrices are different per direction and can be visualized with a free body diagram for where each direction is represented. Within these matrices the values are obtained with massless values, along with derived values from aircraft calculations.

For each matrix, the stability analysis is divided into two sections: The longitudinal stability analysis, and the lateral directional stability analysis. And for the obtained characteristics of each matrix, we will use the stability characteristics of the Boeing 747 provided by AIAA at sea level conditions.

2.4.1 Aerodynamic and Mass Properties of Conventional Aircrafts

To analyze and input the necessary variables in the stability and control matrices, we will use the standard sea level conditions of the stability characteristics. For each condition, we have the standard sea level measurements of the lift, drag, and deflection angle coefficients to obtain the necessary pole locations for longitudinal and lateral-directional states.

Table 1: aerodynamic coefficients of the Boeing 747

Aerodynamic Coefficient	**Value**	**Aerodynamic Coefficient**	**Value**
C_{L0}	0.29	$C_{y\beta}$	-0.9
C_{D0}	0.0305	$C_{l\beta}$	-0.16
$C_{m\alpha}$	-1.6	$C_{n\beta}$	0.16
$C_{D\alpha}$	0.5	C_{lp}	-0.34
C_{mq}	-25.5	C_{np}	0.13
$C_{L\alpha}$	5.5	C_{lr}	-0.033
$C_{X\delta e}$	0	C_{nr}	-0.033
$C_{Z\delta e}$	0.29	$C_{L\delta a}$	0.014
$C_{m\delta e}$	-1.2	$C_{y\delta\alpha}$	0.0018
C_{yp}	-0.0272	$C_{y\delta r}$	0.118
$C_{n\delta r}$	-0.095	$C_{l\delta r}$	0.008

Table 2: mass and Inertial Parameters of the Boeing 747

Parameter	Value	Parameter	Value
Weight	564,000 lbf	I_{xx}	1.41×10^7 (slug-ft^2)
B	196 ft	I_{yy}	3.05×10^7(slug-ft^2)
$\bar{c}$	27.3 ft	I_{zz}	4.27×10^7(slug-ft^2)

Using these conditions, we can determine the force conditions needed for our state and control matrix, by dividing the necessary parameters with the coefficients to obtain our variables such as thrust force, downwards force, and so forth. Applying these conditions, we can then calculate and compute the longitudinal and lateral directional stability of the aircraft.

$$A_{long} = \begin{bmatrix} -0.0433 & 11.4378 & 0 & -32.1741 \\ -0.0012 & -0.4889 & 1 & 0 \\ 0 & -0.3855 & -0.4356 & 0 \\ 0 & 0 & 1 & 0 \end{bmatrix}$$

$$A_{lat} = \begin{bmatrix} 0 & 1 & 0 & 0 & 0 \\ 0 & -0.9871 & -1.246 & 0.3834 & 0 \\ 0.1456 & 0 & -0.089 & -1 & 0 \\ 0 & -0.1441 & 0.2694 & -0.2338 & 0 \\ 0 & 0 & 0 & 1 & 0 \end{bmatrix}$$

$$B_{long} = \begin{bmatrix} 0 \\ -0.0297 \\ -0.3980 \\ 0 \end{bmatrix}; \; B_{lat} = \begin{bmatrix} 0 & 0 \\ 0 & 0.235 \\ 0.0148 & 0 \\ -0.1655 & -0.0122 \\ 0 & 0 \end{bmatrix}$$

2.4.2 Longitudinal Stability

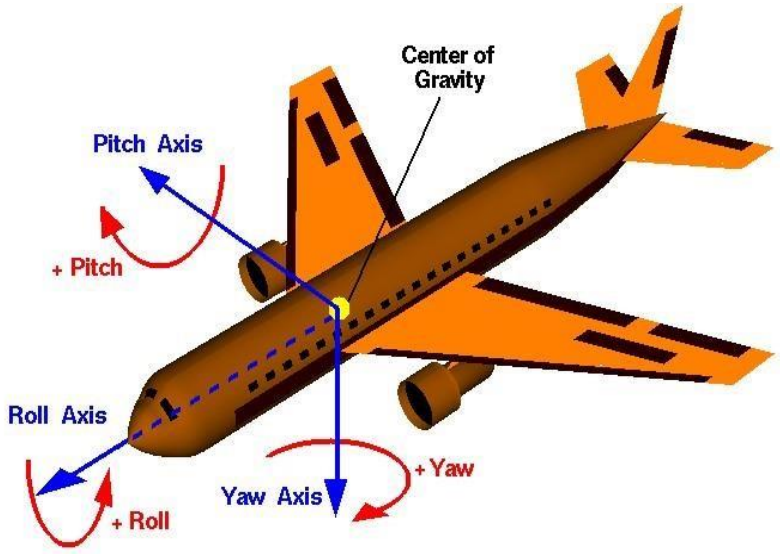

Figure 2: free body diagram of a conventional aircraft with axis and angles (NASA).

To start the stability analysis, the longitudinal measurements of the aircraft will be considered. This represents the motion pitch movement along the aircraft, which is controlled conventionally by an elevator located on the wing. This means that we will need to investigate the change in the angle of attack, pitch angle, pitch rate and speed, as the associated pitch compensation will automatically control the trim angle of the air speed.

$$A = \begin{bmatrix} X_u & X_\alpha & 0 & -g \\ \frac{Z_u}{U_1} & \frac{Z_\alpha}{U_1} & 1 & 0 \\ \left(M_u + \frac{M_\dot{\alpha} Z_u}{U_1}\right) & \left(M_\alpha + \frac{M_\dot{\alpha} Z_u}{U_1}\right) & M_q + M_\alpha & 0 \\ 0 & 0 & 1 & 0 \end{bmatrix} \quad (2.37)$$

$$B = \begin{bmatrix} X_{\delta e} \\ \frac{Z_{\delta e}}{U_1} \\ M_{\delta e} + \frac{M_\dot{\alpha} Z_{\delta e}}{U_1} \\ 0 \end{bmatrix} \quad (2.38)$$

$$\vec{x} = \begin{bmatrix} u \\ \alpha \\ q \\ \theta \end{bmatrix} \quad (2.39)$$

Using MATLAB, we can obtain the eigenvalues of both the long period and short period characteristics of the pole measurements, damping, time constant and frequency. In the program this is computed by calculating the eigen value of the identity matrix C in the output, listed below:

Table 3: longitudinal mode characteristics of the Boeing 747

Pole	Damping	Frequency (rad/sec)	Time constant (sec)
-6.55e-03 + 1.63e-01i	4.01e-02	1.63e-01	1.53e+02

-6.55e-03 - 1.63e-01i	4.01e-02	1.63e-01	1.53e+02
-4.77e-01 + 6.21e-01i	6.09e-01	7.83e-01	2.09e+00
-4.77e-01 - 6.21e-01i	6.09e-01	7.83e-01	2.09e+00

From numerical values provided in the table based on the inputs of the aircraft, we can use MATLAB to convert the state space variables to a transfer function with a command. In the table above we can see that the pole values in all 4 characteristics are negative, meaning that in steady flight the aircraft is fully stable. In computation we can determine the rank of the provided matrices which comes out to a value of five, meaning the transfer function will be a relationship to the fifth order, listed below:

$$G(s) = \frac{-0.1655s^3 - 0.1741s^2 - 0.00781s - 0.03214}{s^5 + 1.31s^4 + 0.6641s^3 + 0.6778s^2 + 0.03037s} \tag{2.40}$$

From the transfer function obtained, we can analyze the overall response of the system with an impulsive input, which is what we need to build a magnetic control system. We can plot these values obtained in MATLAB using an open loop Simulink block diagram to see the impulse and step response of the change phi over the time domain. The block diagram needed for this simulation is displayed below:

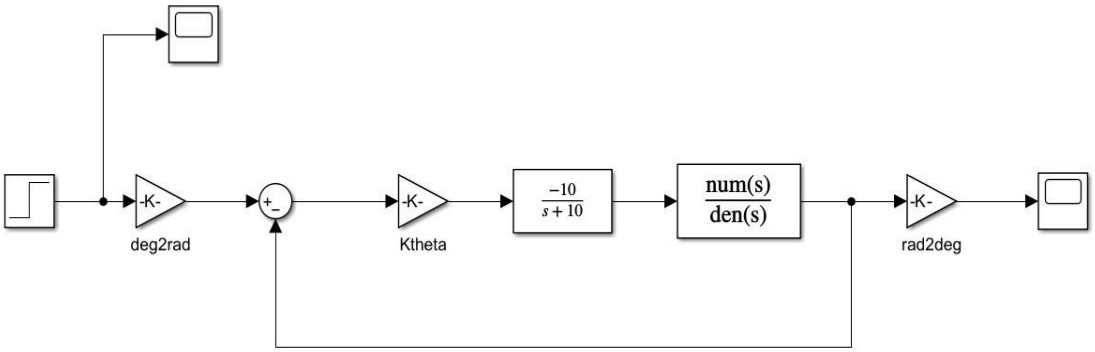

Figure 3: Simulink block diagram of longitudinal stability of the Boeing 747

To view the stability of the aircraft in the longitudinal region, our plot should provide an impulse and step response of the change in theta with the elevator deflection ($\theta(s)/\delta_e(s)$) over time; as well as the change in alpha with the elevator deflection ($\alpha(s)/\delta_e(s)$) over time.

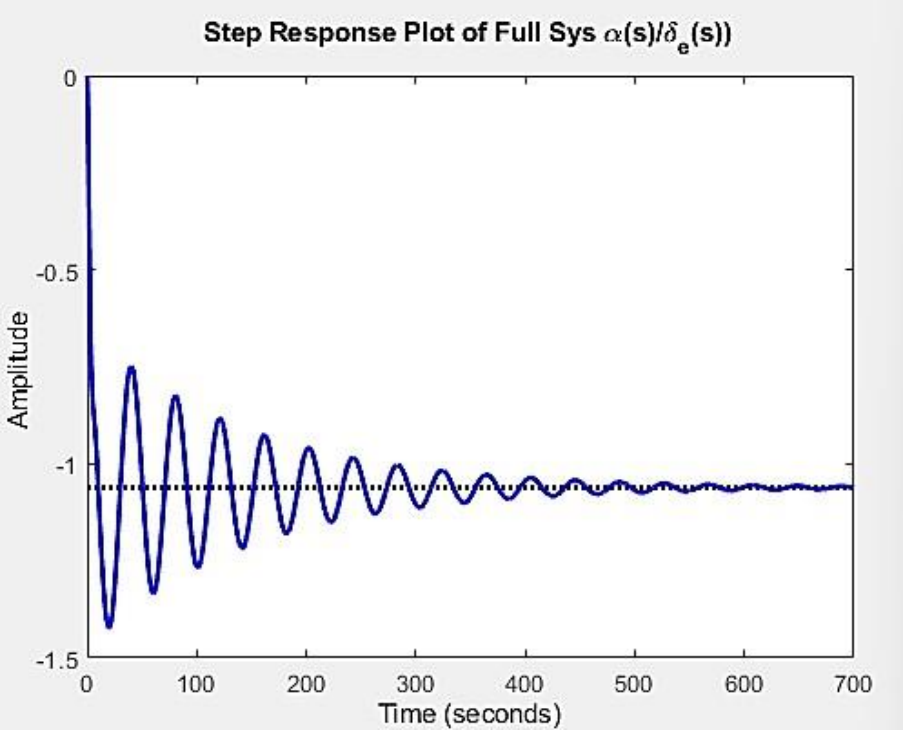

Figure 4: Boeing 747 step response α(s)/δe (s)

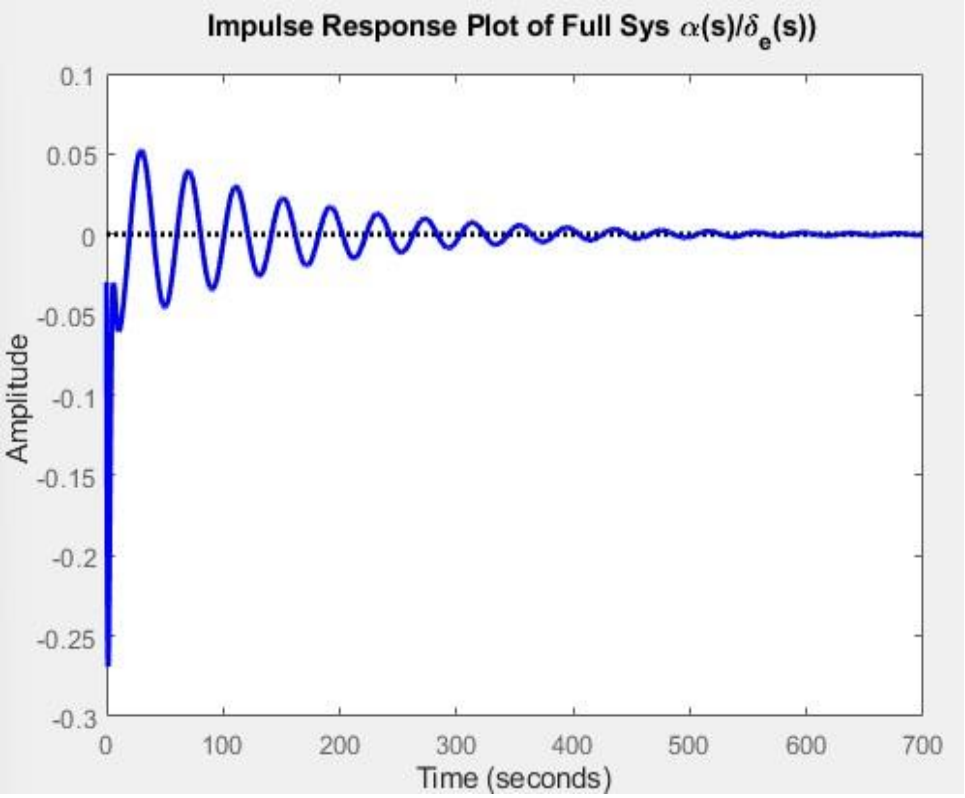

Figure 5: Boeing 747 impulse response α(s)/(δe (s))

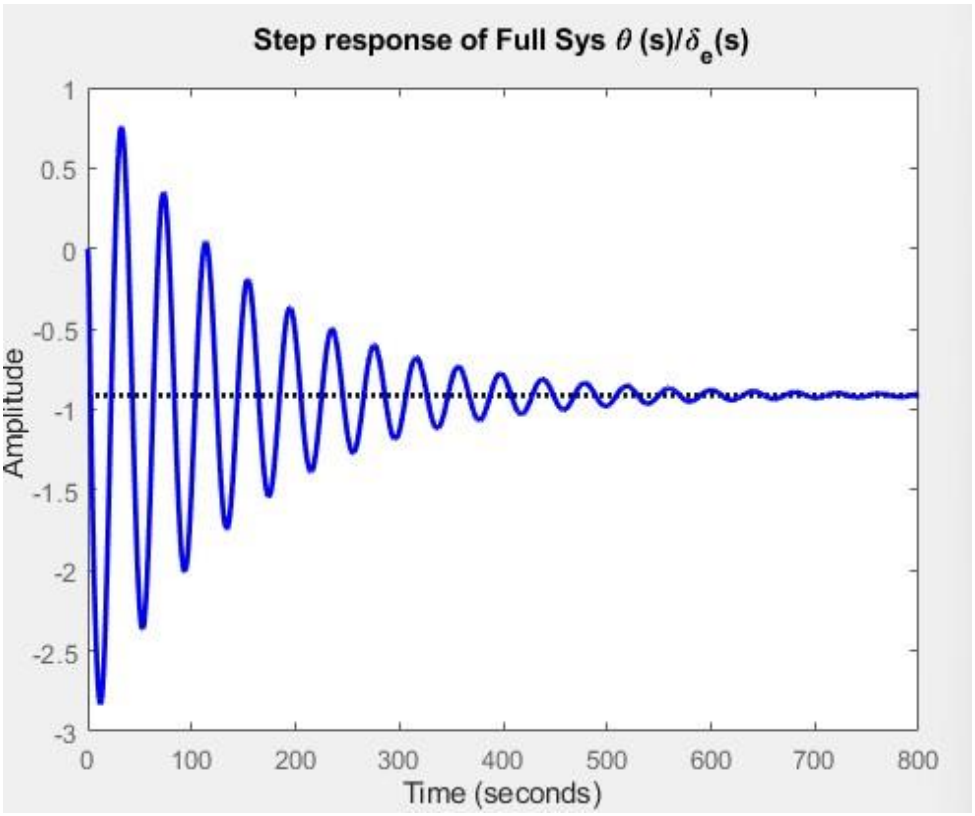

Figure 6: Boeing 747 step response θ(s)/(δe (s))

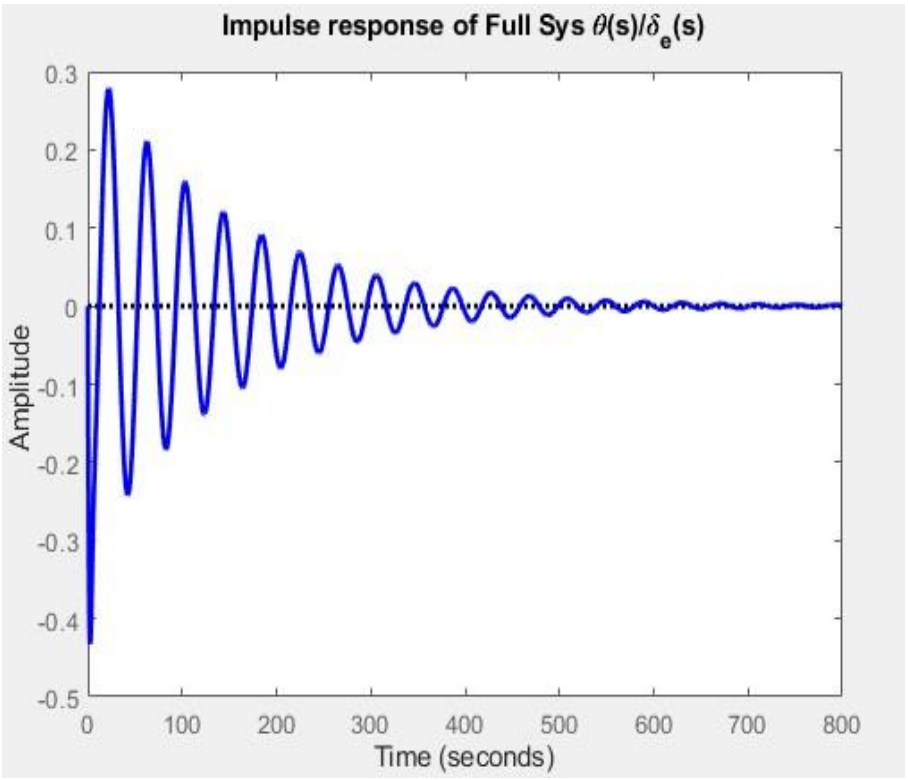

Figure 7: Boeing 747 impulse response θ(s)/(δe (s))

From these plots, we can see that over a period the aircraft is ablet to return to level flight after a step response and an impulse response to the change in elevator deflection. Though it does stabilize, we can see that for the angle of attack it returns to stable flight at around 300 to 400 seconds, the change in the pitch angle takes approximately 500 to 600 seconds to completely stabilize . To optimize the time, it takes to stabilize in flight we will need to build a controller that can shorten the time it takes to return to steady level flight and minimize the oscillations we see in each plot.

2.4.3 Lateral Directional Stability

For this section, lateral movement refers to the motion about the aircraft's rolling or 'x' axis, as well as the directional movement referring to the yaw or 'z' axis of the aircraft. Commonly the rolling axis on an aircraft is controlled by the ailerons while the rudder of an aircraft is responsible for the directional movement. Below are the derived matrices representing the linearized equations of motion for the state space equations:

$$A = \begin{bmatrix} 0 & 1 & 0 & 0 & 0 \\ 0 & L_P & L_\beta & L_r & 0 \\ \frac{g\cos\theta}{u_1} & \frac{Y_p}{u_1} & \frac{Y_\beta}{u_1} & \frac{Y_r}{u_1} - 1 & 0 \\ 0 & N_p & N_\beta & N_r & 0 \\ 0 & 0 & 0 & 1 & 0 \end{bmatrix} \tag{2.41}$$

$$B = \begin{bmatrix} 0 & 0 \\ L_{\delta_r} & L_{\delta_\alpha} \\ \frac{Y_{\delta r}}{u_1} & \frac{Y_{\delta_\alpha}}{u_1} \\ 0 & 0 \end{bmatrix} \tag{2.42}$$

$$\vec{x} = \begin{bmatrix} \phi \\ p \\ \beta \\ \psi \end{bmatrix} \tag{2.43}$$

Table 4: lateral directional mode characteristics of the Boeing 747

Pole	Damping	Frequency (rad/sec)	Time constant (sec)
0e+0	-1.00e+00	0.00e+00	inf
4.68e-02	1.00e+00	4.68e-02	2.14e+01
-2.78e-02 + 7.33e-01i	3.79e-02	7.33e-01	3.60e+01
-2.78e-02 - 7.33e-01i	3.79e-02	7.33e-01	3.60e+01
-1.21e+00	1.00e+00	1.21e+00	8.28e-01

From the characteristic table above, we see that there are some variations in the pole, with most of them being negative, and one being critically stable and one being positive, or unstable

in this case. We computed that the rank of the controllability in this system is also five, meaning that the transfer function will also have a fifth order of magnitude.

$$G(s) = \frac{0.0122s^3 - 0.09134s^2 - 0.008226S + 0.0308}{s^5 + 1.31s^4 + 0.6641s^3 + 0.06778s^2 + 0.03037s} \quad (2.44)$$

Once we obtained the transfer function above, we can now plot the change in the roll angle over the change in the rudder deflection ($\psi(s)/\delta_r(s)$) and the heading angle over the change in aileron deflection ($\phi(s)/\delta_a(s)$) to analyze the lateral directional stability of the aircraft.

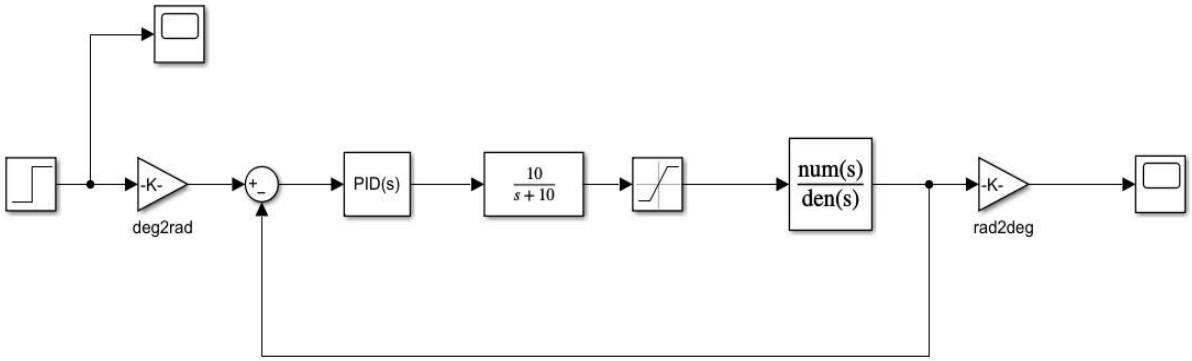

Figure 8: Simulink block diagram of lateral-directional stability of the Boeing 747

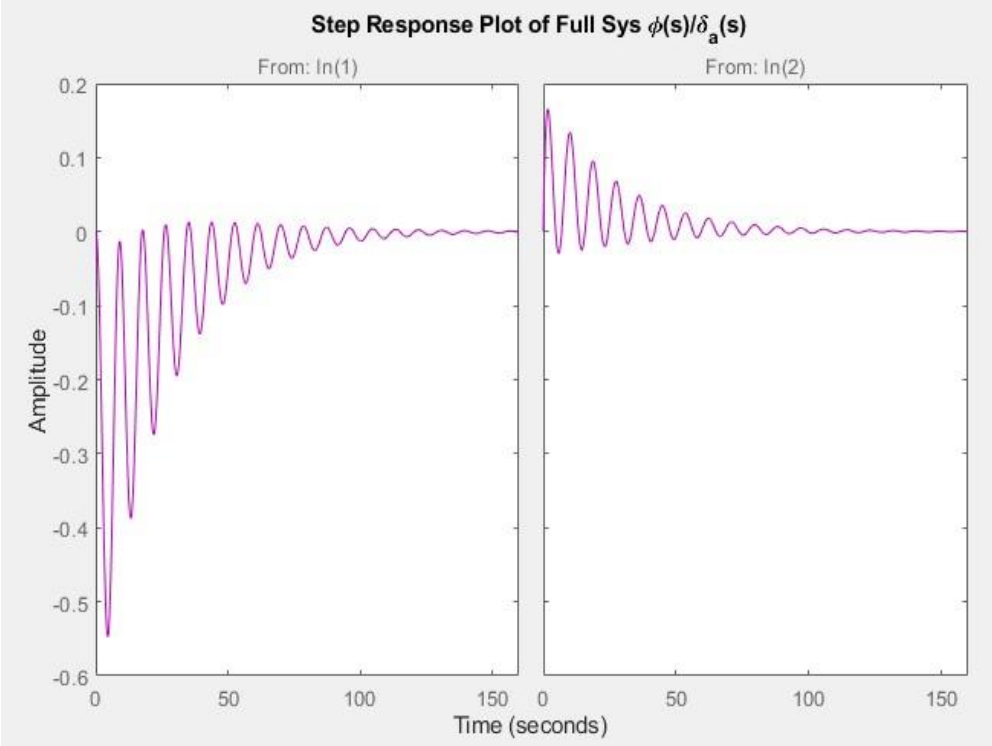

Figure 9: Boeing 747 lateral-directional step response of ϕ(s)/(δα (s))

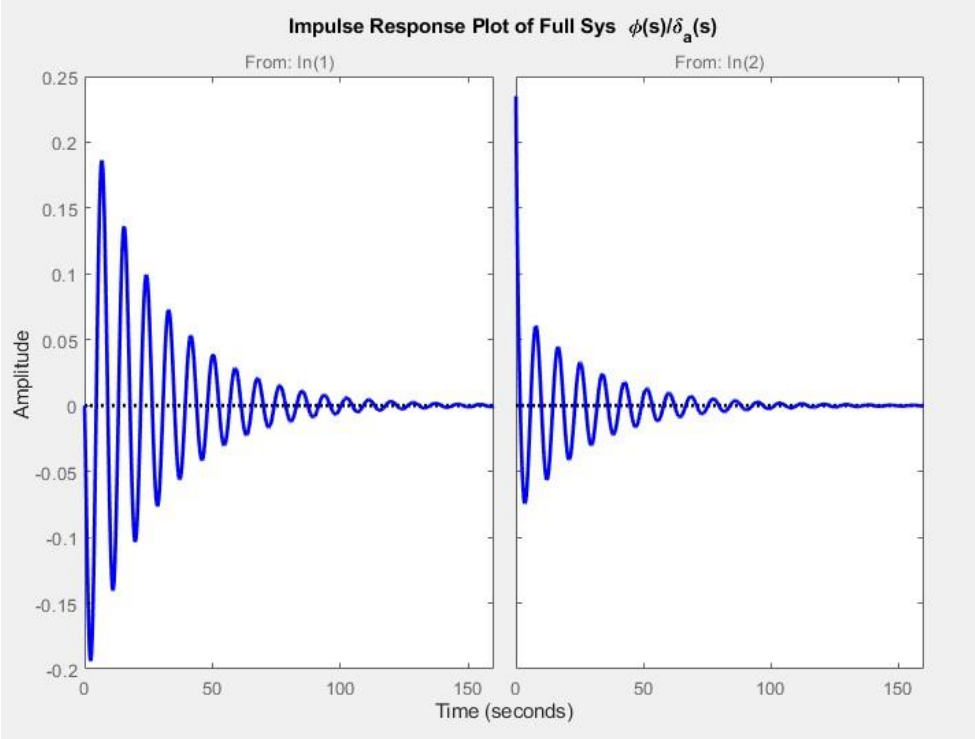

Figure 10: Boeing 747 lateral-directional impulse response of ϕ(s)/(δα (s))

Analyzing these graphs, we can see that the change in the aileron provides a steady flight with the change in the roll angle over time as it stabilizes at around fifty to sixty seconds once perturbed, however once we see the heading angle change, we can see that it has a harder time to stabilize under a stepped response, compared to an impulse.

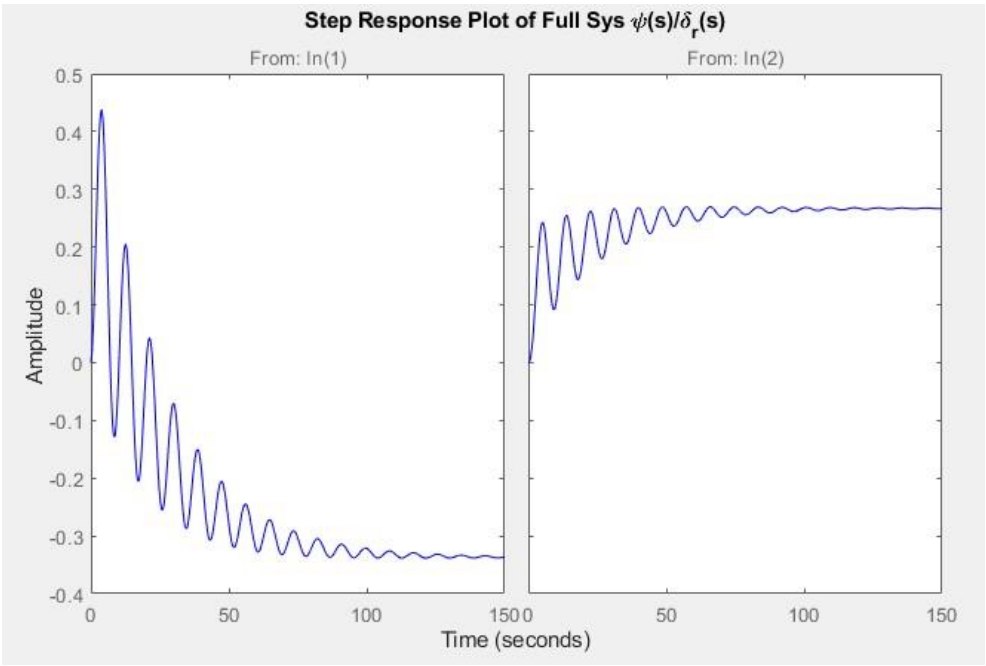

Figure 11: Boeing 747 lateral-directional step response of ψ(s)/(δr (s))

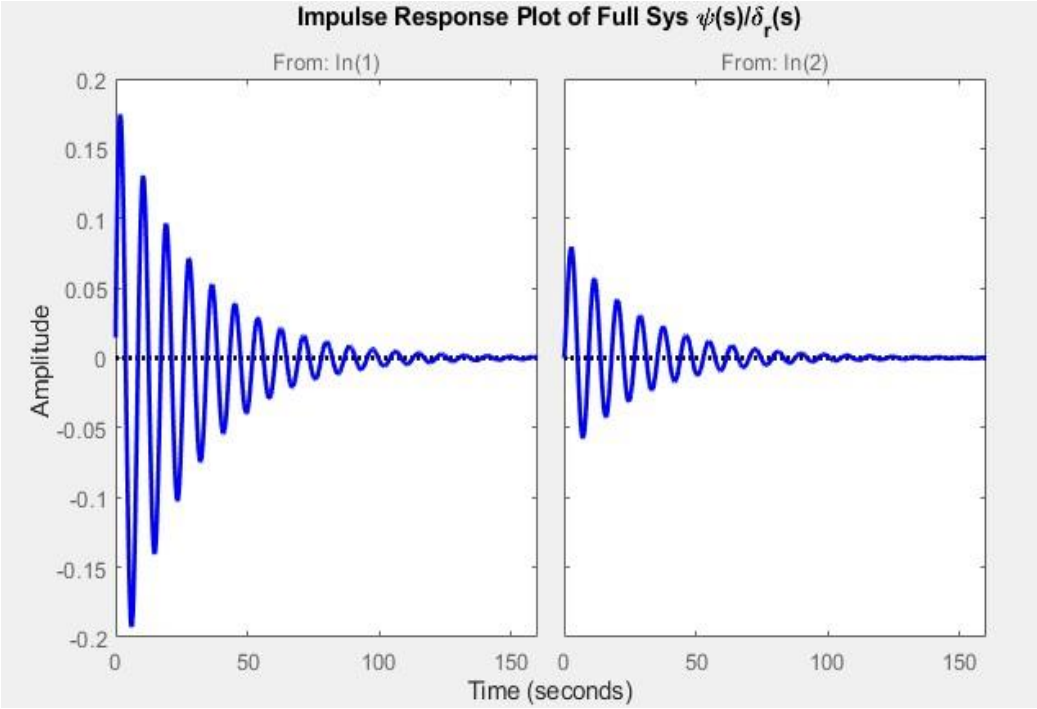

Figure 12:Boeing 747 lateral-directional impulse response of ψ(s)/(δ_r (s))

With these response results, we can now develop a controller design to optimize the aileron and rolling angle responses with a closed loop analysis.

2.5 Optimized Prototype Controller Design

Prototyping a control system after knowing what responses provide stability allows for a better understanding of what values need to be tuned and controlled. This optimization will incur with four separate optimizations:

- Aileron to Roll Angle Control
- Rudder to Yaw Angle Control
- Elevator to Pitch rate control
- Elevator to Angle of Attack Control

2.5.1 Aileron to Roll Angle PID Control

Since we know that the controllability matrix in each direction is five, this states that all five lateral/directional modes can be controlled by parameters in the input matrix B. for these axes we will use a proportional integral derivative (PID) controller. This starts by designing a PID controller to find what frequency is the most neutrally stable for the aircraft system created in Simulink. This will include a step input which will simulate the desired roll angle, then a PID constant block next to a unit transfer function. Then a saturation block will simulate the

maximum air speed of the aircraft, and a rate limiter is used to replicate the deflection of the aileron.

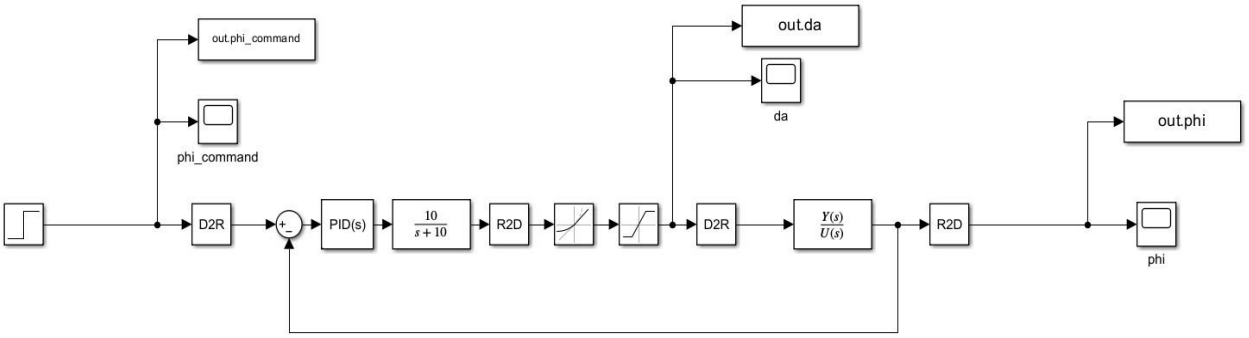

Figure 13: PID Simulink controller for ϕ(s)/(δα (s))

From here we will need to tune the integral and derivative gains in the Simulink file, K_i and K_d until the system is neutralized. With neutrally stabilized conditions we can plot the response to see where the maximum attainable value is before the aircraft becomes unstable.

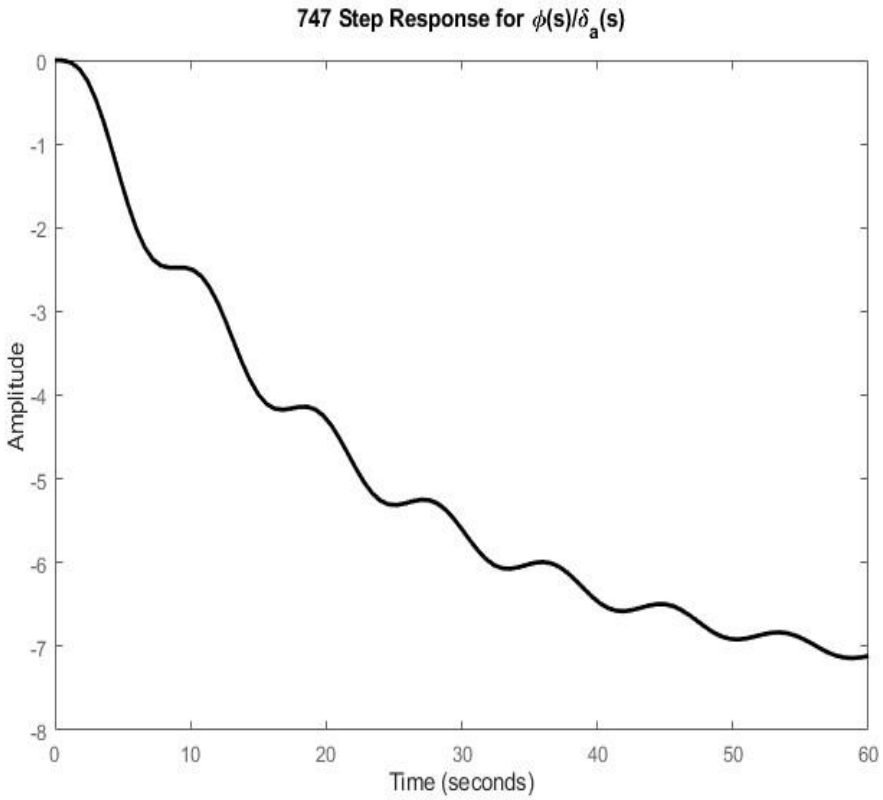

Figure 14: step response of roll angle to aileron deflection

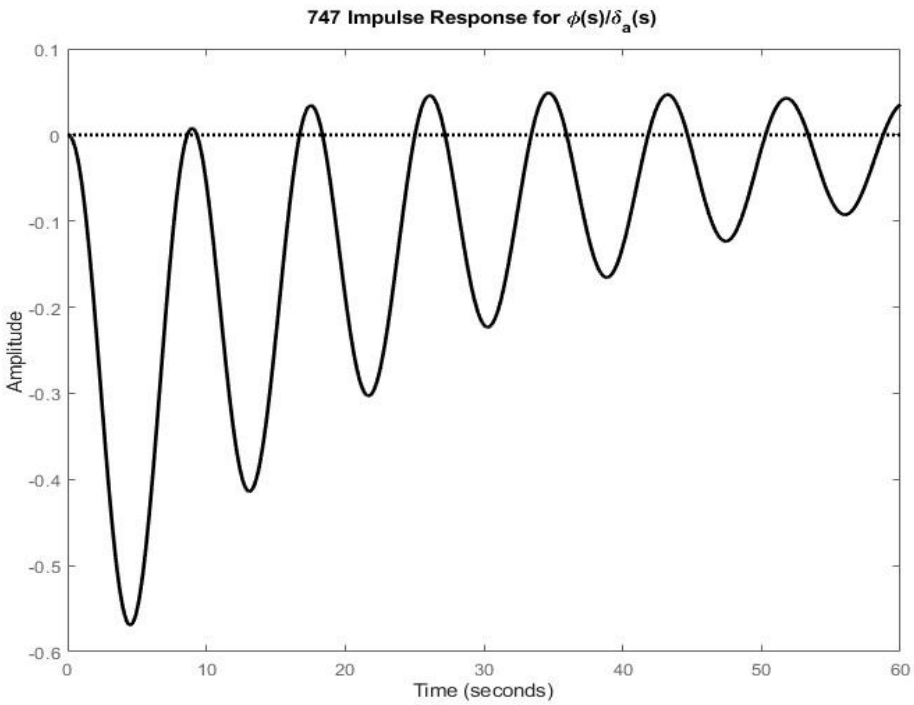

Figure 15: impulse response of roll angle to aileron deflection

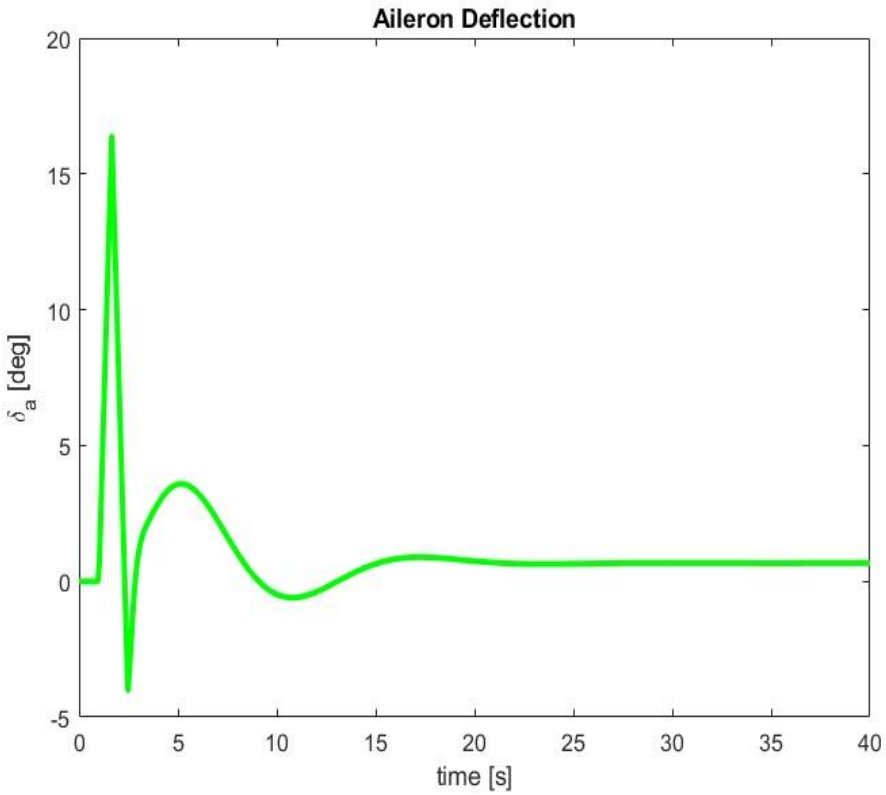

Figure 16: change in aileron deflection over time using PID

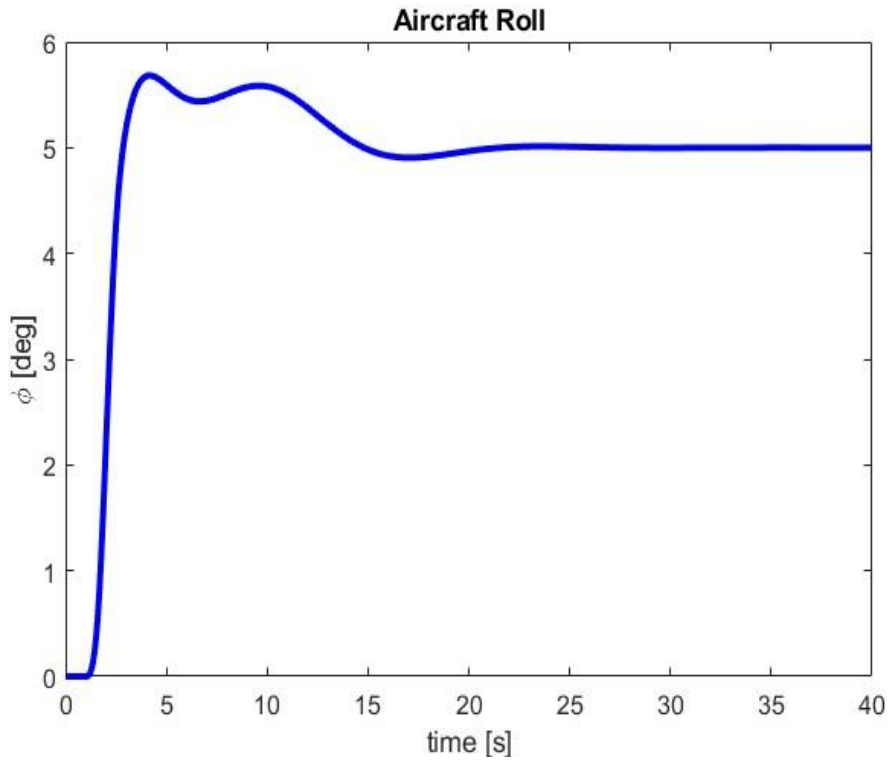

Figure 17: change in aircraft roll angle over time using PID

For this study we see that the PID controller used minimizes the number of oscillations it takes to stabilize the system, along with the overshot needed to correct itself. The aileron deflection plot shows a larger overshoot for the first five seconds, then undershoots after five, then stabilizes by fifteen seconds after the perturbation. This change in angle is viewed less in the aircraft roll where it overshoots after five seconds, then stabilizes after fifteen seconds as well. Analyzing the PID controller for this system shows that the gain can be improved to provide a faster response and minimal overshoot for controlling the aileron deflection and roll angle.

2.5.2 Rudder to Yaw Angle Control with LQR

This section discusses the optimization of the lateral directional controls using a linear quadratic reduction, or LQR for short to evaluate the controllability in each directional change that impacts the performance. To use LQR, we would need to tune both the quadratic and reduction matrices with the same state matrices used in the lateral directional control stability. The quadratic matrix will use a 5x5 matrix used as a product with the same dimensions as the input matrix used above, as well as the R matrix being a 2x2 identity matrix to provide the output. From here we would need to solve for the reduced Ricatti equation to generate the P matrix, as well as the optimal gains needed for the block diagram.

$$A^TP+PA-PBR^{-1}B^TP=0 \text{ (2.39)}$$

$$K=R^{-1}B^TP \text{ (2.40)}$$

Then we can input this into MATLAB to compute the optimal controller gain, which can be written as a command such as “lqr(A_lat, B_lat, Q_lat, R_lat)” to calculate the gain. From here we can create a flow chart representing each of the variables in line with the controller gain, using the lateral-directional control state and input matrices. This controller is designed to output the yaw angle of the aircraft and compares three different responses: the LQR design, the simple feedback, and the open loop design.

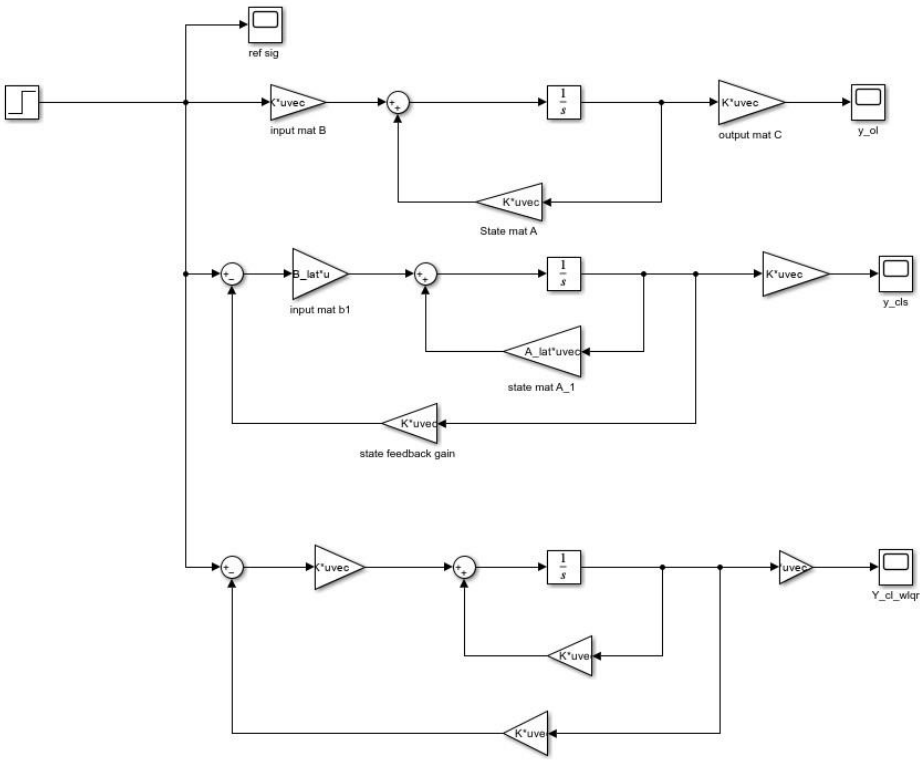

Figure 18: block diagram of an LQR controller for the Boeing 747

We are now able to obtain the responses for each lateral-directional quantity, which is then used for our feedback control program to plot the values over a ten second interval from a step input over a five-minute range. The intention is to measure the components listed in a free body diagram based on the aircraft’s sea-level flight conditions.

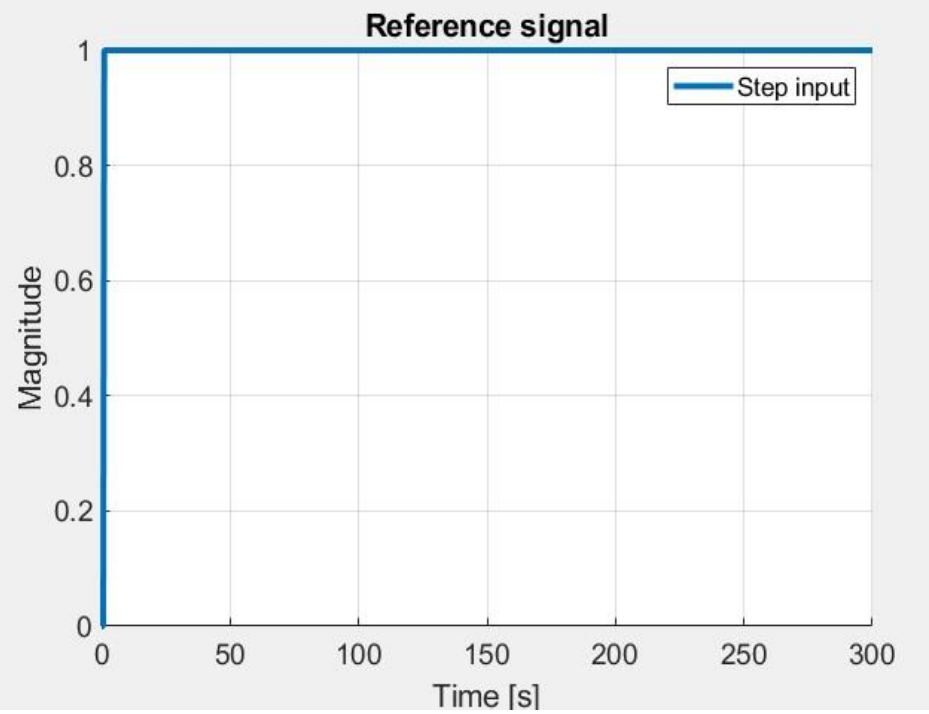

Figure 19: reference signal of LQR response

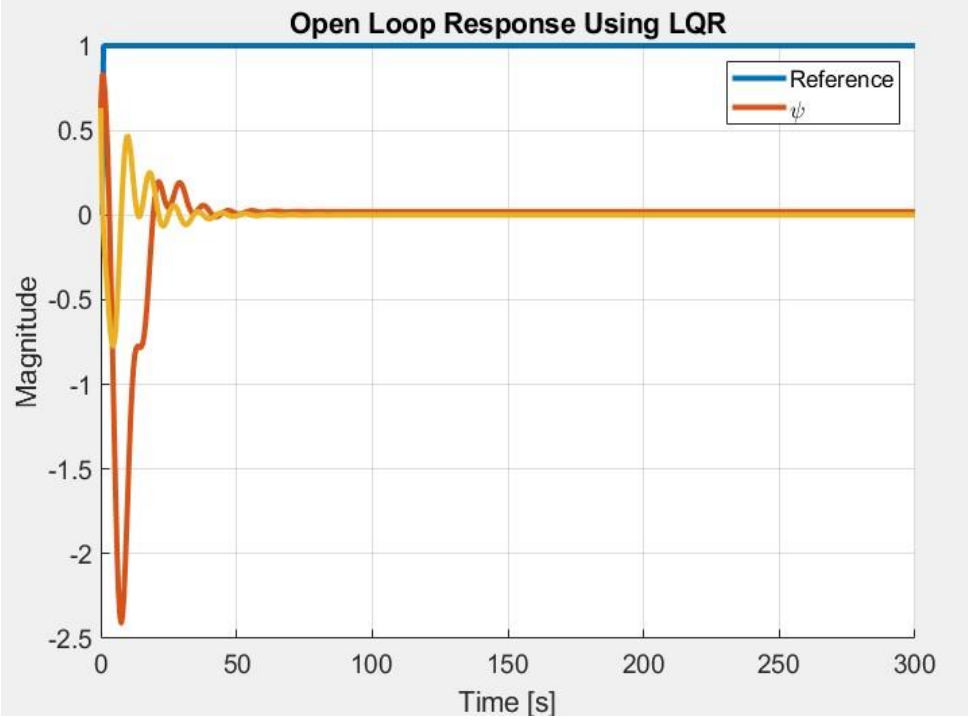

Figure 20: open loop response of δr to ψ angle with LQR

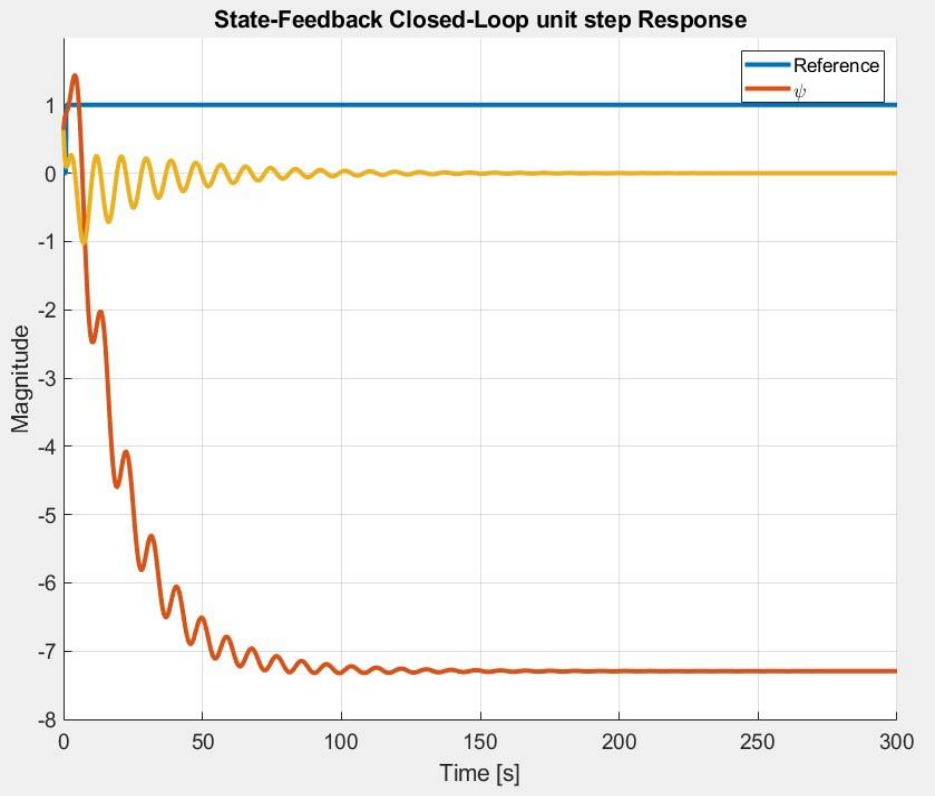

Figure 21: state feedback closed loop response of δr to ψ with LQR

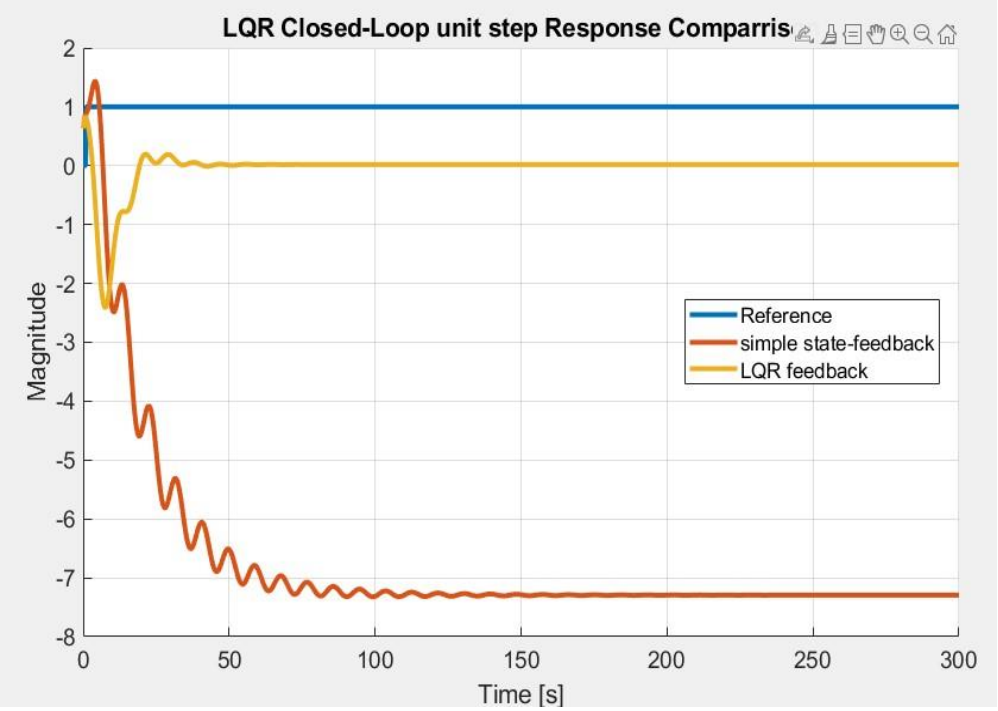

Figure 22: comparison of closed-loop LQR and state feedback

After plotting the computed values obtained from the LQR controller, we can see that the open loop response accurately to the provided step input. Under the feedback closed loop response we can see that the aircraft first overcorrects itself, next under corrects, then stabilizes at approximately 150 seconds. These values were obtained by modifying the C matrix as a four-by-one matrix written as [0,0,0,1]. At a five-minute period, we can see how an LQR controller is optimized for an extended period stability. This is best seen in the last image comparing the LQR feedback to the closed loop response where the state feedback fails to residualizing in comparison to the LQR model.

2.5.3 Elevator to Pitch Rate control with PID

After analyzing the rudder to yaw angle controller, we will use PID again to analyze and optimize the controller relative to the elevator and pitch rate. For this control system we aim to prevent sudden longitudinal acceleration from large perturbations, thus a successive loop closure is chosen. However, a successive loop has an issue of being sluggish in response to the command input. To combat this issue, we looked at three PID tuning methods to determine which is best: Cohen-Coon, Kappa-Tau, and Hagglund Astrom.

Table 5: PID constant for different methods

	P	I	D
Cohen-Coon	$\left(\frac{1.35}{K_u}\right)\left(1+\frac{0.18\tau}{1-\tau}\right)$	$(2.5-2.0\tau)P_u(1-0.39\tau)$	$(0.37-0.37\tau)P_u(1-0.81\tau)$
Kappa-Tau	$\frac{3.8}{K_u}e^{-8.4\tau+7.3r^2}$	$5.2P_u e^{-2.5\tau-1.4\tau^2}$	$0.89P_u e^{-0.37\tau-4.1\tau^2}$
Hagglund-Astrom	$\frac{0.66}{Gm}cosd\left(\frac{79.2}{\pi}-PM\right)$	$\frac{2}{Wpm}\left(tand\left(\frac{79.2}{\pi}-PM\right)-\sqrt{1+tand^2\left(\frac{79.2}{\pi}-PM\right)}\right)$	$\frac{I}{4}$

The Cohen-coon method is an optimized method od the Ziegler-Nichols method, meaning that this also requires a time constant, system gain and time delay as the previous method. This also means there is a large overshoot in the results. The Kappa-tau method performs similarly to the Ziegler-Nichols method in reducing overshoot and results in around a 30% overshoot reduction. Lastly the Hagglund-Astrom method operates on a relay method focusing on rejection of disturbances. This means the controller is initially assumed to be for a bang-bang system, providing on or off states. Based on calculations we determined that the Hagglund-Astrom method is best suited for this control system and is used for the controller optimization. So, from this, the gain margin (GM), phase margin (PM), and crossover frequency (Wpm) are used. If the plant can only

produce on or off values, we know that PID is inherently oscillatory. This results in square wave oscillations which provide an advantage, where the designer can choose the oscillation frequency of the response. This is great for control surfaces since flutter must be suppressed and results in the default oscillation being approximately the length of pi. From here the gain is increased to decrease the oscillation speed where the overshoot remains lower than the rest.

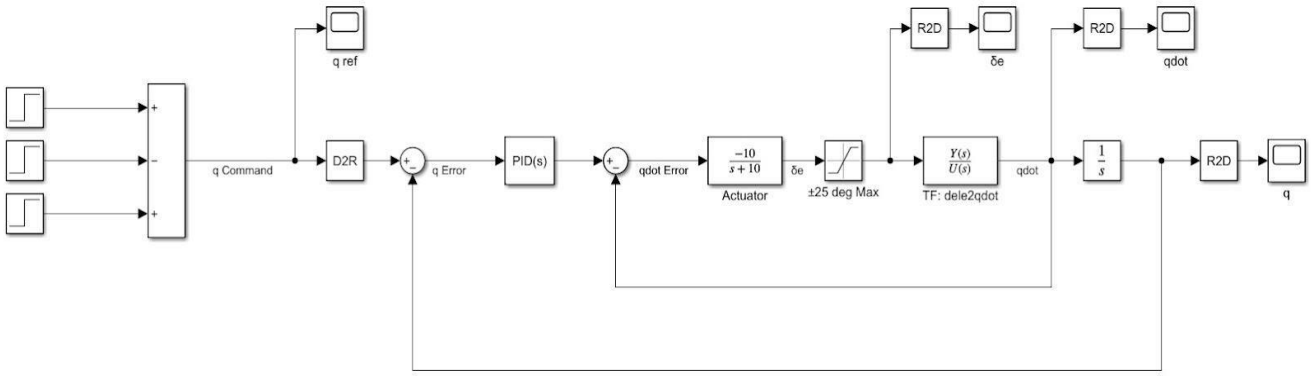

Figure 23: Simulink block diagram for PID controller for elevator to pitch rate

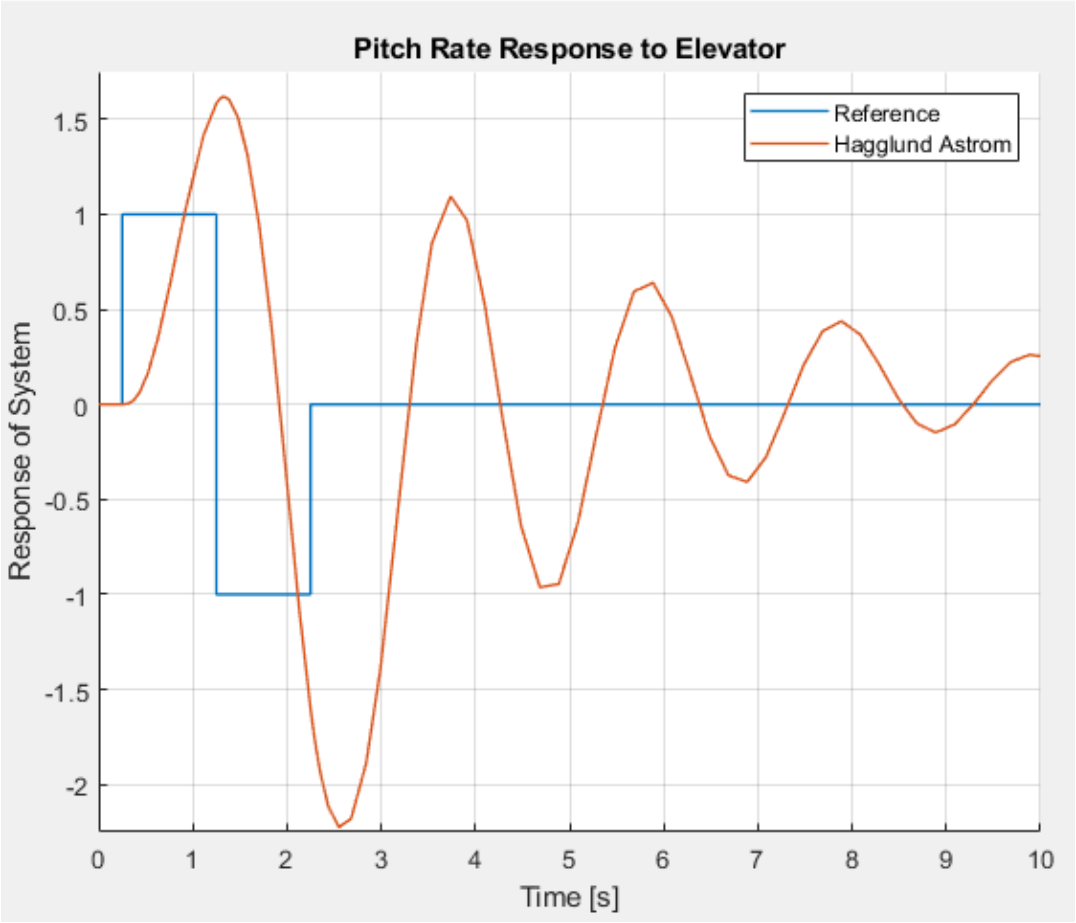

Figure 24: longitudinal system Response with the Hagglund-Astrom PID controller

2.5.4 Elevator to Angle of Attack Dynamic Inversion Controller

This section of the report will consist of improving the overall stability of the system. After viewing the longitudinal open loop response, we know there's a long settling time for the system, which will benefit from the use of a dynamic inversion controller, implemented at sea level conditions. This starts by controlling the elevator deflection input which impact the angle of attack, then hold said angle to stabilize during flight, and decrease the settling time and oscillations of the system. This provides a better closed loop transient response, an advantage to robustness, as well as less control magnitude for the behavior of the aircraft and becomes powerful for the control of non-linear systems. This analysis can be shown with a control law with the use of a linear time-invariant (LTI) system shown below:

$$u = (CB)^{-1}(\dot{r} - CAx + Ke) \tag{2.45}$$

From the LTI system, we have A, B, and C matrices form our state space equations above, r is the input reference signal, K is the controller gain, x represents the state vector, and e is the error signal between the desired output and the current output. For the desired output we situate the C matrix in a four by one matrix as [0 1 0 0] to output the necessary angle of attack response. The controller gain, K is the main parameter what will be tuned to optimize the dynamic inversion controller, which can be tuned and customized in the block diagram below.

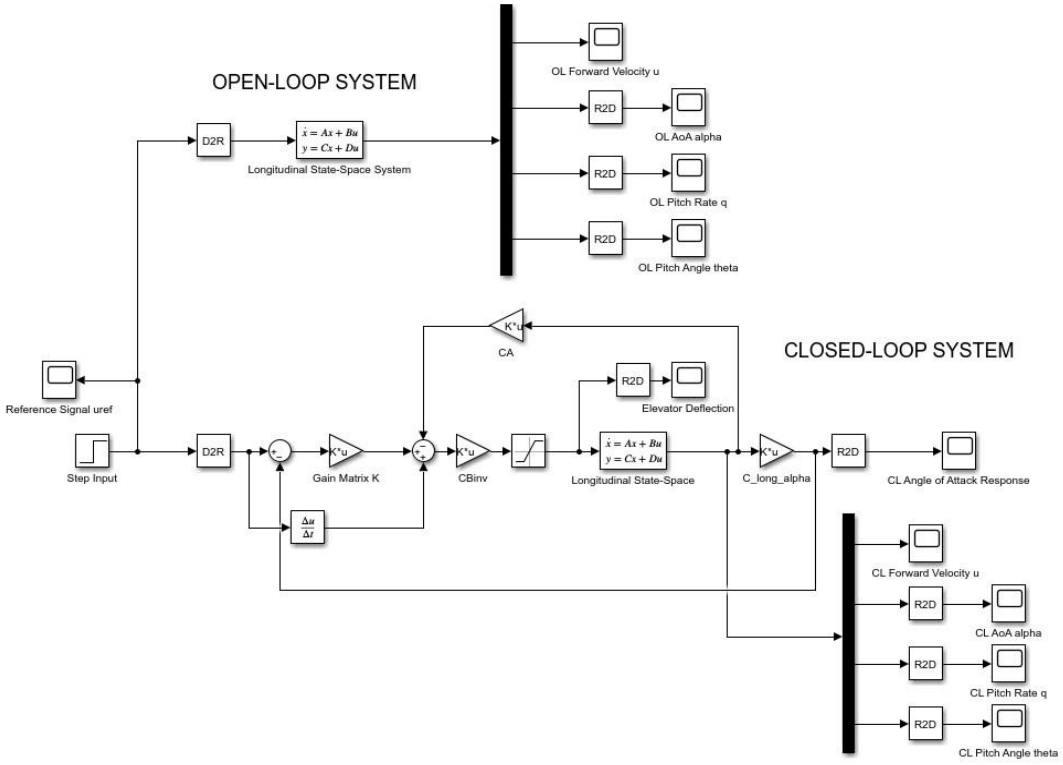

Figure 25: Simulink block diagram of dynamic inversion controller for elevator to aoa

This controller will be used to track the reference signal, being a unit step function timed at one second. This is shown in the figure below and will use the dynamic inversion controller to track the reference signal at sea level conditions. From here we vary the controller gain from one to sixteen, to find the optimal controller performance of settling time and maximum overshoot. This test is shown on the table below:

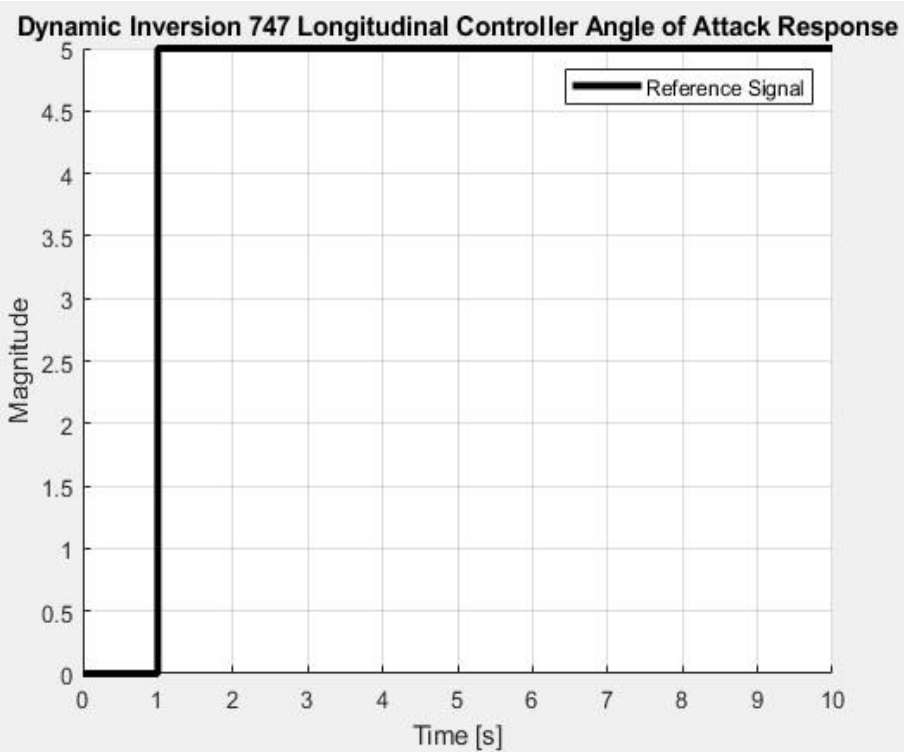

Figure 26: five-degree angle of attack reference signal

Table 6: maximum Overshoot and Settling time for varying controller gain values (K)

K	1	2	3	4	5	6	7	8
t_s	5.76	3.736	3.379	2.988	2.81	2.76	2.527	2.354
M	4.94	4.955	4.981	4.980	4.986	4.991	4.99	5.06
K	9	10	11	12	13	14	15	16
t_s	2.370	2.784	2.73	2.747	2.76	2.809	2.829	2.85
M	5.01	5.006	5.011	5.012	5.010	5.006	5.004	5.002

Based on our tabulated performance characteristics it seems that a value between eight and nine yields the best performance comparing settling time and maximum overshot. Anything below eight undershot the magnitude, whereas any value above ten began to overshoot. This is then plotted with an open loop and closed loop response for the longitudinal state space system. The close loop angle of attack is plotted in line with the reference signal to provide a tracking demonstration.

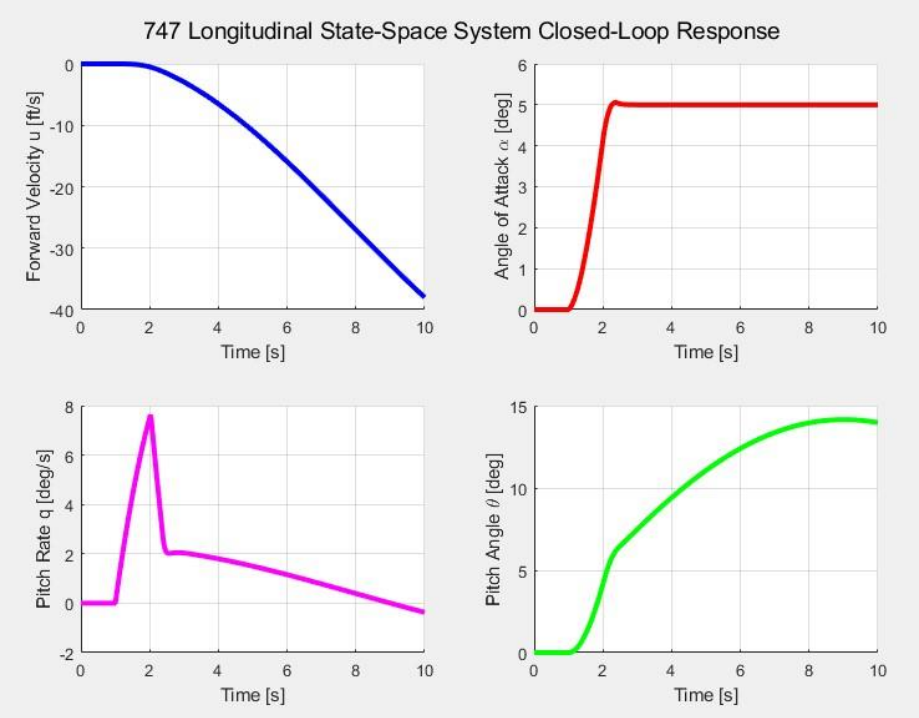

Figure 27:747 longitudinal state space system closed loop response.

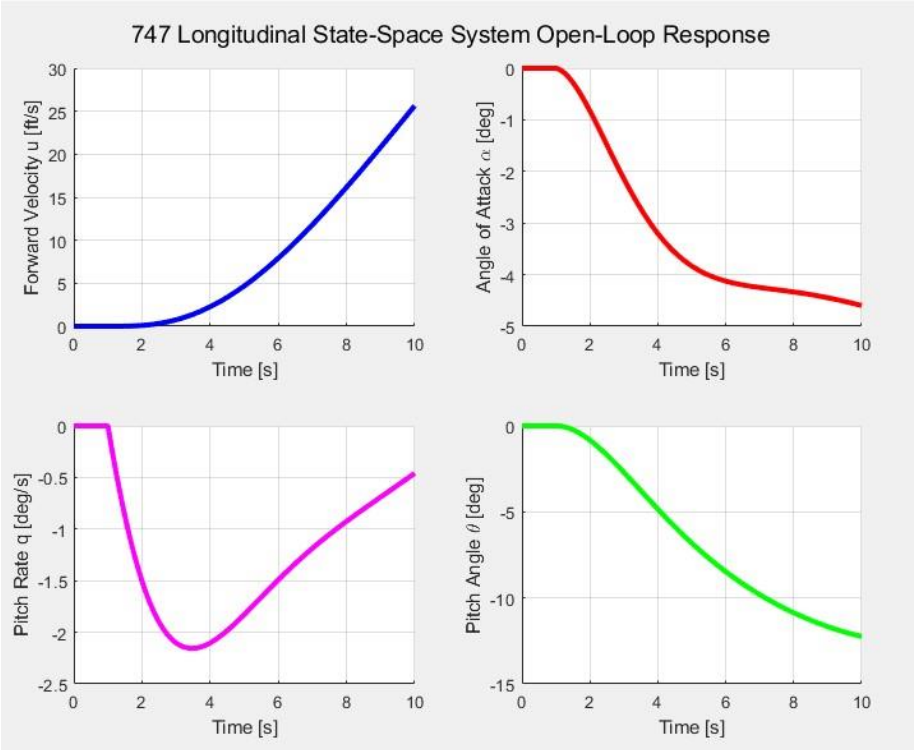

Figure 28: 747 longitudinal state space system open loop response

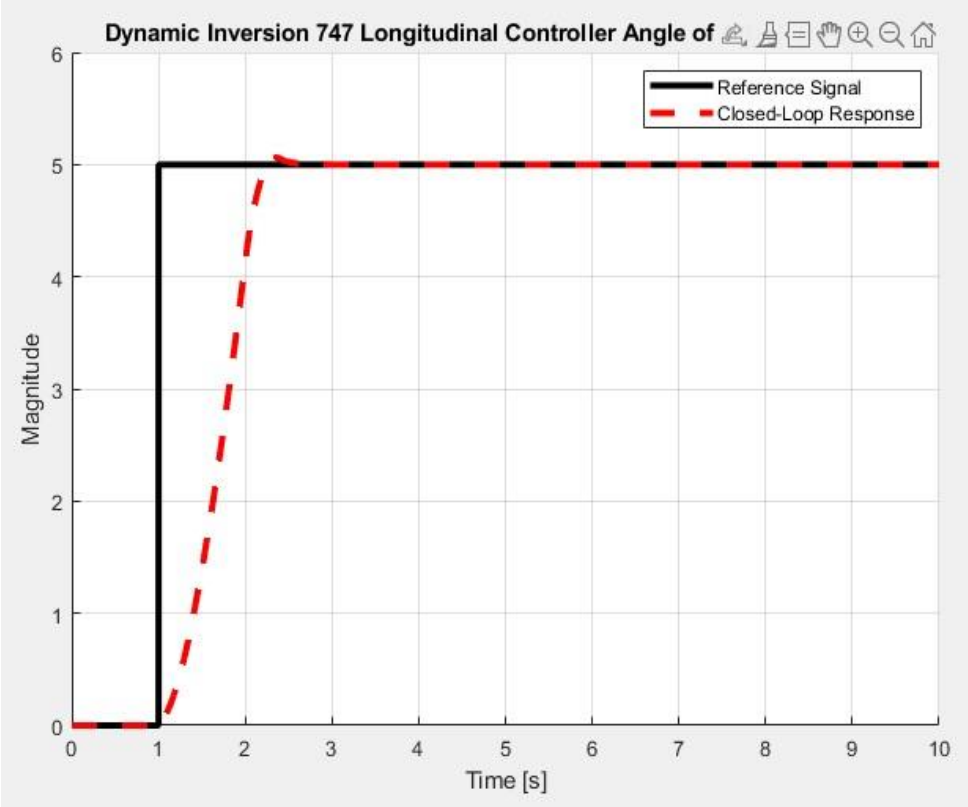

Figure 29:747 dynamic inversion longitudinal controller AOA Response

With the controllability gain of around eight the settling time is around 2.3 seconds and has little to no overshoot. This effectively controls the angle of attack of the Boeing 747 at sea level. Comparing the other rates such as forward velocity, and pitch rate shows an oscillatory increase over time, whereas the angle of attack and pitch angle shows a decrease but are still showing stability in their plotted results. The elevator deflection angle is shown below and has a deflection limit between 25 and-25 degrees.

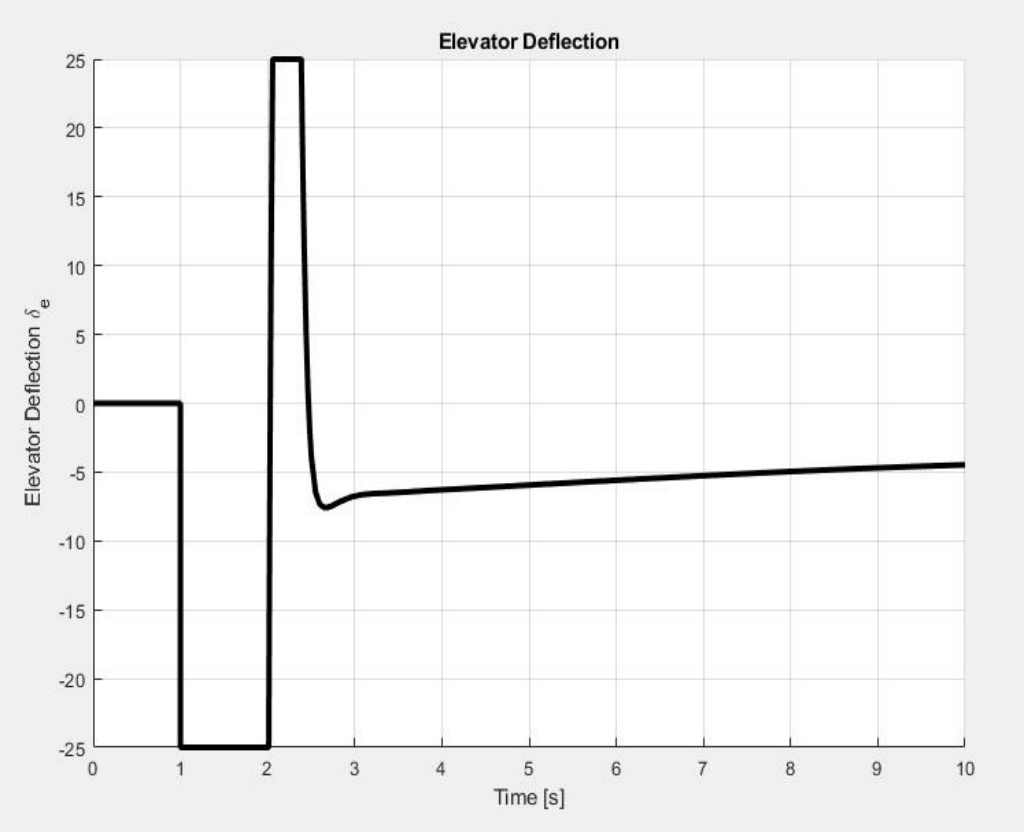

Figure 30: 747 dynamic inversion elevator deflection

2.6 Prototyping Results

The results of the controller designs yield the expected values and performance metrics for the Boeing 747 aircraft. Longitudinal stability results showed a lengthy stabilization time, as well as the time it takes for the aircraft to return to the commanded pitch angle, where this can be solved by reducing the provided gain to optimize its stability. The lateral directional stabilities provided for the aircraft show a long, albeit shorter response time of about a minute to the given impulse. After the stability analysis, we compared the relation between the aileron to roll angle, where there is a short period where the PID controller overshoots the target angle, then stabilizes in a quick manner. The Rudder to the Yaw angle control system using a linear quadratic reduction provides the fastest settling time at the provided angle of attack. Analyzing the graphs have shown that the best solution to optimizing the control systems to account for magnetic controls is to reduce the gain on longitudinal as well as lateral-directional stability, then the aileron controls can be adjusted by changing the integrator values to minimize the stabilization time. Lastly the elevator relation to the angle of attack can be improved by optimizing the gain matrix and integrating additional parameters. This integrates magnetic control devices for the aircraft system and will be discussed in the next chapter.

Chapter 3: Integration of magnetic control devices and parameters in aircraft control systems

3.1 Introduction of part integration

After designing the prototype control system using PID, LQR and Dynamic Inversion controllers, we can now implement the necessary parameters of magnetic controllers to improve the performance of the provided controller designs in the aircraft. Since the proposal, we have tested and developed a functioning model for our system, then provided results for where the prototype controller can be improved with magnetic controls. We know from the previous tests that the aileron to roll angle, as well as elevator to pitch angle, controls can be improved by changing the PID constants using alternative equations for the proportional, integral and derivative to better suit out controller requirements. For the rudder to yaw angle control we determined that its best to leave most of the LQR values the same, but change the gain, K to further reduce the settling time for a more stable flight. The elevator to angle of attack, using dynamic inversion we need to find an overshoot value and settling time value between the selected in table 5 to determine a more subtle approach. With the integration of magnetic controls, we can then assess, and test new values used to optimize this control system.

This chapter will be separated into three segments. First, we will select and determine what controller or magnetic device we can use to integrate into our control system, as well as determine what are the necessary parameters and values, to properly integrate the controller. Next, using the parameters discovered in the magnetic controller, we will first optimize the PID controllers by analyzing three different PID constant methods and determining which will best suit the magnetic controller design. These optimized constants will be used for both the elevator to pitch angle controls, as well as the aileron to roll angle control systems. Then, the LQR and dynamic inversion control system will then have magnetic controls implemented with improved gain parameters as well as the settling and overshoot times. Finally, we can analyze and discuss the results provided and see provide acumen on how else this can be implemented.

3.2 Magnetic Controller devices

To begin with the optimization of the control system we have started, we will need to find the right controller that meets the requirements. As stated previously, these controllers need to provide a gain value to improve the LQR and dynamic inversion parameters of settling time and overshoot. Then it must be able to operate as a PID controller and we must choose which constant method is best for operation. This section will look at a selection of magnetic controllers that fit the criterion of the control system and will be chosen for testing. Magnetic controllers are made of two separate components, which are the actuators and the controller. Along with additional subcomponents, these two parts account for the user input into machine language for precise measurements and actions, which we will look at three specific categories:

- Magnetic Bearing Controllers

- Permanent magnetic actuators with a mechanical controller
- Variable reluctance actuators with mechanical controller

3.2.1 Magnetic bearing controller analysis

We can start by analyzing the magnetic bearing controller and how it works. These operate in a system which includes several independent components that work simultaneously in a feedback loop. For a proper example, we will use the Calentix insights magnetic bearing controller which provides multiple power and voltage ratings to accommodate for various machines.

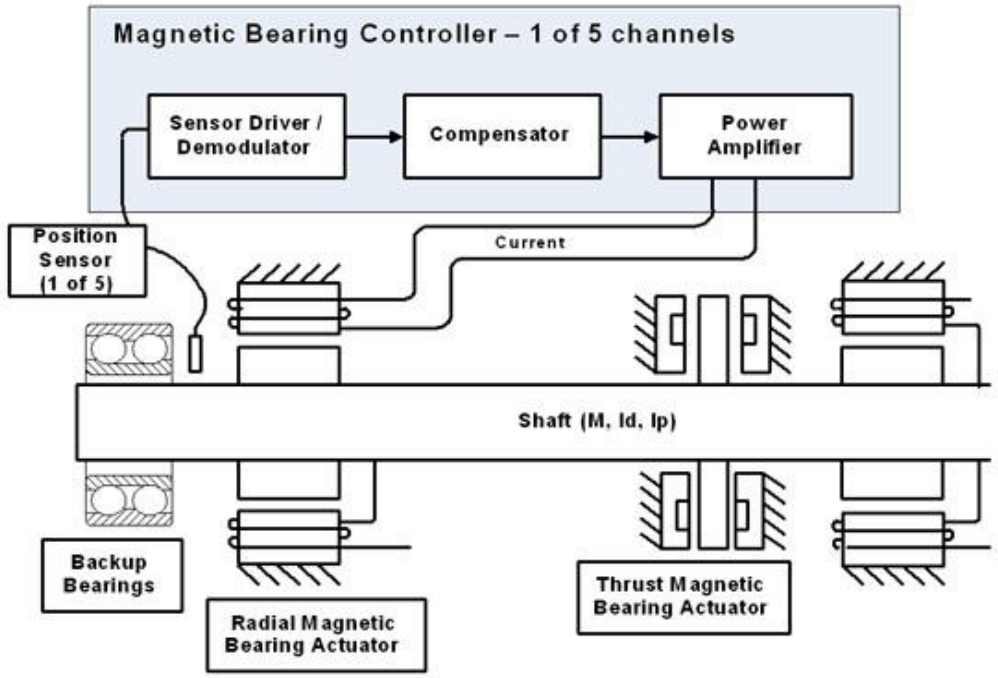

Figure 31: magnetic bearing controller relationship with sensors and actuators

In the figure above we can see that a basic rotor and magnetic bearing system have an active magnetic bearing (AMB) which includes electromagnetic actuators and position sensors. These are then connected to the magnetic bearing controller (MBC) through cables, thus forming a complete AMB system. Key elements are contained int eh MBC such as the digital signal processor board (DSP), with the purpose of processing signals from the position sensors and then executes a control algorithm to stabilize the rotor. This image also shows that the DSP manages levitation logic, diagnostic functions and fault detection. There is also a power amplifier which translates DSP commands into electrical currents and then drives the coils. From this analysis we can see that the control system ensures precise motor positioning through electromagnetic force adjustments.

Next, we will look at the feedback loop that is generated from the magnetic bearing controller, which is seen below:

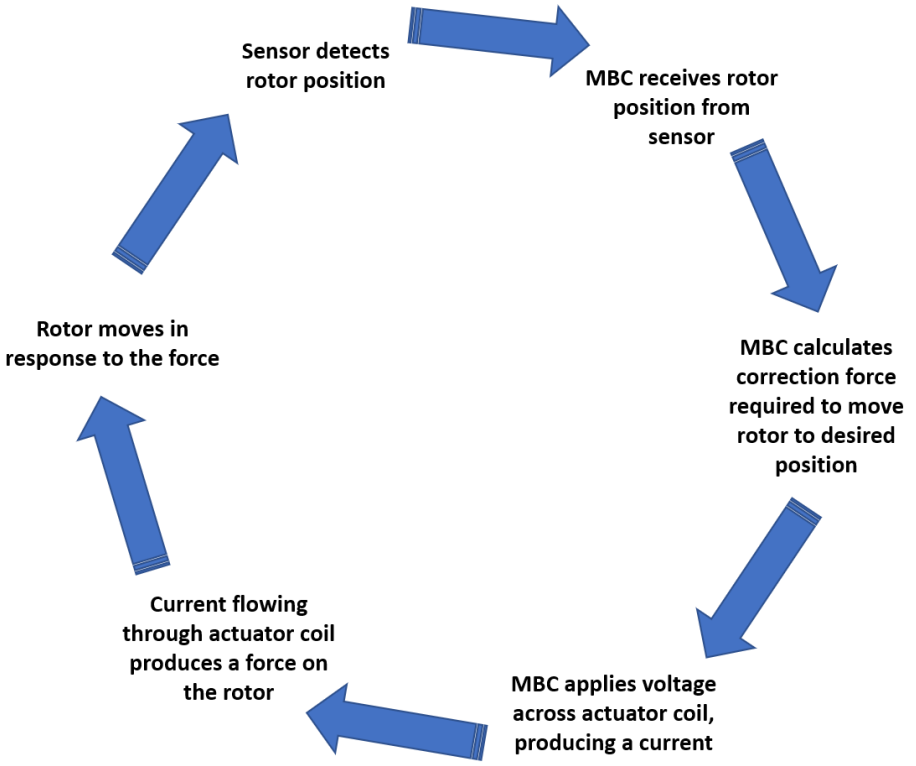

Figure 32: basic operation and feedback of the magnetic bearing control loop

The operations of this control system loop begin with the position sensors detecting rotor movement and then sends a voltage signal to the DSP in the MBC. From here the DSP determines the error between the actual rotor positions and the desired rotor positions, then calculates the corrective actions using a compensatory algorithm. The diagram also shows that the power amplifier convers the input command to current, which flows through the actuator coils to generate electromagnetic forces and stabilizes the rotors. From here, AMD systems generate both stiffness and damping forces to maintain rotor stability, compared to conventional bearings that rely on mechanical fluid forces. This frequent change of forces is often overlooked by the compensators transfer function, designed using a machines rotor dynamic model, which is then stored in the DSP's flash memory. Lastly, additional machine specific data, such as fault logs and sensor calibration is saved in DSP memory for reliable and precise operation.

For the simplicity of computations and calculations, the magnetic bearing controller we will use for this project is the Calnetix technologies insight 804 controller shown below.

Figure 33: Calnetix Insight 804 Controller

This controller provides all the operational needs as stated above as well as exceeds requirements for controller integration with the size and cooling requirements needed for the aircraft. The specifications are listed in a table below:

Table 7: voltage, current and dimension parameters of the Insight 804

Insight 804 Parameters	
Input Voltage [VDC]	144
Maximum Continuous current output [A]	3
Amplifier current rating [A]	6
Bus voltage [VDC]	144
Cooling method	Cold Plate
Dimensions [in]	10 × 8 × 3

For this controller to be used in our aircraft control system, we will need a motor to operate the given commands. For this controller we used a DC servo motor by McMaster-Carr part number 5082N33. This motor is used for small automation applications however, for the necessary calculations, we will only need two parameters of the motor, the shaft diameter (19 mm), and rotations per minute (3000 rpm). These parameters will be used to calculate the force this controller provides.

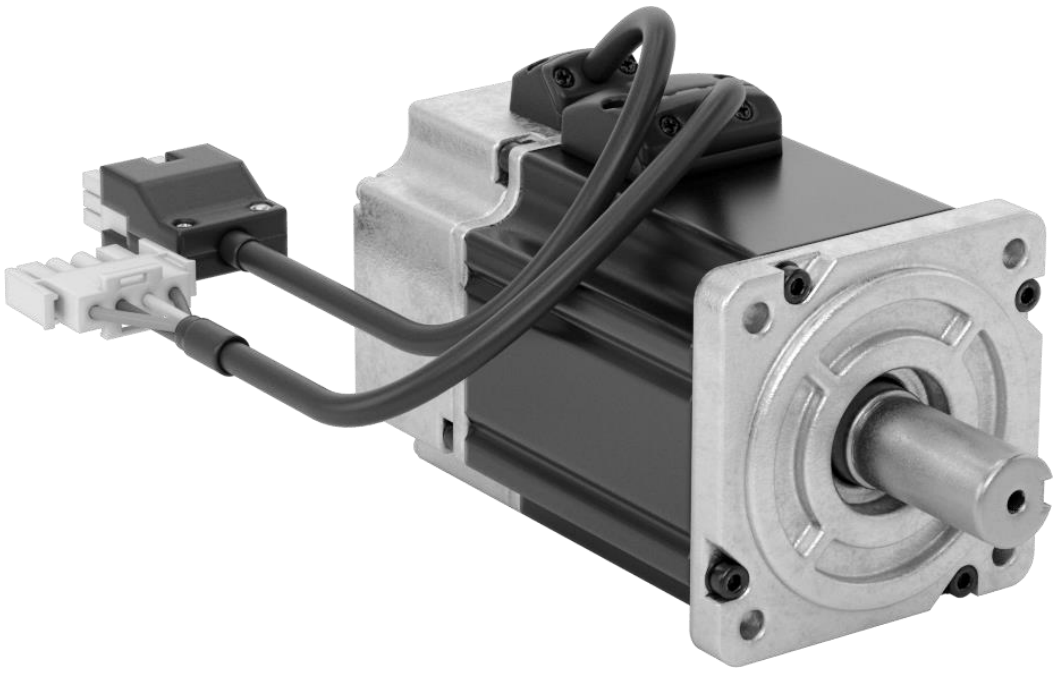

Figure 34: McMaster-Carr DC Servo motor PN 5082N33

3.2.2 Permanent Magnetic Actuator analysis

This subsection will look at the linear magnetic actuator and determine what best suits the problem description. Linear magnetic actuators are advanced motion control devices that operate on electromagnetism, with greater precision, reliability and efficiency compared to the traditional mechanical system. Magnetic actuators consist of a stationary stator, and a moving translator where the electromagnetic interactions produce a linear force which enables smooth controlled movement. This is often categorized into two main types: permanent magnet actuators and variable reluctance actuators.

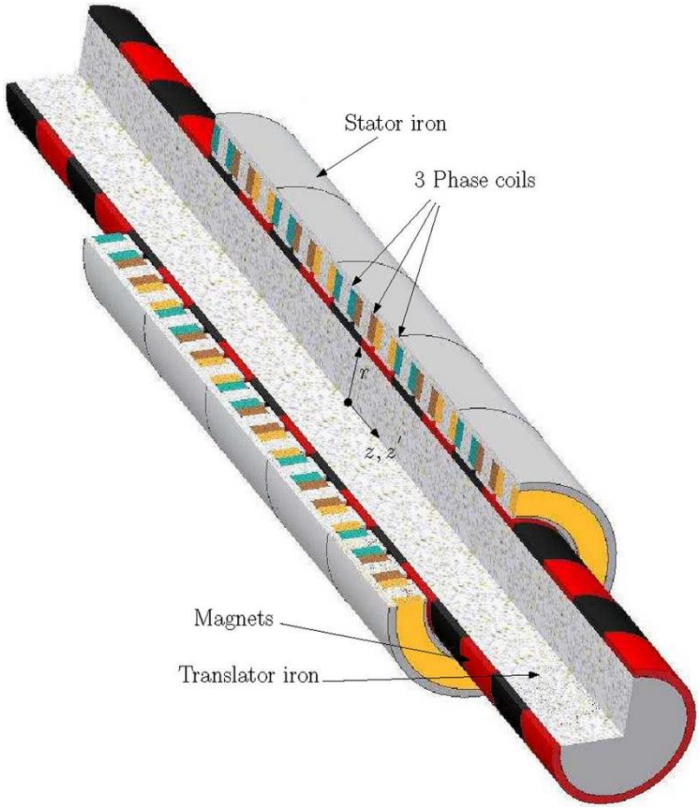

Figure 35: tubular permanent magnetic actuator

Permanent magnet actuators offer a unique solution to control, since they are fixed magnets that provide a higher force density, as well as generate a steady magnetic field. This means that for the actuator to create motion, the electromagnetic coils need to modulate for the action to happen. The working principle of the actuator is driven by the interaction of the permanent magnet's field with the electromagnetic field generated by the coil. This provides a more constant and smooth torque output due to the continuous presence of the magnetic field. This offers more power efficiency due to the permanent magnet that contributes to the force generation without additional current. This means that this actuator is commonly used in servo motors, brushless DC motors and precise control systems. For analyzing the dynamics of this system, we will look at the ORCA series of linear magnetic actuators, from Iris Dynamics, and specifically use the ORCA-6-48V for the high force precise position accuracy.

Figure 36: model of the ORCA-6-48V linear magnetic actuator

This actuator meets the necessary specifications for operating motor controls for a given aircraft, most notably with position accuracies measuring in ranges of 150 micrometers and repeatable between 15 micrometers. However, looking at the specifications we can see that the minimum supply voltage is around 12V and maximum of 60V, each providing different performance metrics at the different voltages and temperatures, which will be listed below:

Table 8: force, speed and power characteristics of the ORCA-6-48V

Force, Power and Speed characteristics					
	Motor Temp (C)	12Vdd	24Vdd	48Vdd	60Vdd
Max Force(N)	20	143	287	573	683
Max Power (W)		102	408	1631	2023
Max Force Duration(s)		175	44	11	8
Fore Constant (Kf)		14.2 N/√W			
Max Force(N)	70	120	241	482	602
Max Power (W)		87	346	1386	2165
Max Force Duration(s)		<1			
Fore Constant (Kf)		12.9 N/√W			
Max Speed (m/s)	full range	0.7	1.4	2.8	3.6
Force Accuracy (N)	0.64				
Force Repeatability (N)	0.1				

From this chart we can see that as the actuator reaches its maximum voltage capacity, the higher the force, power and speed of the actuation. Though it does perform worse at 70 degrees, at about 83% of its normal operating temperatures, the duration time will also decrease based on how much voltage is given to the motor. Aircraft tend to operate sea level atmosphere, where the temperature is considerably lower, the high temperature measurements can be viewed as negligible. This shows the speed at which these motors accept user input, the force at which they are applied, as well as the precision at which the motors can move to, are more than capable of operating at high stress conditions in the air. One issue that can be observed with the motors is the cooling capabilities which are shown below:

Table 9: cooling characteristics of the ORCA-6-48V

Cooling			
	Condition	Power (W)	Force (N)
Continuous Power/Force	20 C ambient still air	34	75
	20 C ambient, single fan (10 CFM)	106	133
	20 C ambient, 2x 60 mm fans (39 CFM each)	139	153

Under still conditions, ambient air can keep the controller at a stable temperature, however it will still take about 34 watts of power to maintain a stable temperature for operation conditions. This value only increases as there are more fans implemented, however after considering the operating conditions of an aircraft, the external temperatures of said aircraft bypass the cooling requirements needed, with the only drawback viewable on permanent magnetic actuators being the power required to actuate said motors.

3.2.3 Variable Reluctance Actuator analysis

Next, we are looking at the variable reluctance motor or VRA for short, which differs from the permanent magnet actuator where it uses no permanent magnets and relies on an electromagnet that changes its magnetic reluctance to generate motion. The most common design seen is the stepper motor which can be seen below:

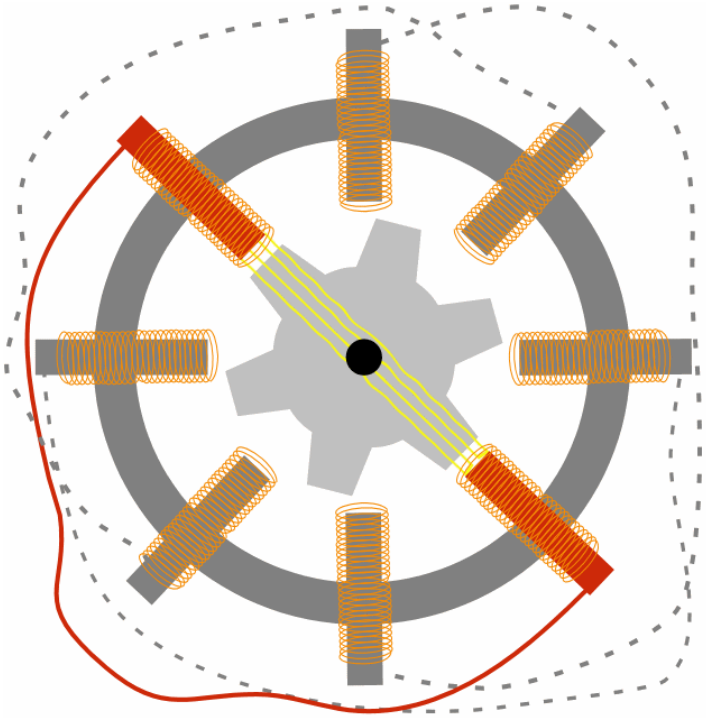

Figure 37: variable reluctance actuator

This actuator works because it changes the reluctance of the magnetic circuit by aligning a ferromagnetic rotor or armature with the magnetic field. This provides a torque and force which is typically more non-linear and can suffer from cogging effects due to the reluctance variations. Due to the movement of the magnet, however, this requires a continuous electrical input to generate the required force, much like the stepper motor we viewed in the beginning. Additionally, variable reluctance actuators are often used in solenoid actuators, stepper motors, as well as simple on/off actions which is best for low-cost manufacturing. To look at precise specifications, we will look at the Moving magnet actuator 5536 from Magnetic Innovations.

Figure 38: Moving magnetic actuator model 5536

This motor provides high precision and reliability. Due to the low power draw, this allows for more devices such as external position sensors and motion controllers to provide further precision for the provided input. The specifications for the motor are provided below:

Table 10: characteristics of the Moving Magnet Actuator 5536

5536 key Specifications	
Dimensions (mm)	55 x 36
Stroke Length (mm)	8
Peak Force (N)	140
Continuous Force (N)	35
Maximum Operating Voltage (VDC)	48
Moving Mass (kg)	0.2

From these characteristics we can see that the actuator can operate sufficiently in high vacuum environments as it ensures low outgassing and a contamination free environment.

3.2.4 Magnetic Actuator and Controller Discussion

There are many factors that determine the performance of these actuators such as coil design magnetic materials thermal management and bearing systems. Due to their numerous advantages, linear magnetic actuators are widely used across various industries. In automation, they provide precise positioning and high-speed motion control in manufacturing and material handling. In the medical field, they enable high-precision movement in surgical robots and diagnostic equipment. Additionally, transportation systems, such as magnetic levitation trains, utilize these actuators for efficient propulsion and guidance. The key benefits of linear magnetic actuators include reduced friction and wear, high accuracy, energy efficiency, and scalability, making them a preferred choice for applications requiring superior motion control solutions. As advancements continue, these

actuators are set to revolutionize various sectors by enhancing performance and reliability while minimizing maintenance needs.

Based on the results provided and the measurements we were given, we can determine that the magnetic bearing controller best suits the longitudinal stability of the aircraft. This is due to the increased stability that the controller provides as well as the stiffness of the control input needed for the overall flight operation of the aircraft. As stated before, the stability of the aircraft can be optimized with the change in the gain parameter of the Simulink controller. This will also aid in reducing the time it takes for the aircraft to stabilize through the help of electromagnetic force adjustments. Then finally we are using permanent magnet actuators to improve the lateral directional stabilities. Aside from the compact form factor, this provides high precision and long-term durability which is needed for lateral directional controls, but the smoothness of operation and precision allows for greater improvement of all controller actuations for the rudder, aileron and elevator controls needed for the aircraft.

3.3 Controller Optimization Results

With the specifications and data of the controller provided, we have all the necessary parameters needed from the magnetic controllers to improve our control systems. With the parameters set, we have determined that the magnetic bearing controller is best suited for the longitudinal controls of the Boeing 747 aircraft, and the permanent magnetic actuator is best suited for the lateral directional controls of the aircraft. Each of these controller parameters will be applied to gain parameters and matrices values, providing a change in the initial code which was optimized.

3.3.1 Longitudinal Stability with Magnetic bearing controller Integration

To start integrating the magnetic bearing controller for longitudinal stability, we need to find and correlate a relationship between the voltage, current and power to determine the force needed to improve the longitudinal performance of the aircraft. This is due to the parameters provided for the magnetic bearing controller showing only the voltage and current, meaning we will need to compute the applied force for the controller. We will start with the relationship between voltage, current and resistance:

$$V = I \cdot R \tag{3.1}$$

Where V is voltage measured in volts (vdc), I is current in ampere (A) and resistance measured in ohms (Ω). This can then be converted to electrical power using this equation:

$$P_{in} = I \cdot V \tag{3.2}$$

We know that motors do some work which can be defined as how much power the motor provides, which can be defined as the torque and turning force of the motor, which can be defined as the equation for the power leaving the system:

$$P_{out} = \tau \cdot \omega \tag{3.3}$$

Tau is the measurement of the torque in the system in newton meters, and omega, is the angular speed of the motor measured in radians per second. The angular speed can be computed into a cartesian measurement using the equation below:

$$\omega = rpm \cdot \frac{2\pi}{60} \tag{3.4}$$

From the output power equation, we can rearrange the equation to generate the torque needed for our controller, however there are additional steps needed to compute this value without error. Ideally the power generated based on the input should be the same as the power that comes out, however in real life, some of that energy is lost to heat in this conversion. For simplicity, we can assume that the output power is around 75% of the input power, denoted to 0.75

$$P_{out} = P_{in} \cdot E \tag{3.5}$$

With all the equations needed, we can rearrange the equations to solve for the torque:

$$\tau = \frac{I \cdot V \cdot E \cdot 60}{rpm \cdot 2\pi} \tag{3.6}$$

$$\tau = \frac{3 \cdot 144 \cdot 0.75 \cdot 60}{3000 \cdot 2\pi} = 0.515\ N \cdot m$$

Finally, the force can be calculated by dividing the calculated torque over the radius of the provided motor.

$$F = \frac{\tau}{r} \tag{3.7}$$

$$F = \frac{0.515\ N \cdot m}{0.019\ m} = 27.1\ N$$

Now that we have a force provided from the magnetic bearing controller, we can integrate this force into our longitudinal stability controller parameters. To do this, we will integrate the provided force into the gain parameter by normalizing the force with the gain used in the previous simulation. We first implemented this with the elevator to angle of attack controller with the results below:

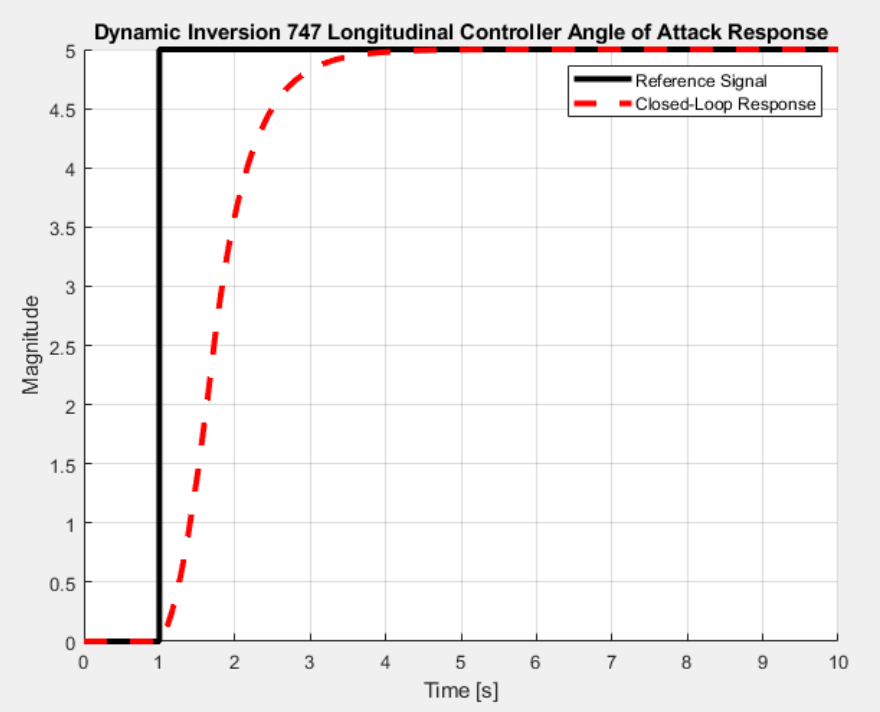

Figure 39: Longitudinal Controller AOA Response with magnetic bearing controller

For this test the same reference signal was used with and angle of attack of five degrees, which was taken as a unit step function measuring at one second. We tracked the angle of attack reference signal using the dynamic inversion controller at sea level altitude as shown above. Next we used the same controller performances to yield the best terms for settling time and maximum overshoot. From here we plotted the best fit results in the state space response both in an open loop and closed loop.

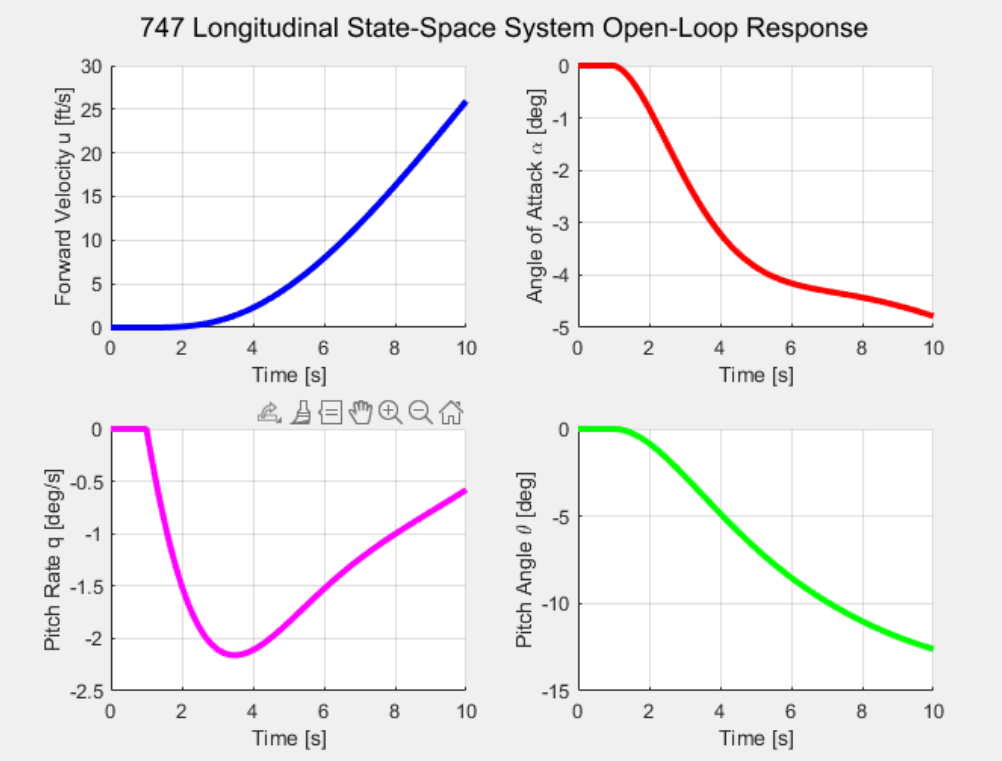

Figure 40: 747 longitudinal state space system open loop response with magnetic bearing controller

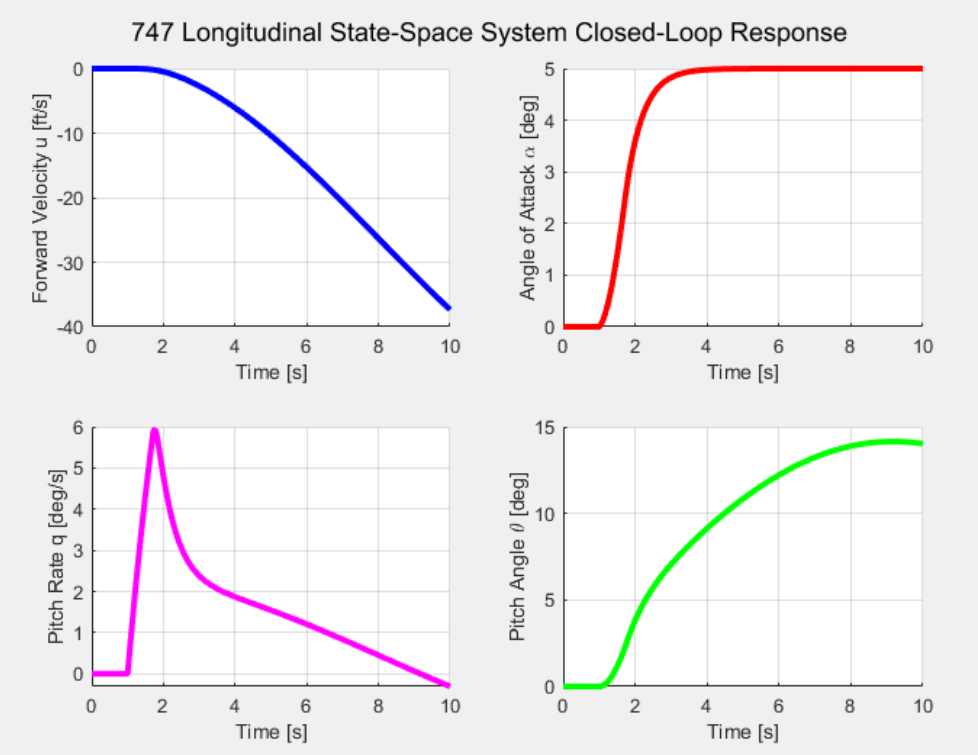

Figure 41: 747 longitudinal state space system closed loop response with magnetic bearing controller

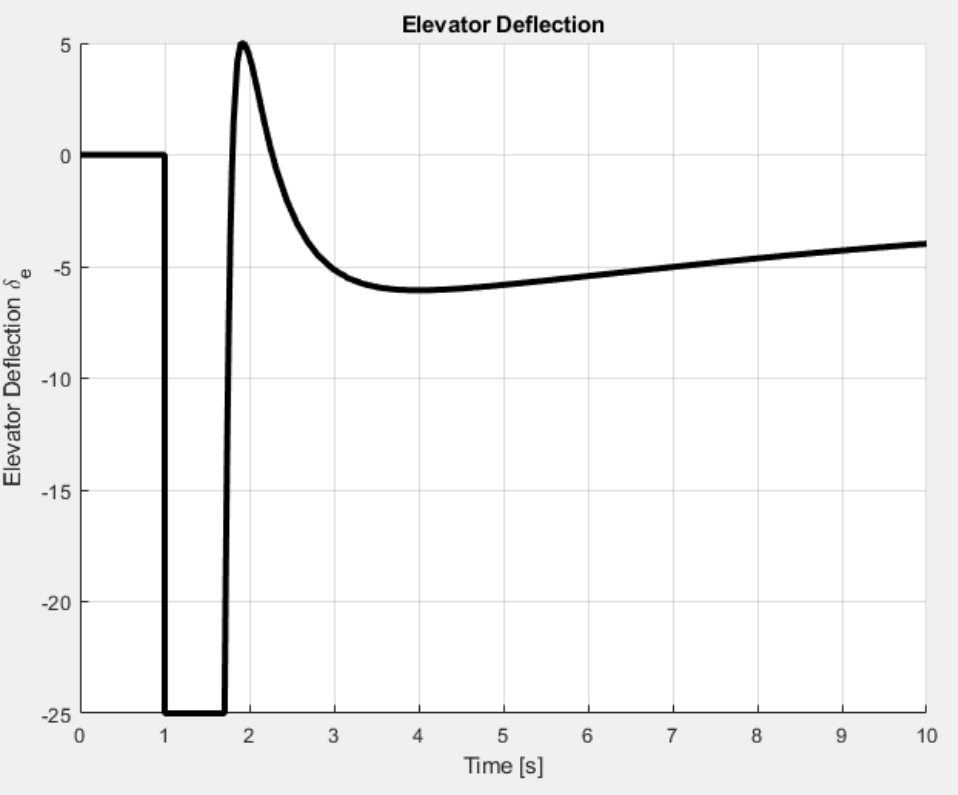

Figure 42: 747 dynamic inversion elevator deflection with magnetic bearing controller

When analyzing this controller, we can see that the closed loop response settles around 3.8 seconds, which though has a longer settling time compared to the initial controller, does not overshoot from the reference angle. This is a good result for longitudinal stability as this allows for minimal disturbances and a gradual stabilization in the change of angle of attack. Next, we compare the open and closed loop response to see that the forward velocity remains unchanged, but the angle of attack, pitch angle, and pitch rate graphs have a slight improvement. With the angle of attack we see that the response does not overshoot compared to the initial simulation, as well as taking a slightly longer time to reach the desired angle of attack. Next the pitch angle compared to previous tests shows a sharp stop after the five-degree angle after two seconds, then gradually increases in a linear rate. In the new simulation we see that it gradually increases from a zero-degree angle of attack and after 1,5 seconds the angle increases over the course of time. Lastly the pitch rate of the initial simulation shows a sharp rate increase of up to eight degrees per second until the two second time period, drops back to 2 degrees per second after one seconds then slowly decrease in pitch rate over the course of seven seconds after reaching he desired angle. This result is changed to where there is no sharp stop then gradual decline in the pitch rate after approximately three seconds, where instead, the pitch rate reaches only six degrees per second, at two seconds, drops to nearly two degrees per seconds after three seconds and gradually decrease to a minute negative pitch rate after 10 seconds. As a result this shows an overall improvement to the longitudinal stability comparing the elevator to the angle of attack.

With the application of the magnetic bearing controller, we also have the characteristic response of the aileron to roll angle. This uses the same reference angle of five degrees, with the results plotted below:

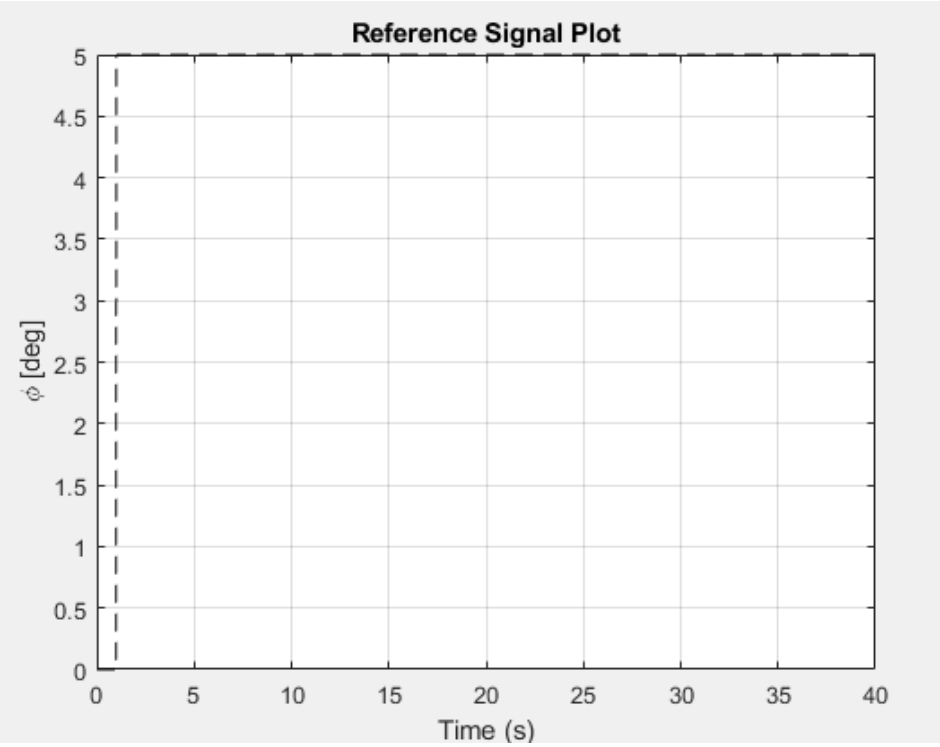

Figure 43: aileron to roll angle reference signal

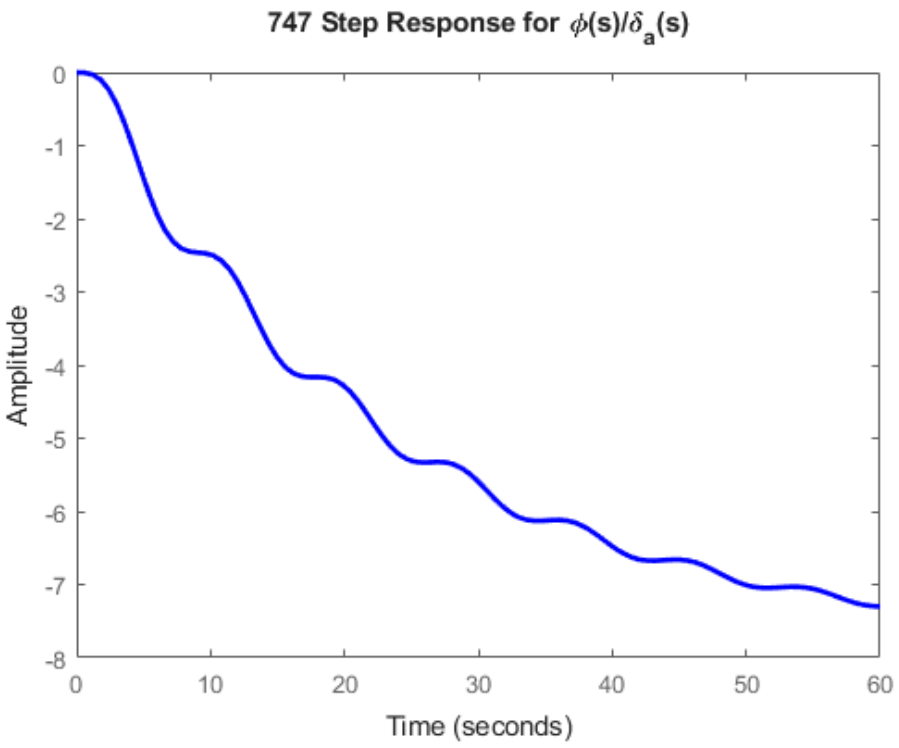

Figure 44: step response of roll angle of aileron deflection

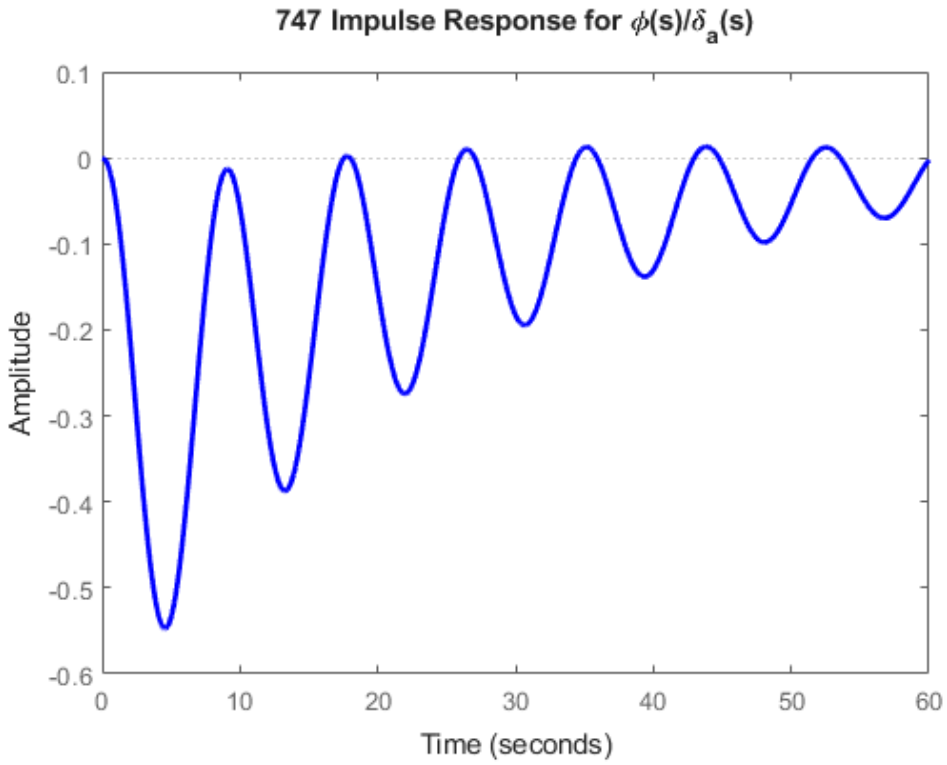

Figure 45:impulse response of roll angle to aileron deflection

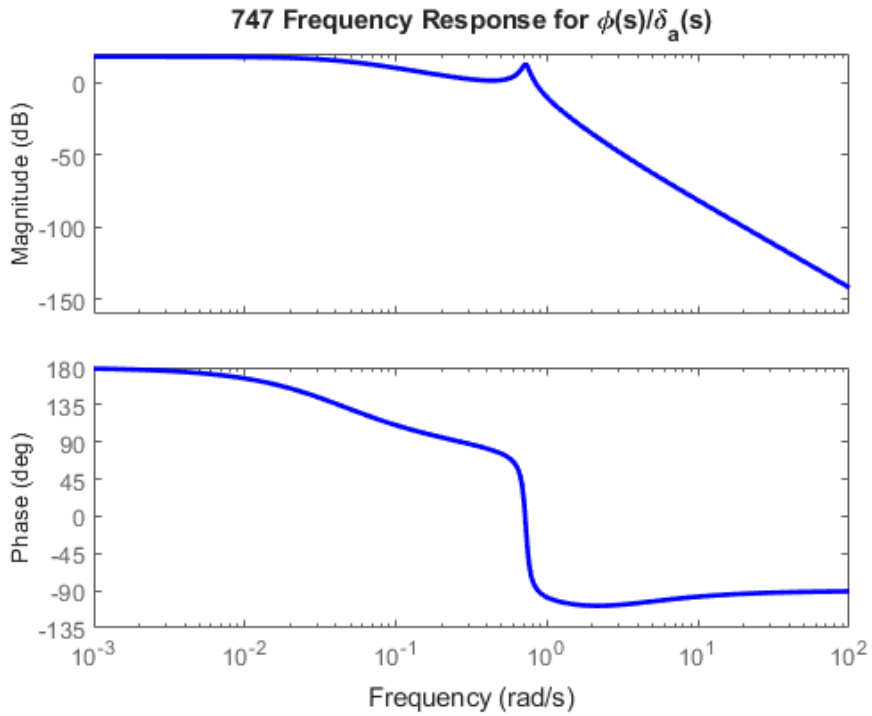

Figure 46: bode plot of the roll angle to aileron deflection

From these results we see that the step, impulse and bode responses are the same as the previous simulation, however for this simulation the aircraft roll changes are improved, using two additional methods of PID control. For this plot we use the Zeiger-Nichols, the modified Ziegler-Nichols and Tyreus-Luyben PID controller methods to determine which is best for the controller.

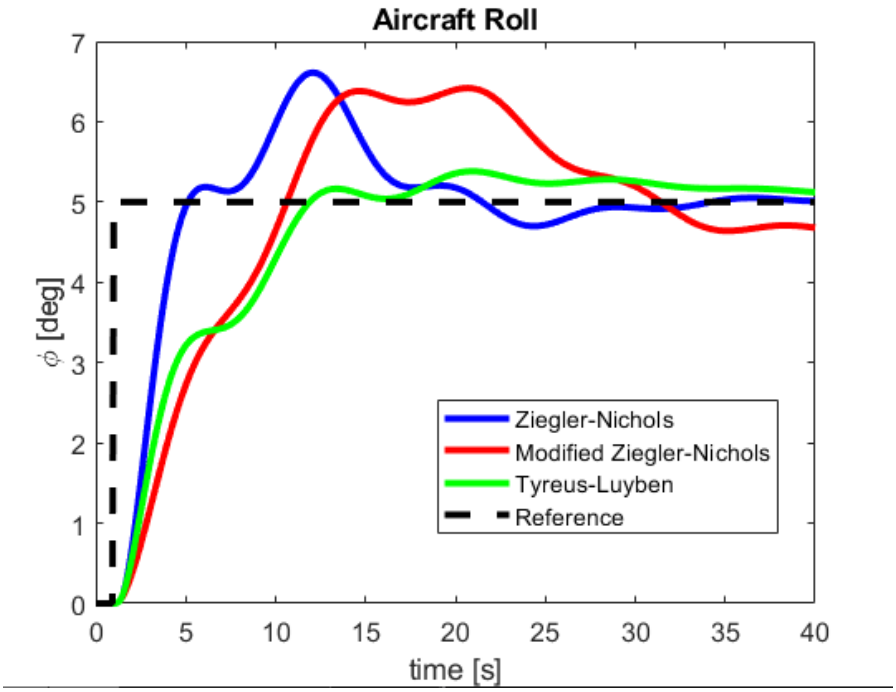

Figure 47: change in aircraft roll angle over time using PID with the magnetic bearing controller

3.32 Lateral Directional Stability with Permanent Magnetic actuator Integration yielding results

After implementing the magnetic bearing controller for the longitudinal stability controls, we are now integrating magnetic controls into the lateral directional stability controls. For these motions we are implementing the variable reluctance actuator to improve the controller's design. Since we have the necessary parameters from our linear magnetic actuator, we can implement these into our LQR controller with our modified measurements. The results of the modified rudder to yaw angle controller can be seen below:

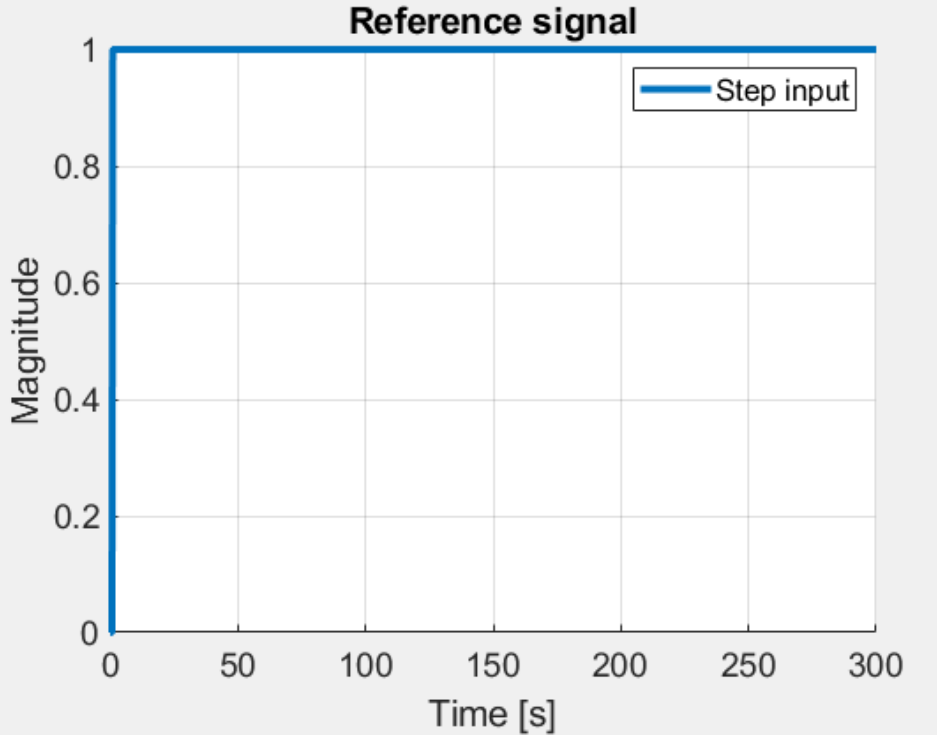

Figure 48: reference signal of LQR response

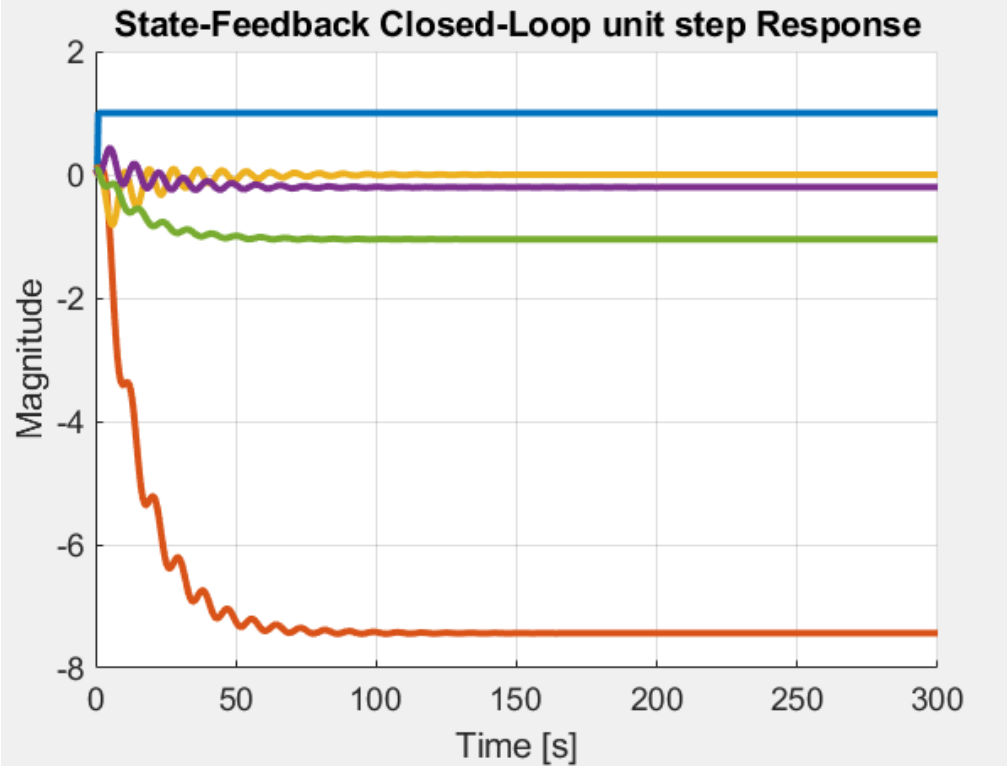

Figure 49: state feedback closed loop response of δr to ψ with LQR with a permanent magnet actuator

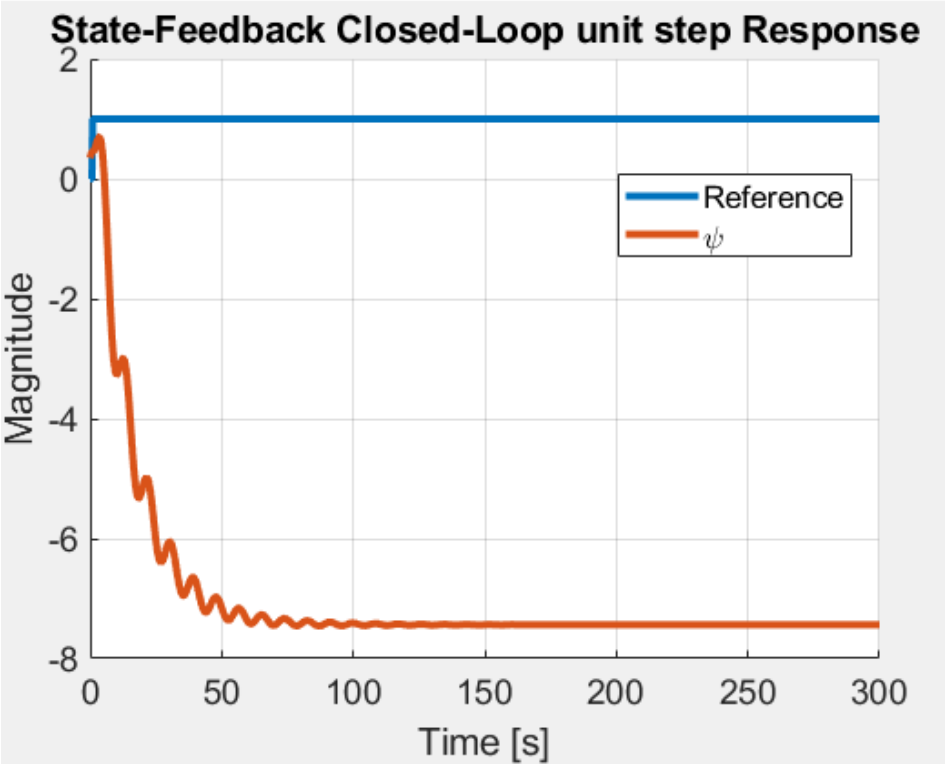

Figure 50: state feedback closed loop response of δr to ψ with LQR with a permanent magnet actuator

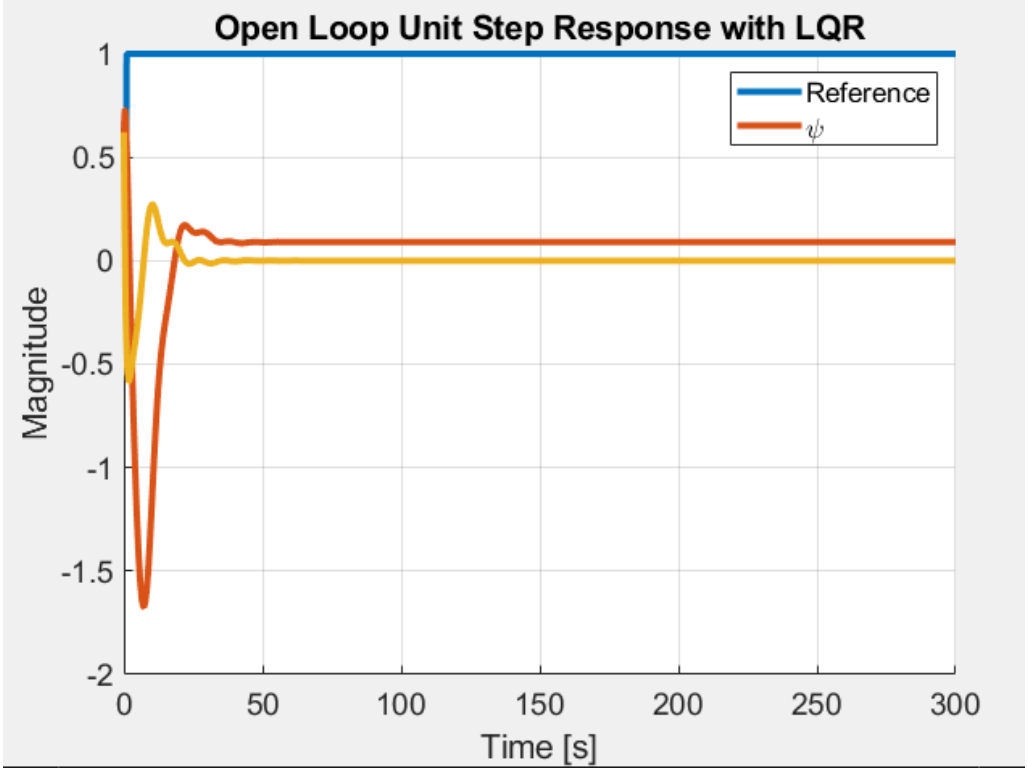

Figure 51: open loop response of δr to ψ angle with LQR with permanent magnet actuator

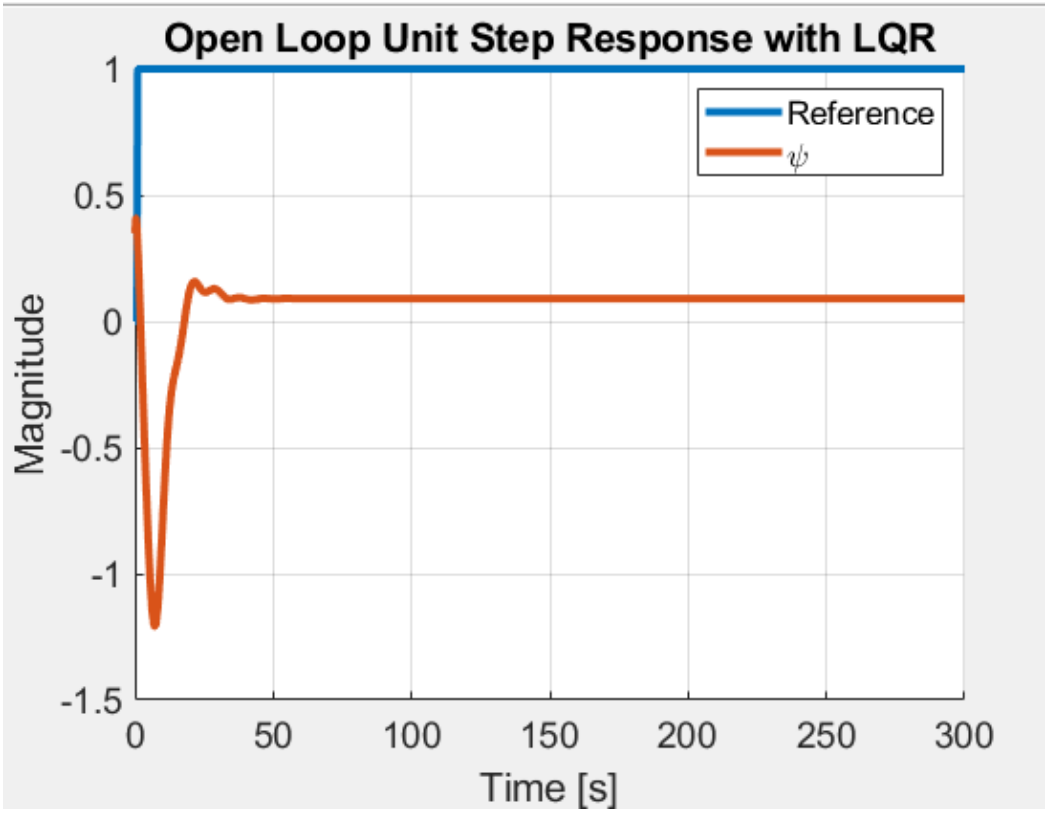

Figure 52: open loop response of δr to ψ angle with LQR with permanent magnet actuator

Lastly, we have the aileron to pitch angle optimization programmed and simulated with the results displayed below:

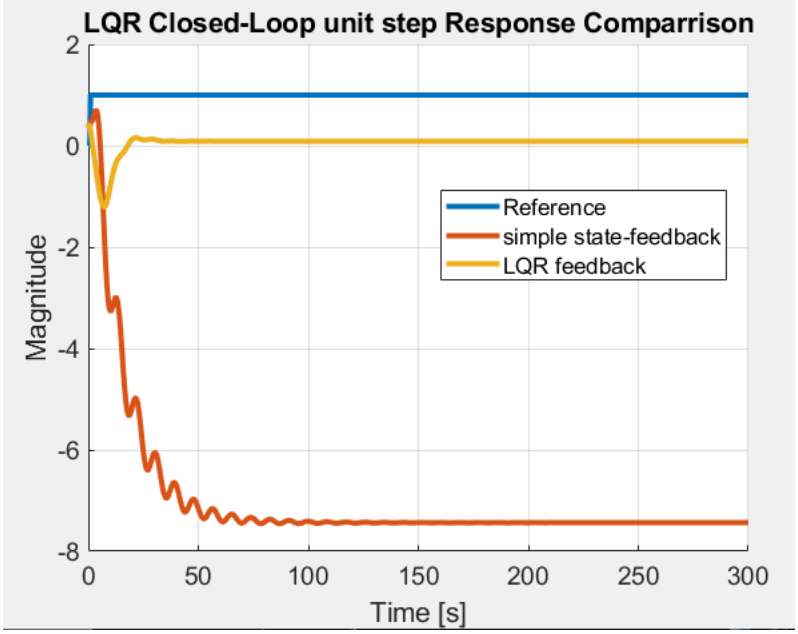

Figure 53: comparison of the closed loop LQR and state feedback with a permanent magnetic actuator

Finally, using the same reference angle of five degrees, we will plot the comparison and results of the elevator to pitch rate control. For this simulation we used the Hagglund-Astrom method for PID using the same parameters as the optimized controller. However, to match the actuator specifications we changed one of the parameters to zero to simulate a fast actuation that would be inputted.

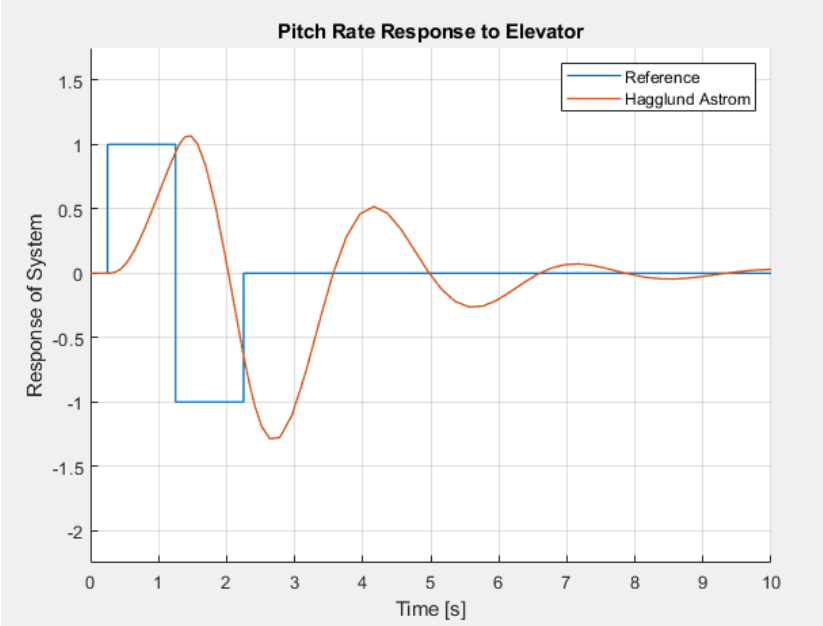

Figure 54: pitch rate response to elevator angle with a permanent magnetic actuator.

In the image above, the reference signal is one degree in both positive and negative directions, and the response shows that it reached the desired target, then takes around ten seconds to return to zero. At almost three seconds we can see it overshoots the desired angle by 0.35 degrees, then oscillates back to 0.52 degrees after four seconds. This shows that there is a significant improvement over the initial simulation where there were larger overshoot measurements in the initial test, as well as the simulation not normalizing after around 10 seconds. Thus, this adjustment proves to be a greater improvement to the lateral directional aircraft controls.

3.4 Discussion

With the results of the controller displayed above with analysis in each control surface, this shows that we have successfully implemented the magnetic controllers and actuators onto a controller designed to operate for the Boeing 747 aircraft. This shows that aircraft that use magnetic components and controllers can have an optimized and more efficient control system that potentially can use less energy, provide a smother flight experience, as well as become a far more reliable control system than the current aircrafts supply. This magnetic controller was designed on top of the initial control system using direct actuator controls from the literature review. The controller uses PID, LQR, and dynamic inversion for each control surface then potentially optimizes said system to account for faster inputs and greater precision, thus we see how well these results stabilize under the improved input. From the implementation of magnetic motors, and permanent actuators, we see a drastic improvement to the stability times for each control surface, with some having a fifty-percent decrease in the overall stabilizing time. After further testing and generating the results, there were some points and additional information that should be addressed in this report.

To start, we must keep in mind that the simulations and tests for this controller are done in a controlled environment to show that in theory, these controllers can work even for slight changes. This means that the controller has yet to be physically designed, pieced together and assessed in a lab environment. We may not know if these controllers can be used in modern aircraft, however this report shows that in theory it can happen. Additionally, we did these tests under sea level conditions, meaning that the parameters for the controller operating at 20,000 or 40,000 feet above sea level have not been conducted. Under additional research and physical assembly, these results may vary based on what parts are chosen, what type of controller is used, the programming language, and testing conditions. However, for now, this paper consists of the foundations of a controller with magnetic devices to be possible and potentially optimal for future use.

The next topic that must be discussed is the potential usability of this controller, and what types of aircraft this controller would be best suited for. To start, this magnetic controller is designed with the intent to be used with the Boeing 747 aircraft, which is a commercial jet made for linear travel from one destination to another. For commercial aircraft there are minimal changes in direction or angular deflection often with the intent to carry passengers and cargo for long periods of time. Realistically, we can see that for commercial planes a controller with faster input registration could be optimal and beneficial, but wide-body aircraft like the Boeings 747, 767, 777 and 787 do not necessarily benefit from these parameters. Though this can reduce the amount of turbulence these aircraft can handle, this improvement can be negligible regarding commercial travel.

In a hypothetical situation, we could measure the controllability and optimize this controller with the parameters of a modern stealth, or fighter jet in mind, such as the Lockheed-Martin F-14, and or F-35. However, due to the nature of these aircraft being top secret projects, obtaining the aircraft data for longitudinal and lateral directional derivatives of these aircraft would not be possible under any circumstances at college graduate level. As a result, using the Boeing 747 which was an aircraft initially released in 1968 was the optimal choice as it is still an aircraft in operation to this day.

Lastly, one topic that was often addressed when completing this project was practical, is this magnetic controller? Our results show that this controller in the right conditions can be optimal and if not, faster than traditional controllers, yet we may not have all the information necessary to determine that. Stated previously, this report entails the theoretical controller design for an aircraft, so this may not consist of all the proper parts and components needed to create a physical controller, thus a weight can is not narrowed down for the necessary parts. For these parts to be determined, further research must be developed and tested to conclude these practical assessments and need to be comparable to the performance of other control systems. The cost of this magnetic controller can also be another factor in practicality and will be notably compared to a fly-by-wire control system which is considered one of the most cost-effective, reliable and light weight control solutions in the aircraft industry. This is also used in commercial aircraft as well as in the 747 which is the aircraft we based the controller on. Overall, with the performance improvement that a magnetic controller may provide to commercial aircraft and potentially defense aircraft, we can see that the practical uses for it may be limited due to the cost-effectiveness of the controller compared to other alternatives.

3.5 Conclusions and Recommendations

3.5.1 Conclusion

This project has studied the utilization and potential implementation of magnetic controllers and actuators in commercial aircraft. This project was designed and proposed with the motivation of optimizing the current state of modern aircraft controllers to operate at an accelerated rate to improve upon precision, accuracy, and safety. This project proposed the use of modified magnetic controllers to observe and inspect any advantages and feasibility the controller would have for modern aircraft.

Using Newtons equations laws, we derived the translational and rotational equations of motion including the necessary equations for dynamics and modeling. From here we derived the six degrees of freedom equations, then reviewed the aerodynamic and stability parameters, which were incorporated into the aircraft equations of motion. Using the perturbation model we then linearized the equations of motions to allow for the equations to be replicated in MATLAB to simulate the initial input conditions of the aircraft before integrating the controller. The full characteristics and assumptions of the equations of motion are listed and presented in this report. Before integrating the magnetic controller, we optimized the controller design to provide a standard for stability measurements of an aircraft These controllers were simplified to measure four main measurements: the aileron to roll angle with a proportional integral derivative (PID) controller, the rudder to yaw angle controller using a linear quadratic regulator (LQR), elevator to pitch angle with

a PID controller, and the elevator to angle of attack with a dynamic inversion controller. This was then detailed and plotted in the report. Upon optimizing the controller without magnetic controllers and actuators, we analyzed what parameters needed to be improved to meet the requirements for integrating the controller. From the analysis we then analyzed what types of magnetic controller best suit each type. The parameters and characteristics were labeled and listed in the report and determined what needs to be changed and added to improve the overall controller design to accommodate for these controllers. After integrating the parameters in the MATLAB code, we then plotted and presented the results of the magnetic implementation, showing the overall effectiveness of the controller. With the controller implementation we showcased an improved response time to the controller and faster stabilization time that a commercial aircraft will have with a new controller based on magnetic inputs.

With the analysis of the controller and optimization, this project provides a solid case as to implementing a prototype of magnetic controllers on an aircraft. This shows an effective solution for modern aircraft with traditional controls, which can provide a safe and efficient method of aircraft control.

3.5.2 Recommendations

This project showcased a theoretical controller which can be implemented into modern day aircraft. This showed promising results that this can work, however there are some caveats to the results presented, and the complexity of implementing this controller in a physical system remains unknown. With some additional information written in the discussion, there is a list of possible areas and topics that can be investigated and addressed to potentially bring this controller into a feasible production:

- Provide simulations for an aircraft above sea-level conditions, including 20,000 feet, and 40,000 feet
- Additional derivation for an aircraft with changes to the geometry
- Wind tunnel testing of stability reaction and changes compared between fly-by-wire and newer controls
- Physical tests, either small scale models or full-scale tests, for implementing magnetic controllers
- Additional tests for implementing magnetic actuators control surfaces for bearing controllers and permanent magnet actuators
- Design the controller with the intent of optimizing defense aircraft

With these parameters implemented for improving this controller, there may be a chance to one day see an aircraft with magnetic controllers take flights.

References

[1] Parkinson, B., Kasdin, N., "A magnetic attitude control system for precision pointing of the rolling GP-B spacecraft" *Acta Astronautica,* Vol. 21, no. 6–7, pp. 477-486, January 1990, Retrieved 12 February 2024 https://doi.org/10.1016/0094-5765(90)90065-S.

[2] Kimura, K., Shoji, Y., Satoh, S., & Yamada, K. "Attitude control experiment of a spinning spacecraft using only magnetic torquers" *Advances in Space Research*, Vol. 71, No. 12,pp. 5386– 5399 30 January 2023. Retrieved 12 February 2024 from https://doi-org.libaccess.sjlibrary.org/10.1016/j.asr.2023.02.018

[3] Porras-Hermoso, A., Piqueras, J., Cubas, J., & Roibás-Millán, E. "On-orbit performance analysis of spinning spacecraft magnetic control laws, Application to the UPMSat-2 mission" *Measurement*, Vol. 225, N.PAG, 28 November 2023, Retrieved 12 February 2024 from https://doiorg.libaccess.sjlibrary.org/10.1016/j.measurement.2023.113962

[4] Atzampou, P., Meijers, P. C., Tsouvalas, A., & Metrikine, A. V. "Contactless control of suspended loads for offshore installations: Proof of concept using magnetic interaction*" Journal of Sound & Vibration*, Vol. 575, N.PAG, 5 January 2024, Retrieved 12 February 2024 from https://doiorg.libaccess.sjlibrary.org/10.1016/j.jsv.2024.118246

[5] Sun, J., Zhao, J., & Bai, J. "Gimbal Angular Velocity Feedforward Method for Magnetically Suspended Control Moment Gyro with Hybrid Magnetic Bearing" *Mechatronics,* Vol. 84, N.PAG, 30 March 2022, Retrieved 13 February 2024 from https://doi.org.libaccess.sjlibrary.org/10.1016/j.mechatronics.2022.102804

[6] Tashiro, K., Yokota, S., Asai, K., Nonomura, T., "Experimental investigation of strut effects on slanted cylinder afterbody aerodynamics using magnetic suspension and balance system" *Experimental Thermal and Fluid Science*, Vol. 148, N.PAG, 23 May 2023, Retrieved 13 February 2024 from https://doi-org.libaccess.sjlibrary.org/10.1016/j.expthermflusci.2023.110952

[7] Nakai, T., "Relationship of Magnetic Domain and Permeability for Clustered Soft Magnetic Narrow Strips with In-Plane Inclined Magnetization Easy Axis on Distributed Magnetic Field" *Sensors*, Vol. 24, No. 2, pp. 706 22 January 2024, Retrieved 13th February 2024 from https://doi-org.libaccess.sjlibrary.org/10.3390/s24020706

[8] Liu, Z., Cao, X., & Cai, J, "A Magnetic Bearing Switched Reluctance Motor With Simultaneous Excitation by a Modified Half-Bridge Converter*." IEEE Transactions on Magnetics*, Vol. 55, No. 10, pp. 1–5, October 2019, Retrieved 13 February 2024 from https://doi-org.libaccess.sjlibrary.org/10.1109/TMAG.2019.2921725

[9] Wang, D., Wang, J., & Li, L. "Electromagnetic field/hypersonic flow field coupled algorithm and its application in the magnetic controlled inlet design" *Aerospace Science & Technology,* Vol. 126, N.PAG 25 April 2022, Retrieved 13 February 2024 from https://doi-org.libaccess.sjlibrary.org/10.1016/j.ast.2022.107598

[10] Jiang, H., Liu, J., Che, X., Du, Y., Huang, W., Ding, F., Zhang, T., "Magnetic field control of high-enthalpy shock wave/boundary-layer interactions using a fully implicit thermochemical non-equilibrium solver*," Aerospace Science and Technology,* Vol. 141, N.PAG, 11 July 2023, Retrieved 13 February 2024, from https://doi.org/10.1016/j.ast.2023.108507.

[11] CHU, L., Li, Q., Gu F., Du, X., HE, Y., Deng, Y., "Design, modeling, and control of morphing aircraft: A review" *Chinese Journal of Aeronautics*, Vol. 35, No. 5, pp. 220-246, 26 October 2021, Retrieved 13 February 2024 from https://doi.org/10.1016/j.cja.2021.09.013.

[12] Lee, I.H., Khim, Y.G., et al. "Controlling the magnetic properties of layered Cr2Te3 thin films via ex-situ annealing" *Applied Surface Science*, Vol. 648, N.PAG, 3 December 2023, Retrieved 14 February 2024 from https://doi.org/10.1016/j.apsusc.2023.159057.

[13] Li, W., Zou, W., Fu, J., Gao, F., Yu, M., "Development of an antivibration aircraft model support system with magnetorheological annular squeeze dampers for wind tunnel" *Mechanical Systems and Signal Processing*, Vol. 202, N.PAG, 25 August 2023, Retrieved 14 February 2024 from https://doi.org/10.1016/j.ymssp.2023.110663.

[14] Dasilva, Marcelo "Aircraft Rotations." *NASA*, 2022. Retrieved 17 February 2024 from ,<https://www1.grc.nasa.gov/beginners-guide-to-aeronautics/aircraft-rotations/>

[15] Chen, K., Xiao, L., Zhang, B., Yang, M., Yang, X., & Guo, X. "Decoupling Algorithm for Online Identification of Inductance in Permanent Magnet Synchronous Motors Based on Virtual Axis Injection Method and Sensorless Control" *Energies* Vol. 17, No. 24, N.PAG, 13 December 2024, Retrieved 8 January 2025 from https://doi-org.libaccess.sjlibrary.org/10.3390/en17246308

[16] Ganesh, M., Lee, S. R., Jeong, J. H., & Joo, Y. H. "An improved direct predictive speed control for three-level NPC converter fed PMSG-based offshore wind turbine system with minimum computation" *Ocean Engineering*, Vol. 314, No. 2, N.PAG, 15 November 2024, Retrieved 8 January 2025 https://doi-org.libaccess.sjlibrary.org/10.1016/j.oceaneng.2024.119705

[17] Vashisht, R. K. "Vibration control of flexible rotors using a passive magnetic device working on the principle of electromagnetic shunt damping" *Mechatronics*, Vol. 90, N.PAG, 21 December 2022, Retrieved 8 January 2025 from https://doi-org.libaccess.sjlibrary.org/10.1016/j.mechatronics.2022.102931

[18] Qian, J., Zhao, C., Pan, N., & Xie, T. "Design and performance analysis of permanent magnet linear synchronous motor." *Journal of Intelligent & Fuzzy Systems*, Vol.40, No. 4, pp. 7811–7818, 12 April 2021, Retrieved 8 January 2025 from https://doi-org.libaccess.sjlibrary.org/10.3233/JIFS-189602

[19] Andre, "Automatic PID Tuning.zip," *MATLAB Central File Exchange* N.PAG, 5 Jun 2014, Retrieved 12 February 2025 from https://www.mathworks.com/matlabcentral/fileexchange/46864-automatic-pid-tuning-zip.

[20] Spinelli, W., "AutotunerPID Toolkit," *MATLAB Central File Exchange* N.PAG, 20 Jun 2009, Retrieved 12 February 2025 from https://www.mathworks.com/matlabcentral/fileexchange/4652-autotunerpid-toolkit.

[21] Hornsey, S., "A Review of Relay Auto-tuning Methods for the Tuning of PID-type Controllers," *Reinvention: an International Journal of Undergraduate Research*, vol. 5, October 2012

[22] Gysen, B.L.J, Paulides, J, Lomonova, E.A., Vanderput, A.J.A. "Analytical and Numerical Techniques for Solving Laplace and Poisson Equations in a Tubular Permanent-Magnet Actuator: Part I. Semi-Analytical Framework", *IEEE Transactions on Magnetics*, vol 44, pp. 1751-1760, 17 June 2008, Retrieved 14 March 2025 10.1109/TMAG.2008.922416

[23] Matan, "Linear magnetic actuator," *Electricity-Magnetism, Oct* 2023, N.PAG, Retrieved 14 March 2025 from https://www.electricity-magnetism.org/linear-magnetic-actuator/.

[24] NA, "High-power voice coil actuators: Efficient Control for demanding applications," *Magnetic Innovations* N.PAG, N.D., Retrieved 14 March 2025 https://www.magneticinnovations.com/products/high-speed-linear-actuator/moving-magnet-actuator-5536/.

[25] NA, "Linear actuator with moving magnet offers precise positioning," *Magnets By HSMAG*, N.PAG, 11 September 2021, Retrieved 14 March 2025 from https://www.hsmagnets.com/blog/linear-actuator-with-moving-magnet-offers-precise-positioning/.

[26] NA, "Force controlled Smart Linear Motors," Iris Dynamics, N.PAG, 1 November 2022, Retrieved 15 March 2025 from https://irisdynamics.com/articles/magnetic-force-feedback.

[27] Hawkins, L., and Khatri, R., "How a magnetic bearing controller works," *Calnetix Technologies,* N.PAG, Oct 2019, Retrieved 14 March 2025 from https://www.calnetix.com/sites/default/files/2020-04/How%20Magnetic%20Bearing%20Controller%20Works.pdf

[28] NA, "DC Servomotor 80mm Frame Size, 61.1 in.-lbs. Maximum Torque PN 5082N33," *McMaster-Carr* N.PAG, N.D, Retrieved 15 March 2025 from https://www.mcmaster.com/5082N33/.

Appendices

Appendix A: Aircraft Dynamic Derivation

Translational Equations of motion

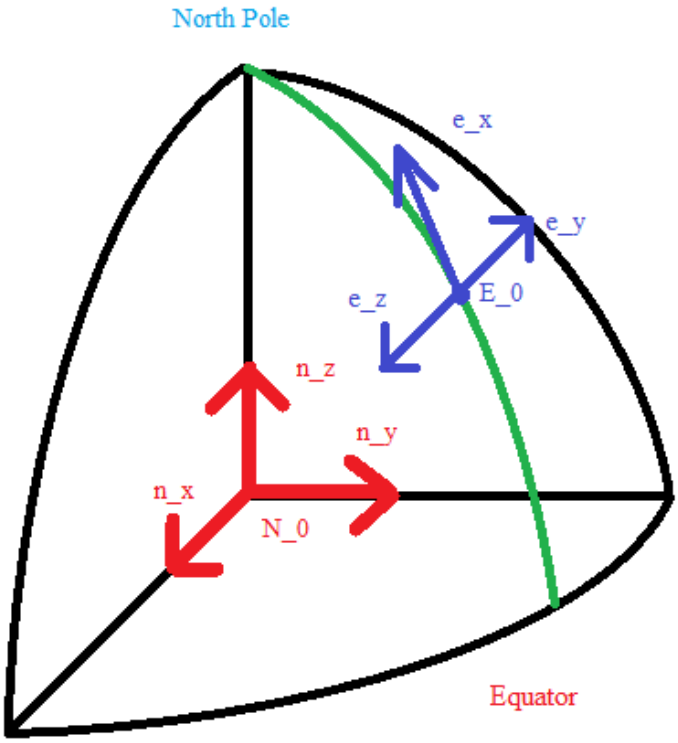

Assume:

- N Frame is the same as the E frame due to "Short Flight Time"
- Apply Newtons Second Law:

$$\sum \overrightarrow{F^B} = \frac{Ed}{dt}\left(mV^{E/B}\right) = m \cdot \frac{Ed}{dt}\left(\vec{V}^{E/B}\right) + \left(\vec{\omega}^{E/B} \times \vec{V}^{E/B}\right)$$

Recall:

$$\vec{V}^{E/B} = u\hat{b}_x + v\hat{b}_y + w\hat{b}_z$$

$$\vec{w}^{E/B} = P\hat{b}_x + Q\hat{b}_y + R\hat{b}_z$$

Thus,

$$\sum F = m \cdot \left[\begin{bmatrix} \dot{U}_{b_{\hat{x}}} \\ \dot{V}_{b_{\hat{y}}} \\ \dot{W}_{b_{\hat{z}}} \end{bmatrix} + \begin{bmatrix} \hat{b}_x & \hat{b}_y & \hat{b}_z \\ P & Q & R \\ U & V & W \end{bmatrix}\right]$$

And $$m \cdot \left[\begin{bmatrix} \dot{U}_{b_{\hat{x}}} \\ \dot{V}_{b_{\hat{y}}} \\ \dot{W}_{b_{\hat{z}}} \end{bmatrix} + \begin{bmatrix} \hat{b}_x & \hat{b}_y & \hat{b}_z \\ P & Q & R \\ U & V & W \end{bmatrix} \right] = \hat{b}_x(QW - RV) - \hat{b}_y(PW - RU) + \hat{b}_z(PV - QU)$$

Translational Equations of Motion (EOM): $$\begin{cases} \hat{b}_x: F_x = m(\dot{U} + QW - RV) \\ \hat{b}_y: F_y = m(\dot{V} + RU - PW) \\ \hat{b}_z: F_z = m(\dot{W} + PV - QU) \end{cases}$$

Rotational Equations of Motion

$$\sum \vec{M} = \frac{Ed}{dt}\left(\vec{H}^{E/\frac{B}{B_0}}\right) = \frac{Bd}{dt}\left(\vec{H}^{E/\frac{B}{B_0}}\right) + \left(\omega^{E/B} \times H^{E/\frac{B}{B_0}}\right)$$

Where: $$\vec{H}^{E/\frac{B}{B_0}} = I \times \omega^{E/B} = \begin{bmatrix} I_{xx} & \cancel{I_{xy}} & I_{xz} \\ \cancel{I_{xy}} & I_{yy} & \cancel{I_{yz}} \\ I_{xz} & \cancel{I_{yz}} & I_{zz} \end{bmatrix} \begin{bmatrix} P \\ Q \\ R \end{bmatrix}$$

With the diagonal values in the matrix canceling out:

$$\vec{H}^{E/\frac{B}{B_0}} = (I_{xx}P + I_{xz}R)\hat{b}_x + (I_{yy}Q)\hat{b}_y + (I_{xz}P + I_{zz}R)\hat{b}_z$$

Thus: $$\sum \vec{M}^B = \frac{\boldsymbol{Bd}}{\boldsymbol{dt}}\left(\vec{\boldsymbol{H}}^{\boldsymbol{E}/\frac{\boldsymbol{B}}{\boldsymbol{B_0}}}\right) + \vec{\boldsymbol{\omega}}^{\boldsymbol{E/B}} \times \vec{H}^{E/\frac{B}{B_0}}$$

Where: $$\frac{\boldsymbol{Bd}}{\boldsymbol{dt}}\left(\vec{\boldsymbol{H}}^{\boldsymbol{E}/\frac{\boldsymbol{B}}{\boldsymbol{B_0}}}\right) = \left(\boldsymbol{I_{xx}\dot{P} + I_{xz}\dot{R}}\right)\hat{\boldsymbol{b}}_{\boldsymbol{x}} + \left(\boldsymbol{I_{yy}\dot{Q}}\right)\hat{\boldsymbol{b}}_{\boldsymbol{y}} + \left(\boldsymbol{I_{xz}\dot{P} + I_{zz}\dot{R}}\right)\hat{\boldsymbol{b}}_{\boldsymbol{z}}$$

And $$\vec{\boldsymbol{\omega}}^{\boldsymbol{E/B}} \times \vec{H}^{E/\frac{B}{B_0}} = \begin{bmatrix} \hat{b}_x & \hat{b}_y & \hat{b}_z \\ P & Q & R \\ I_{xx}P + I_{xz}R & I_{yy} & I_{xz}P + I_{zz}R \end{bmatrix}$$

Combining the terms we get the rotational equations of motion:

$$\begin{cases} \hat{\boldsymbol{b}}_{\boldsymbol{x}}: \boldsymbol{M_x} = I_{xx}\dot{P} + I_{xz}\dot{R} + (I_{zz} - I_{yy})QR + I_{xz}PQ \\ \hat{\boldsymbol{b}}_{\boldsymbol{y}}: \boldsymbol{M_y} = I_{xx}\dot{P} + I_{xz}\dot{R} + (I_{zz} - I_{yy})QR + I_{xz}PQ \\ \hat{\boldsymbol{b}}_{\boldsymbol{z}}: \boldsymbol{M_z} = I_{xx}\dot{P} + I_{xz}\dot{R} + (I_{zz} - I_{yy})QR + I_{xz}PQ \end{cases}$$

NASA Standard Euler Angles

Ψ (Psi) – Yaw angle about $\hat{e}_z$

Θ (Theta) – Pitch angle about $\hat{e}_y$

Φ(Phi) – Roll angle about $\hat{e}_x = \hat{b}_x$

Since we know that $\hat{e}_x = \hat{b}_x$, we can represent the relationship on a 2-dimensional plane:

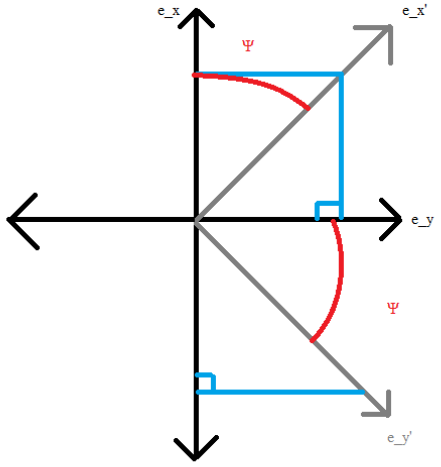

	e_x	e_y	e_z
e_x'	C_Ψ	S_Φ	0
$e_{y'}$	$-S_\Psi$	C_Φ	0
e_z'	0	0	1

Thus the relations between angles can be summarized as: $\begin{cases} \hat{e}_x{}' = C_\Psi \hat{e}_x + S_\Phi \hat{e}_y \\ \hat{e}_y = -S_\Psi \hat{e}_x + C_\Phi \hat{e}_y \end{cases}$

With the angular relations simplified, we have our complete translational and rotational equations of motion, as well as the kinematic differential equations:

Translational EOMS (Force Equations)

$$-mgS_\theta + X + X_T = m(\dot{U} + QW - RV)$$
$$mgC_\theta + Y + Y_T = m(\dot{V} + RU - PW)$$
$$mgC_\theta C_\phi + Z + Z_T = m(\dot{W} + PV - QU)$$

Rotational Equations of Motion (Moment Equations)

$$\mathcal{L} + \mathcal{L}_T = I_{xx}\dot{P} + I_{xz}\dot{R} + (I_{zz} - I_{yy})QR + I_{xz}PQ$$
$$\mathcal{M} + \mathcal{M}_T = I_{yy}\dot{Q} + (I_{xx} - I_{zz})PR + (R^2 - P^2)I_{xz}$$
$$\mathcal{N} + \mathcal{N}_T = I_{xz}\dot{P} + I_{zz}\dot{R} + (I_{yy} - I_{xx})PQ - I_{xz}QR$$

Recall that $\vec{w}^{E/B} = P\hat{b}_x + Q\hat{b}_y + R\hat{b}_z$ which can also be expressed as $\vec{w}^{E/B} = \dot{\Psi}\hat{e}_z + \theta\hat{e}_y + \dot{\Phi}\hat{b}_x$ and can write the kinematic differential equations as below:

$$\begin{bmatrix} P \\ Q \\ R \end{bmatrix} = \begin{bmatrix} 1 & 0 & -\sin\theta \\ 0 & \cos\phi & \sin\phi\cos\theta \\ 0 & -\sin\phi & \cos\theta\cos\phi \end{bmatrix} \begin{bmatrix} \phi \\ \dot{\theta} \\ \dot{\psi} \end{bmatrix}$$

Linearization of EOMs

We can define the following sub notations as:

$$\text{Translational Velocities: } \begin{cases} U = U_1 + u \\ V = V_1 + v \\ W = W_1 + w \end{cases} \qquad \text{Angular Velocities: } \begin{cases} P = P_1 + p \\ Q = Q_1 + q \\ R = R_1 + r \end{cases}$$

$$\text{Euler Angles: } \begin{cases} \Psi = \Psi_1 + \psi \\ \Theta = \Theta_1 + \theta \\ \Phi = \Phi_1 + \phi \end{cases} \qquad \text{Aero Forces: } \begin{cases} X = X_1 + f_x \\ Y = Y_1 + f_y \\ Z = Z_1 + f_z \end{cases}$$

$$\text{Thrust Force: } \begin{cases} X_T = X_{T_1} + f_{T_x} \\ Y_T = Y_{T_1} + f_{T_y} \\ Z_T = Z_{T_1} + f_{T_z} \end{cases} \qquad \text{Aero Moments: } \begin{cases} \mathcal{L} = \mathcal{L}_1 + \ell \\ \mathcal{M} = \mathcal{M}_1 + m \\ \mathcal{N} = \mathcal{N}_1 + n \end{cases}$$

$$\text{Thrust Moments: } \begin{cases} \mathcal{L}_T = \mathcal{L}_{T_1} + \ell_T \\ \mathcal{M}_T = \mathcal{M}_{T_1} + m_T \\ \mathcal{N}_T = \mathcal{N}_{T_1} + n_T \end{cases}$$

Where the capital denotes the steady state term and the lowercase denotes the perturbed term.

We will need the following trigonometric identities to linearize the EOMs:

$$\sin(a + b) = \sin a \cos b + \cos a \sin b$$
$$\cos(a + b) = \cos a \cos b - \sin a \sin b$$

Small angle approximation: when angle a is immesurably small; $\begin{cases} \cos \alpha \approx 1 \\ \sin a \approx a \\ \tan a \approx a \end{cases}$ where a is the angle in radians

$\dot{u}$:

$$-mgS_\theta + X + X_T = m\left(\dot{U} + QW - RV\right)$$

$$-mg \sin(\Theta_1 + \theta) + (X_1 + f_x) + \left(X_{T_1} + f_{T_x}\right)$$
$$= m\left(\left(\dot{U}_1 + \dot{u}\right) + (Q_1 + q)(W_1 + w) - (R_1 + r)(V_1 + v)\right)$$

$$ms \sin \Theta_1 \cancel{\cos\theta} + \cos \Theta_1 \cancel{\sin\theta} + X_1 + f_x X_{T_1} + f_{T_x} =$$

$$m\left(\dot{U}_1 + \dot{u} + Q_1 W_1 + Q_1 w + q W_1 + \cancel{qw} + R_1 V_1 + r V_1 + v R_1 + \cancel{rv}\right)$$

Simplify $\sin\theta = \theta, \cos\theta = 1, qw = 0\ rv = 0$

From here we can simplify the equations even further

$$\cancel{-mg\sin\Theta_1} - mg\theta\cos\Theta_1 + x_1 + f_x + X_{T_1} + f_{T_x}$$

$$= \cancel{m\left(\dot{U}_1 + Q_1W_1 + R_1V_1\right)} + m(\dot{u} + Q_1w + qW_1 + rV_1 + vR_1)$$

Since $-mgS_\theta + X + X_T = m\left(\dot{U}_1 + Q_1W_1 + R_1V_1\right)$ in steady state conditions, we can cancel the component of the equation.

Linearization Eq.

$$-mg\theta\cos\Theta_1 + x_1 + f_x + X_{T_1} + f_{T_x} = m(\dot{u} + Q_1w + qW_1 + rV_1 + vR_1)$$

Straight and level Steady State flight conditions

- No steady state lateral velocity ($V_1=0$)
- No steady state vertical velocity ($W_1=0$)
- No steady state roll angle ($\Phi_1 = 0$)
- No steady state angular velocity ($P_1 = Q_1 = R_1 = \Phi_1 = \Theta_1 = \Psi_1 = 0$)

Apply Straight and level conditions (SS) to $\dot{U}$ equations

$$-mg\theta\cos\Theta_1 + x_1 + f_x + X_{T_1} + f_{T_x} = m(\dot{u} + \cancel{Q_1w} + \cancel{qW_1} + \cancel{rV_1} + \cancel{vR_1})$$

Steady State Simplification: $-mg\theta cos\Theta_1 + f_x + f_{T_x} = m(\dot{u})$

$\dot{w}$

$$mgC_\theta + Y + Y_T = m\left(\dot{V} + RU - PW\right)$$

$$mg\cos(\Theta_1 + \theta) + \left(Y_1 + f_y\right) + \left(Y_{T_1} + f_{T_y}\right)$$
$$= m\left(\left(\dot{V}_1 + v\right) + (R_1 + r)(U_1 + u) - (P_1 + p)(W_1 + w)\right)$$

$$mgcos(\Theta_1) + Y_1 + Y_{T_1} + f_y + f_{T_y} - mg\theta sin(\Theta_1)$$
$$= m(\dot{V}_1 + \dot{v} + RU_1 + R_1u + U_1r - P_1W_1 - P_1w - W_1p)$$

$$mgcos(\Theta_1) + Y_1 + Y_{T_1} + f_y + f_{T_y} - mg\theta sin(\Theta_1)$$

$$mg(-\theta\sin\Theta_1)\cos\Phi_1 - \phi\sin\Phi\cos\Theta_1 + f_z = m(\dot{w} - U_1q - uQ_1 + V_1p + vP_1)$$

Steady State Simplification: $-mg\theta\cos\Theta_1 + f_z + f_{T_z} = m(\dot{w} + U_1q)$

$\dot{q}$

$$mgC_\theta C_\phi + Z + Z_T = m\left(\dot{W} + PV - QU\right)$$

$$-mg\theta cos(\Phi_1)sin(\Theta_1) - mg\phi cos(\Theta_1)sin(\Phi_1) + f_z + f_{T_z} = m[\dot{w} + P_1 v + pV_1 - Q_1 u - qU_1]$$

$$mgsin(\Theta_1) + Z_1 + Z_{T_1} = m(P_1 V_1 - Q_1 U_1)$$

$$mg\theta\cos(\Theta_1) + f_z + f_{T_z} = m(\dot{w} + P_1 v + pV_1 - Q_1 u - qU_1)$$

Steady State Simplification: $mg\theta\cos(\Theta_1) + f_z + f_{T_z} = m(\dot{w} + pV_1 - qU_1)$

$\dot{\Phi}$ $$\mathcal{L} + \mathcal{L}_T = I_{xx}\dot{P} + I_{xz}\dot{R} + (I_{zz} - I_{yy})QR + I_{xz}PQ$$

$$L_1 + l + L_{T_1} + l_T = I_{xx}\dot{p} + I_{xz}\dot{r} + (I_{zz} - I_{yy})(Q_1 + q)(R_1 + r) + I_{xz}(P_1 + p)(Q_1 + q)$$

$$L_1 + l + L_{T_1} + l_T = I_{xx}\dot{p} + I_{xz}\dot{r} + (I_{zz} - I_{yy})(Q_1 R_1 + Q_1 r + qR_1) + I_{xz}(P_1 Q_1 + P_1 q + pQ_1)$$

$$L_1 + L_{T_1} = (I_{zz} - I_{yy})Q_1 R_1 + I_{xz}P_1 Q_1$$

$$l + l_T = I_{xx}\dot{p} + I_{xz}\dot{r} + (I_{zz} - I_{yy})(Q_1 r + qR_1) + I_{xz}(P_1 q + pQ_1)$$

Steady State Simplification: $l + l_T = I_{xx}\dot{p} + I_{xz}\dot{r}$

$\dot{\Theta}$ $$\mathcal{M} + \mathcal{M}_T = I_{yy}\dot{Q} + (I_{xx} - I_{zz})PR + (R^2 - P^2)I_{xz}$$

$$M_1 + m + M_{T_1} + m_T = I_{yy}\dot{q} + (I_{xx} - I_{zz})(P_1 + p)(R_1 + r) + I_{xz}((R_1 + r)^2 - (P_1 + p)^2)$$

$$m + m_T = I_{yy}\dot{q} + (I_{xx} - I_{zz})(P_1 r + pR_1) + I_{xz}(2R_1 r - 2P_1 p)$$

Steady State Simplification: $m + m_T = I_{yy}\dot{q}$

$\dot{\Psi}$ $$\mathcal{N} + \mathcal{N}_T = I_{xz}\dot{P} + I_{zz}\dot{R} + (I_{yy} - I_{xx})PQ - I_{xz}QR$$

$$N_1 + n + N_{T_1} + n_T = I_{xz}\dot{p} + I_{zz}\dot{r} + (I_{yy} - I_{xx})(P_1 + p)(Q_1 + q) - I_{xz}(Q_1 + q)(R_1 + r)$$

$$n + n_T = I_{xz}\dot{p} + I_{zz}\dot{r} + (I_{yy} - I_{xx})(P_1 q + pQ_1) - I_{xz}(Q_1 r + qR_1)$$

Steady State Simplification: $n + n_T = I_{xz}\dot{p} + I_{zz}\dot{r}$

Linearized Force Equations:
$$\begin{cases} -mg\theta cos\Theta_1 + f_x + f_{T_x} = m(\dot{u}) \\ -mg\theta\cos\Theta_1 + f_z + f_{T_z} = m(\dot{w} + U_1 q) \\ mg\theta\cos(\Theta_1) + f_z + f_{T_z} = m(\dot{w} + pV_1 - qU_1) \end{cases}$$

Linearized Moment Equations:
$$\begin{cases} l + l_T = I_{xx}\dot{p} + I_{xz}\dot{r} \\ m + m_T = I_{yy}\dot{q} \\ n + n_T = I_{xz}\dot{p} + I_{zz}\dot{r} \end{cases}$$

Dimensional Stability and Control Derivatives

Aerodynamic Forces in X direction: $\Delta X = q_1 s(-C_{D_u}\frac{u}{U_1} - C_{D_\alpha}\alpha - C_{D_{\delta_e}}\delta_e)$

$$X_u = \frac{1}{m}\frac{\partial X}{\partial u}$$

$$u = -q_1 s C_{D_u}\frac{u}{U_1}$$

$$D1 = q_1 s C_{D_1} D1$$

$$\frac{\partial D_1}{\partial u} = 2q_1 s C_{D_1}\frac{1}{U_1}$$

Thus: $X_u = \frac{1}{m}(-q_1 s\frac{C_{D_u}}{U_1} - 2q_1 s C_{D_1}\frac{1}{U_1}) = \frac{1}{mU_1}[\vec{q}_1 s(-C_{D_u} - 2C_{D_1})$ [1/s]

$$X_\alpha = \frac{1}{m}\frac{dx}{d\alpha}$$

$$\alpha = -q_1 s C_{D_\alpha}\alpha$$

$$L_1 = q_1 s C_{L_1},\ X \approx -D - L\alpha$$

Thus: $X_\alpha = \frac{1}{m}\frac{dx}{da} = \frac{1}{m}[\vec{q}_1 s(-C_{D_\alpha} - C_{l_1})]$ [(ft/s^2)/Rad]

$$X_{\delta e} = \frac{1}{m}\frac{dx}{d\delta_e}$$

$$\delta_e = -q_1 s C_{D_{\delta_e}}\delta_e$$

Thus: $X_{\delta e} = \frac{1}{m}\frac{dx}{d\delta_e} = -\frac{1}{m}[\vec{q}_1 s C_{D_{\delta e}}]$ [(ft/s^2)/Rad]

Aerodynamic Forces in Z direction: $\Delta Z = q_1 s(-C_{L_u}\frac{u}{U_1} - C_{L_\alpha}\alpha - C_{L_{\delta_e}}\delta_e - C_{L_{\dot{\alpha}}}\frac{\dot{\alpha}c}{2U_1})$

$$Z_u = \frac{1}{m}\frac{\partial Z}{\partial u}$$

$$u = -q_1 s C_{D_u}\frac{u}{U_1}$$

$$L_1 = q_1 s C_{L_1}$$

$$\frac{\partial L_1}{\partial u} = 2q_1 s C_{L_1}\frac{1}{U_1}$$

Thus: $Z_u = \frac{1}{mU_1}[\vec{q}_1 s(-C_{l_u} - 2C_{l_1})]$ [1/s]

$$Z_\alpha = \frac{1}{m}\frac{\partial Z}{\partial \alpha}$$

$$\alpha = -q_1 s C_{L_\alpha}\alpha$$

$$D1 = q_1 s C_{D_1} D1 \text{ and } Z \approx -L - D\alpha$$

$Z_\alpha = \frac{1}{m}[\vec{q}_1 s(-C_{l_\alpha} - C_{D_l})]$ [(ft/s^2)/Rad]

$$Z_{\delta e} = \frac{1}{m}\frac{\partial Z}{\partial \delta_e}$$

$$\delta_e = -q_1 s C_{L_{\delta_e}}\delta_e$$

$$Z_{\delta e} = \frac{-1}{m} C_{l_e}\vec{q}_1 s$$

$$Z_{\dot{\alpha}} = \frac{1}{m}\frac{\partial Z}{\partial \dot{\alpha}}$$

$$\dot{\alpha} = \frac{1}{2}\frac{q_1 sc C_{L_{\dot{\alpha}}}}{U_1}$$

Thus: $Z_{\dot{\alpha}} = \frac{-\vec{q}_1 s\vec{c}}{2mu_1} C_{l_{\dot{\alpha}}}$

[(ft/s^2)/Rad]

Aerodynamic Pitching Moment: $\Delta M = q_1 sc$

$$M_u = \frac{1}{I_{yy}}\frac{\partial M}{\partial u}$$

$$u = q_1 s C_{M_u}\frac{u}{U_1}$$

$$M_1 = -q_1 s C_{M_1} \; and \; \frac{\partial M_1}{\partial u} = 2q_1 s C_{M_1}\frac{1}{U_1}$$

Thus: $M_u = \frac{1}{I_{yy}u_1}[\vec{q}_1 s\vec{c}(C_{m_u} + 2C_{m_l})]$

[rads/s^2/ft/s]

$$M_\alpha = \frac{1}{I_{yy}}\frac{\partial M}{\partial \alpha}$$

$$\alpha = q_1 s C_{M_\alpha}\alpha$$

Thus: $$M_\alpha = \frac{\vec{q}_1 s\vec{c}}{I_{yy}} C_{M_\alpha}$$ [rads/s^2/rad]

$$M_{\dot{\alpha}} = \frac{1}{I_{yy}} \frac{\partial M}{\partial \dot{\alpha}} = \frac{\vec{q}_1 s\overrightarrow{c^2}}{2 I_{yy} u_1} C_{M_{\dot{\alpha}}}$$ [rads/s^2/rad/s]

$$M_q = \frac{1}{I_{yy}} \frac{\partial M}{\partial q}$$

$$q = q_1 s c C_{M_q} \frac{qc}{U_1}$$

Thus: $$M_q = \frac{\vec{q}_1 s\overrightarrow{c^2}}{2 I_{yy} u_1} C_{M_q}$$

[rads/s^2/rad/s]

$$M_{\delta_e} = \frac{1}{I_{yy}} \frac{\partial M}{\partial \delta_e} = \frac{\vec{q}_1 s\vec{c}}{I_{yy}} C_{M_{\delta_e}}$$ [rads/s^2/rad]

Longitudinal Linearized Perturbation Equations for straight level flight with constant thrust

$$\begin{cases} \dot{u} = X_u u + X_\alpha \alpha + X_{\delta_e} \delta e - g\theta cos\Theta_1 \\ \dot{\alpha} = q + Z_u \hat{u} + Z_\alpha \alpha + Z_{\delta_e} \delta e + Z_{\dot{\alpha}} \frac{d\alpha}{d\hat{t}} + Z_q \hat{q} - g\theta sin\Theta_1 \\ \dot{q} = M_u \hat{u} + M_\alpha \alpha + M_{\delta_e} \delta e + M_{\dot{\alpha}} \frac{d\alpha}{d\hat{t}} + M_q \hat{q} \\ \dot{\theta} = q \end{cases}$$

For steady flight, assume: $Z_{\dot{\alpha}} = Z_q = 0; \Theta_1 = 0$ substitute terms:

$$\begin{cases} \dot{u} = X_u u + X_\alpha \alpha + X_{\delta_e} \delta e - g\theta cos\Theta_1 \\ \dot{\alpha} = q + \left(\frac{Z_u}{u_1}\right) \hat{u} + \left(\frac{Z_\alpha}{u_1}\right) \alpha + \left(\frac{Z_{\delta_e}}{u_1}\right) \delta e \\ \dot{q} = M_u \hat{u} + M_\alpha \alpha + M_{\delta_e} \delta e + M_{\dot{\alpha}} \left(\frac{Z_u \hat{u} + Z_\alpha \alpha + Z_{\delta_e} \delta e + (1 + Z_q)\hat{q}}{1 - Z_{\dot{\alpha}}} \right) \frac{d\alpha}{d\hat{t}} + M_q \hat{q} \\ \dot{\theta} = q \end{cases}$$

Thus:

$$\begin{bmatrix} \dot{u} \\ \dot{\alpha} \\ \dot{q} \\ \dot{\theta} \end{bmatrix} = \begin{bmatrix} X_u & X_\alpha & 0 & -g \\ \frac{Z_u}{U_1} & \frac{Z_\alpha}{U_1} & 1 & 0 \\ \left(M_u + \frac{M_{\dot{\alpha}} Z_u}{U_1}\right) & \left(M_\alpha + \frac{M_{\dot{\alpha}} Z_u}{U_1}\right) & M_q + M_\alpha & 0 \\ 0 & 0 & 1 & 0 \end{bmatrix} \begin{bmatrix} u \\ \alpha \\ q \\ \theta \end{bmatrix} + \begin{bmatrix} X_{\delta e} \\ \frac{Z_{\delta e}}{U_1} \\ M_{\delta e} + \frac{M_{\dot{\alpha}} Z_{\delta e}}{U_1} \\ 0 \end{bmatrix} \delta_e$$

In State Space: $\dot{\vec{x}} = A\vec{x} + B\vec{u}$ State equation

$\vec{y} = C\vec{x} + D\vec{u}$ Output Equation

Lateral Directional Dynamics and Control

$$Y_{\delta_{\delta a}}\delta_a + Y_{\delta_r}\delta_r = U_1\dot{\beta} - Y_\beta\beta - Y_p p + U_1 r - Yr - g\theta cos\Theta_1$$

$$\dot{p} + \frac{I_{xz}}{I_{xx}}\dot{r} - L_\beta - L_p p - L_r r = L_{\delta_a}\delta_a + L_{\delta_r}\delta_r$$

$$\dot{r} + \frac{I_{xz}}{I_{zz}}\dot{\phi} - N_p p - N_\beta\beta - N_r r = N\delta_a + N_{\delta_r}\delta_r$$

Solve for $\dot{p}$ in the second equation

$$\dot{p} = \frac{-I_{xz}}{I_{xx}}\dot{r} + L_\beta\beta + L_p p + L_r r + L_{\delta_a}\delta_a + L_{\delta_r}\delta_r$$

Substitute $\dot{p}$ into the third equation

$$\dot{r} + \frac{I_{xz}}{I_{zz}}\left(\frac{-I_{xz}}{I_{xx}}\dot{r} + L_\beta\beta + L_p p + L_r r + L_{\delta_a}\delta_a + L_{\delta_r}\delta_r\right) - N_p p - N_\beta\beta - N_r r = N\delta_a + N_{\delta_r}\delta_r$$

$$\dot{r} = \frac{\cancel{I_{xz}}}{\cancel{I_{zz}}}\left(\frac{-\cancel{I_{xz}}}{\cancel{I_{xx}}}\right)\dot{r} - \frac{I_{xz}}{I_{xx}}L_\beta\beta - \frac{\cancel{I_{xz}}}{\cancel{I_{xx}}}L_p p - \frac{\cancel{I_{xz}}}{\cancel{I_{xx}}}L_{\delta_r}\delta_r - \frac{\cancel{I_{xz}}}{\cancel{I_{xx}}}L_{\delta_a}\delta_a + N_\beta\beta + N_p p + N_r r + N\delta_a + N_{\delta_r}\delta_r$$

For conventional aircraft we know that $\frac{I_{xz}}{I_{xx}}$ & $\frac{I_{xz}}{I_{zz}}$ are negligible

Thus:

$$\dot{r} = N_\beta\beta + N_p p + N_r r + N\delta_a + N_{\delta_r}\delta_r$$

$$\dot{p} = L_\beta\beta + L_p p + L_r r + L_{\delta_a}\delta_a + L_{\delta_r}\delta_r$$

$$\begin{cases} \dot{\phi} = p \\ \dot{p} = L_\beta\beta + L_p p + L_r r + L_{\delta_a}\delta_a + L_{\delta_r}\delta_r \\ \dot{\beta} = \dfrac{g\cos\theta}{u_1}\phi + Y_p p + Y_\beta\beta + (Y_r - U_1)r + Y_{\delta_{\delta a}}\delta_a + Y_{\delta_r}\delta_r \\ \dot{\psi} = r \end{cases}$$

$$\begin{bmatrix} \dot{\phi} \\ \dot{p} \\ \dot{\beta} \\ \dot{\psi} \end{bmatrix} = \begin{bmatrix} 0 & 1 & 0 & 0 & 0 \\ 0 & L_P & L_\beta & L_r & 0 \\ \dfrac{g\cos\theta}{u_1} & \dfrac{Y_p}{u_1} & \dfrac{Y_\beta}{u_1} & \dfrac{Y_r}{u_1} - 1 & 0 \\ 0 & N_p & N_\beta & N_r & 0 \\ 0 & 0 & 0 & 1 & 0 \end{bmatrix} \begin{bmatrix} \phi \\ p \\ \beta \\ \psi \end{bmatrix} + \begin{bmatrix} 0 & 0 \\ L_{\delta_r} & L_{\delta_\alpha} \\ \dfrac{Y_{\delta_r}}{u_1} & \dfrac{Y_{\delta_\alpha}}{u_1} \\ 0 & 0 \end{bmatrix} \begin{bmatrix} \delta_r \\ \delta_\alpha \end{bmatrix}$$

State space to transfer function

Given a continuous time, linear time variant system of the equations is in the form:

$$\begin{cases} \dot{\vec{x}} = A\vec{x} + B\vec{u} & \text{State equation with intial condition } \vec{x}(t_0) = \vec{x}_0 \\ \vec{y} = C\vec{x} + D\vec{u} & output\ equation \end{cases}$$

$$I[\dot{x}] = I[A\vec{x} + B\vec{u}] = sX(s) - x(t_0) = AX(s) + BU(s)$$

$$sX(s) - AX(s) = X_0 + BU(S) = \frac{(sI - A)X(s)}{(sI - A)} = \frac{X_0 + BU(s)}{(sI - A)}$$

$$X(s) = (sI - A)^{-1}(X_0 + BU(s))$$

Additionally,

$$I[y] = I[Cx + Du] = Y(s) = CX(s) + DU(s)$$

Substitute X(S) for the equation above:

$$Y(s) = c(sI - A)^{-1}\big(\cancel{X_0} + BU(s)\big) + DU(s)$$

Assume $x_0 = 0$ and D = 0

$$Y(s) = c(sI - A)^{-1}\big(BU(s)\big)$$

Finally:

$$\frac{Y(s)}{U(s)} = C(sI - A)^{-1}B$$

Appendix B: Aileron to Roll Angle Simulation CODE

```
clc; clear all; close all;
g = 32.17405; % [ft/s^2] Earth gravitational acceleration
h = 0; % [ft] sea level altitude
U_1 = 221; % [ft/s]
X_u = -0.0433; % [1/s]
X_alpha = 11.4378; % [ft/s^2]
X_delta_e = 0; % [ft/s^2]
Z_u = -0.272; % [1/s]
Z_alpha = -108.0542; % [ft/s^2]
Z_delta_e = -6.5565; % [ft/s^2]
M_u = 0; % [1/ft/s]
M_alpha = -0.414; % [1/s^2]
M_alphadot = -0.0582;% [1/s]
M_q = -0.3774; % [1/s]
M_delta_e = -0.3997; % [1/s^2]
theta1 = 0;
L_p = -0.9871;
L_beta = -1.2461;
L_r = 0.3834;
L_delta_r = 0;
L_delta_a = 0.235;
Y_p = 0;
Y_beta = -19.664;
Y_r = 0;
Y_delta_r = 3.26;
Y_delta_a = 0;
N_p = -0.1441;
N_beta = 0.2694;
N_r = -0.2338;
N_delta_r = -0.1655;
N_delta_a = 0.0122;
%-----------------------------------------------------------------------
% Longitudinal Open-Loop State-Space Model
A_long = [X_u, X_alpha, 0, -g;
        Z_u/U_1, Z_alpha/U_1, 1, 0;
        M_u + (M_alphadot*Z_u)/U_1, M_alpha + (M_alphadot*Z_alpha)/U_1,...
        M_q + M_alphadot, 0;
        0, 0, 1, 0];
B_long = [X_delta_e; Z_delta_e/U_1; M_delta_e + ...
```

```
        (M_alphadot*Z_delta_e)/U_1; 0];
C_long = [1, 0, 0, 0; 0, 1, 0, 0; 0, 0, 1, 0; 0, 0, 0, 1];
D_long = 0;
OL_long = ss(A_long,B_long,C_long,D_long);
damp(OL_long)
co_long = rank(ctrb(A_long,B_long))
% Lateral/Directional Open-Loop State-Space Model
A_ld = [0, 1, 0, 0, 0;
   0, L_p, L_beta, L_r, 0;
   (g*cos(theta1))/U_1, Y_p/U_1, Y_beta/U_1, (Y_r/U_1)-1, 0;
   0, N_p, N_beta, N_r, 0;
   0, 0, 0, 1, 0];
B_ld = [0, 0;
   L_delta_r, L_delta_a;
   Y_delta_r/U_1, Y_delta_a/U_1;
   N_delta_r, N_delta_a;
   0, 0];
C_ld = [1, 0, 0, 0, 0;
   0, 1, 0, 0, 0;
   0, 0, 1, 0, 0;
   0, 0, 0, 1, 0;
   0, 0 ,0, 0, 1];
D_ld = [0,0;0,0;0,0;0,0;0,0];
OL_ld = ss(A_ld,B_ld,C_ld,D_ld);
tf(OL_ld)
damp(OL_ld)
co_latdir = rank(ctrb(A_ld,B_ld))
%
% From the damping characteristics of the lateral-directional state-space
% system, we find that the system is not stable. There exists a pole at the
% origin, and a positive real pole.
%
% The rank of the controllability matrix indicates that the
% lateral-directional system consisting of five state variables is fully
% controllable.
%--------------------------------------------------------------------------

C_ld_roll = zeros(5,5);
C_ld_roll(1,1) = 1;

latsys = ss(A_ld,B_ld,C_ld_roll,D_ld);
```

```
figure(1)
bode(latsys(1,1),'b');
title('747 Frequency Response for \phi(s)/\delta_a(s)');
set(findall(gcf,'type','line'),'linewidth',2);
set(gcf,'color','w');

tfinal = 60;
figure(2)
impulse(latsys(1,1),tfinal,'b');
title('747 Impulse Response for \phi(s)/\delta_a(s)');
set(findall(gcf,'type','line'),'linewidth',2);
set(gcf,'color','w');


figure(3)
step(latsys(1,1),tfinal,'b');
title('747 Step Response for \phi(s)/\delta_a(s)');
set(findall(gcf,'type','line'),'linewidth',2);
set(gcf,'color','w');
%% Aileron Deflection to Roll Closed Loop Controller

C_ld_roll = [1 0 0 0 0];

D_ld = [0,0];

[num_tf_da2phi,den_tf_da2phi] = ss2tf(A_ld,B_ld,C_ld_roll,D_ld,2)
latsys = ss(A_ld,B_ld,C_ld_roll,D_ld);

tfinal = 40; % [sec]

Ku = 27.1/6.5;
Tu = 7.226;

open_system('b747_da2roll.slx');

%% Ziegler-Nichols
Ti = 0.5*Tu;
Td = 0.125*Tu;
Kp = 0.6*Ku; % Proportional gain
Ki = Kp/Ti; % Integral gain
Kd = Kp*Td; % Derivative gain
```

```
output_zn = sim('b747_da2roll.slx');

%Modified Ziegler-Nichols
Ti = 0.5*Tu;
Td = (1/8)*Tu;
Kp = 0.2*Ku; % Proportional gain
Ki = Kp/Ti; % Integral gain
Kd = Kp*Td; % Derivative gain
output_modzn = sim('b747_da2roll.slx');

%%Tyreus-Luyben
Ti = 2.2*Tu;
Td = Tu/6.3;
Kp = Ku/2.2;
Ki = Kp/Ti; % Integral gain
Kd = Kp*Td; % Derivative gain
output_tl = sim('b747_da2roll.slx');

figure(7)
plot(output_zn.phi.time(:,1),output_zn.phi.signals.values(:,1),'b')
hold on
plot(output_modzn.phi.time(:,1),output_modzn.phi.signals.values(:,1),'r')
hold on
plot(output_tl.phi.time(:,1),output_tl.phi.signals.values(:,1),'g')
hold on
ref_signal = output_tl.ref.getElement(1);
time = ref_signal.Values.Time;
values = ref_signal.Values.Data;
plot(time, values, 'k--')
legend('Ziegler-Nichols','Modified Ziegler-Nichols', 'Tyreus-Luyben','Reference')
xlabel('time [s]');
ylabel('\phi [deg]');
title('Aircraft Roll');
set(gca,'fontsize',12);
set(findall(gcf,'type','line'),'linewidth',3);
set(gcf,'color','w');
%% reference signal
% Extract reference signal from Dataset
ref_signal = output_tl.ref.getElement(1);  % Adjust index if needed
```

```
% Extract time and values
time = ref_signal.Values.Time;
values = ref_signal.Values.Data;

% Plot the signal'
figure()
plot(time, values, 'k--')
xlabel('Time (s)')
ylabel('\phi [deg]')
title('Reference Signal Plot')
grid on
```

Appendix C: Rudder to Yaw Angle Simulation CODE

```
% AE295 Project
%% 747 Longitudinal Data Sea Level
g = 32.17405; % [ft/s^2] Earth gravitational acceleration
h = 0; % [ft] sea level altitude
U_1 = 221; % [ft/s]
X_u = -0.0433; % [1/s]
X_alpha = 11.4738; % [ft/s^2]
X_dele = 0; % [ft/s^2]
Z_u = -0.2720; % [1/s]
Z_alpha = -108.0542; % [ft/s^2]
Z_dele = -6.5565; % [ft/s^2]
M_u = 0.0001; % [1/ft/s]
M_alpha = -0.4140; % [1/s^2]
M_alphadot = -0.0582;% [1/s]
M_q = -0.3774; % [1/s]
M_dele = -0.3997; % [1/s^2]
%% 747 Lateral Data Sea Level
Phi_1 = 0;
L_p = -0.9871 % [1/s]
L_beta = -1.2461; % [1/s^2]
L_r = 0.3834; % [1/s]
L_delr = 0;% [1/s^2]
L_dela = 0.235; % [1/s^2]
Y_p = 0; % [ft/s]
Y_beta = -19.6694; % [ft/s^2]
Y_r = 0; % [ft/s]
```

```
Y_delr = 3.26; % [ft/s^2]
Y_dela = 0;  % [ft/s^2]
N_p = -0.1441; % [1/s]
N_beta = 0.2694; % [1/s^2]
N_r = -0.2338; % [1/s]
N_delr = -0.1655; % [1/s^2]
N_dela = 0.0122; % [1/s^2]
%% Longitudinal Open-Loop State-Space Model
A_long= [X_u, X_alpha, 0, -g; Z_u/U_1, Z_alpha/U_1, 1, 0;...
   (M_u + M_alphadot*Z_u/U_1),...
   (M_alpha + M_alphadot*Z_alpha/U_1), (M_q + M_alphadot), 0;...
   0, 0, 1, 0];
B_long= [X_dele; Z_dele/U_1; (M_dele + M_alphadot*Z_dele/U_1); 0];
C_long_pr= [0, 0, 1, 0]; % third one is q, the pitch rate
D_long= zeros(size(C_long_pr,1),size(B_long,2));
OL_long = ss(A_long,B_long,C_long_pr,D_long);
damp(OL_long)
co_long = rank(ctrb(A_long,B_long));
s= tf("s");
[n_dele2q_Full, d_dele2q_Full]= ...
   ss2tf(A_long,B_long,C_long_pr,D_long);
dele2q_Full= tf(n_dele2q_Full, d_dele2q_Full);
%% Cohen Coon
% https://www.mathworks.com/matlabcentral/fileexchange/
% 46864-automatic-pid-tuning-zip)
G = dele2q_Full;
s = tf([1 0],1);
t1 = 0:0.00001:50;
[y,t] = step(G,t1);
y2p = impulse(G*s,t);
n = length(y2p);
K = y(length(y));
for k = 2:n-1
     if( ( (y2p(k) <= 0) && (y2p(k+1) > 0) ) || ( (y2p(k) >= 0) && (y2p(k+1) < 0) ) )
        p = k+1; % save inflection point
        Mx = t(p);
        My = y(p);
        break
     end
end
```

```
if ((y(p)- y(p-1)) < (y(p+1)-y(p)))
   Mx0 = double(t(p-1));
   My0 = double(y(p-1));
else
   Mx0 = double(t(p+1));
   My0 = double(y(p+1));
end
m = (My-My0)/(Mx-Mx0);
t1 = Mx - My / m;
[y2 i] = min(abs(y-0.63*K));
B = t(i);
L = (t1);
T = B-L;
a = K*L/T;
Kp = (1.5/a)*(1+0.18*T/(1-T));
Ti = L*(2.5-2*T)/(1-0.39*T);
Td = (0.37-0.37*T)*L/(1-0.81*T);
open_system("AE246Project.slx");
CohenCoon= sim("AE246Project.slx");
%% Hagglund and Astrôm
% https://www.mathworks.com/matlabcentral/fileexchange/
% 46864-automatic-pid-tuning-zip)
s = tf([1 0],1);
[Gm, Pm, Wgm, Wpm] = margin(G);
if ((Gm == Inf)||(Wgm == Inf)||(Gm == 0)||(Wgm == 0))
   p = 1/(s+1e-6);
   [Gm Pm Wgm Wpm] = margin(G/s);
   if ((Gm == Inf)||(Wgm == Inf))
       [Gm Pm Wgm Wpm] = margin(G/p^2);
   end
end
rP = Gm;
phiP = Pm*pi/180;
w = Wpm;
% Hagglund and Astrôm, 1988
phiS = -1.0000001;
rS = .1742356660;
phiR = phiS - phiP;
rR = rS/rP;
% Friman and Walter, 1996
Kp = rR*cos(phiR);
```

```
Ti = (2/w)*(tan(phiR) + sqrt(1+tan(phiR)^2));
Td = 1.5*Ti;
open_system("AE246Project.slx");
HagAst= sim("AE246Project.slx");
%% Kappa Tau
% https://www.mathworks.com/matlabcentral/fileexchange/
% 4652-autotunerpid-toolkit
A0 = 3.8;   A1 = -8.4;  A2 = 7.3;
B0 = 5.2;   B1 = -2.5;  B2 = -1.4;
C0 = 0.89;  C1 = -0.37; C2 = -4.1;
D0 = 0.4;   D1 = 0.18;  D2 = 2.8;
a   = m*L/T;            % normalized gain
tau = L/(L+T);          % normalized delay
%
Kp  = A0/a*exp(A1*tau+A2*tau^2);
Ti = L*B0*exp(B1*tau+B2*tau^2);
Td = L*C0*exp(C1*tau+C2*tau^2);
open_system("AE246Project.slx");
KappaTau= sim("AE246Project.slx");
%% Plot
figure
hold on
plot(CohenCoon.qref(:,1),CohenCoon.qref(:,2),"LineWidth",1)
%plot(CohenCoon.q(:,1),CohenCoon.q(:,2),"LineWidth",1)
plot(HagAst.q(:,1),HagAst.q(:,2),"LineWidth",1)
%plot(KappaTau.q(:,1),KappaTau.q(:,2),"LineWidth",1)
legend("Reference","Hagglund Astrom","Cohen Coon","Kappa Tau")
title("Pitch Rate Response to Elevator")
xlabel("Time [s]")
ylabel("Response of System")
xlim([0 10])
ylim([-2.25 1.75])
grid on
hold off
```

Appendix D: Elevator to Pitch Rate Simulation CODE

```
%% 747 Longitudinal Data Sea Level
g = 32.17405; % [ft/s^2] Earth gravitational acceleration
h = 0; % [ft] sea level altitude
U_1 = 221; % [ft/s]
```

```
X_u = -0.0433; % [1/s]
X_alpha = 11.4738; % [ft/s^2]
X_dele = 0; % [ft/s^2]
Z_u = -0.2720; % [1/s]
Z_alpha = -108.0542; % [ft/s^2]
Z_dele = -6.5565; % [ft/s^2]
M_u = 0.0001; % [1/ft/s]
M_alpha = -0.4140; % [1/s^2]
M_alphadot = -0.0582;% [1/s]
M_q = -0.3774; % [1/s]
M_dele = -0.3997; % [1/s^2]
%% 747 Lateral Data Sea Level
Phi_1 = 0;
L_p = -0.9871 % [1/s]
L_beta = -1.2461; % [1/s^2]
L_r = 0.3834; % [1/s]
L_delr = 0;% [1/s^2]
L_dela = 0.235; % [1/s^2]
Y_p = 0; % [ft/s]
Y_beta = -19.6694; % [ft/s^2]
Y_r = 0; % [ft/s]
Y_delr = 3.26; % [ft/s^2]
Y_dela = 0;  % [ft/s^2]
N_p = -0.1441; % [1/s]
N_beta = 0.2694; % [1/s^2]
N_r = -0.2338; % [1/s]
N_delr = -0.1655; % [1/s^2]
N_dela = 0.0122; % [1/s^2]
%% Longitudinal Open-Loop State-Space Model
A_long= [X_u, X_alpha, 0, -g; Z_u/U_1, Z_alpha/U_1, 1, 0;...
   (M_u + M_alphadot*Z_u/U_1),...
   (M_alpha + M_alphadot*Z_alpha/U_1), (M_q + M_alphadot), 0;...
   0, 0, 1, 0];
B_long= [X_dele; Z_dele/U_1; (M_dele + M_alphadot*Z_dele/U_1); 0];
C_long_pr= [0, 0, 1, 0]; % third one is q, the pitch rate
D_long= zeros(size(C_long_pr,1),size(B_long,2));
OL_long = ss(A_long,B_long,C_long_pr,D_long);
damp(OL_long)
co_long = rank(ctrb(A_long,B_long));
s= tf("s");
[n_dele2q_Full, d_dele2q_Full]= ...
```

```
   ss2tf(A_long,B_long,C_long_pr,D_long);
dele2q_Full= tf(n_dele2q_Full, d_dele2q_Full);
%% Hagglund and Astrôm
% https://www.mathworks.com/matlabcentral/fileexchange/
% 46864-automatic-pid-tuning-zip)
s = tf([1 0],1);
[Gm, Pm, Wgm, Wpm] = margin(G);
if ((Gm == Inf)||(Wgm == Inf)||(Gm == 0)||(Wgm == 0))
   p = 1/(s+1e-6);
   [Gm Pm Wgm Wpm] = margin(G/s);
   if ((Gm == Inf)||(Wgm == Inf))
       [Gm Pm Wgm Wpm] = margin(G/p^2);
   end
end
rP = Gm;
phiP = Pm*pi/180;
w = Wpm;
% Hagglund and Astrôm, 1988
phiS = -1.0000000001;
rS = 0;
phiR = phiS - phiP;
rR = rS/rP;
% Friman and Walter, 1996
Kp = rR*cos(phiR);
Ti = (2/w)*(tan(phiR) + sqrt(1+tan(phiR)^2));
Td = 3.5*Ti;
open_system("AE246Project.slx");
HagAst= sim("AE246Project.slx");
%% Plot
figure
hold on
plot(CohenCoon.qref(:,1),CohenCoon.qref(:,2),"LineWidth",1)
%plot(CohenCoon.q(:,1),CohenCoon.q(:,2),"LineWidth",1)
plot(HagAst.q(:,1),HagAst.q(:,2),"LineWidth",1)
%plot(KappaTau.q(:,1),KappaTau.q(:,2),"LineWidth",1)
legend("Reference","Hagglund Astrom","Cohen Coon","Kappa Tau")
title("Pitch Rate Response to Elevator")
xlabel("Time [s]")
ylabel("Response of System")
xlim([0 10])
ylim([-2.25 1.75])
```

```
grid on
hold off
```

Appendix E: Elevator to Angle of Attack Simulation CODE

```
clc; clear all; close all;
g = 32.17405; % [ft/s^2] Earth gravitational acceleration
h = 0; % [ft] sea level altitude
U_1 = 221; % [ft/s]
X_u = -0.0433; % [1/s]
X_alpha = 11.4738; % [ft/s^2]
X_delta_e = 0; % [ft/s^2]
Z_u = -0.272; % [1/s]
Z_alpha = -108.0542; % [ft/s^2]
Z_delta_e = -6.5565; % [ft/s^2]
M_u = 0; % [1/ft/s]
M_alpha = -0.4140; % [1/s^2]
M_alphadot = -0.0582;% [1/s]
M_q = -0.3774; % [1/s]
M_delta_e = -0.3997; % [1/s^2]
%------------------------------------------------------------------------
% Longitudinal Open-Loop State-Space Model
A_long = [X_u                X_alpha                0          -g;...
        Z_u/U_1              Z_alpha/U_1            1           0;...
        M_u+(M_alphadot*Z_u)/U_1   M_alpha+(M_alphadot*Z_alpha)/U_1...
        M_q+M_alphadot     0;...
        0                0                1           0]
B_long = [X_delta_e;...
        Z_delta_e/U_1;...
        M_delta_e+(M_alphadot*Z_delta_e)/U_1;...
        0]
C_long = eye(length(A_long));
C_long_alpha = [0 1 0 0];
D_long = zeros(size(C_long,1),size(B_long,2));
OL_long = ss(A_long,B_long,C_long,D_long);
damp(OL_long);
co_long = rank(ctrb(A_long,B_long));
%------------------------------------------------------------------------
% Longitudinal Dynamic Inversion Control System for Angle of Attack
CBinv = inv(C_long_alpha*B_long);
CA = C_long_alpha*A_long;
```

```
K = 27.12/13;
open('ae295b_747_dyninvsim.slx');
sim = sim('ae295b_747_dyninvsim.slx');
figure,
grid on, hold all
plot(sim.uref(:,1),sim.uref(:,2),'k');
plot(sim.alpha(:,1),sim.alpha(:,2),'r--');
xlabel('Time [s]');
ylabel('Magnitude');
legend('Reference Signal','Closed-Loop Response')
title('Dynamic Inversion 747 Longitudinal Controller Angle of Attack Response')
set(findall(gcf,'type','line'),'linewidth',3);
epsilon = 0.01; % Error Threshold of 0.01 deg, 0.2% of desired 5 deg
for i = 1:length(sim.alpha(:,1))
   if abs(sim.alpha(i,2)-5) < epsilon
      i % Display iteration value
      sim.alpha(i,1) % Display time when alpha is within 0.2%
      break;
   end
end
max(sim.alpha(:,2)) % Calculate maximum value of overshoot
figure,
subplot(2,2,1)
hold on, grid on
plot(sim.u(:,1),sim.u(:,2),'b-');
xlabel('Time [s]');
ylabel('Forward Velocity u [ft/s]');
subplot(2,2,2)
hold on, grid on
plot(sim.alpha1(:,1),sim.alpha1(:,2),'r-');
xlabel('Time [s]');
ylabel('Angle of Attack \alpha [deg]');
subplot(2,2,3)
hold on, grid on
plot(sim.q(:,1),sim.q(:,2),'m-');
xlabel('Time [s]');
ylabel('Pitch Rate q [deg/s]');
subplot(2,2,4)
hold on, grid on
plot(sim.theta(:,1),sim.theta(:,2),'g-');
xlabel('Time [s]');
```

```
ylabel('Pitch Angle \theta [deg]');
set(findall(gcf,'type','line'),'linewidth',3);
sgtitle('747 Longitudinal State-Space System Closed-Loop Response')
figure,
subplot(2,2,1)
hold on, grid on
plot(sim.uOL(:,1),sim.uOL(:,2),'b-');
xlabel('Time [s]');
ylabel('Forward Velocity u [ft/s]');
subplot(2,2,2)
hold on, grid on
plot(sim.alphaOL(:,1),sim.alphaOL(:,2),'r-');
xlabel('Time [s]');
ylabel('Angle of Attack \alpha [deg]');
subplot(2,2,3)
hold on, grid on
plot(sim.qOL(:,1),sim.qOL(:,2),'m-');
xlabel('Time [s]');
ylabel('Pitch Rate q [deg/s]');
subplot(2,2,4)
hold on, grid on
plot(sim.thetaOL(:,1),sim.thetaOL(:,2),'g-');
xlabel('Time [s]');
ylabel('Pitch Angle \theta [deg]');
set(findall(gcf,'type','line'),'linewidth',3);
sgtitle('747 Longitudinal State-Space System Open-Loop Response')
figure,
hold on, grid on
plot(sim.de(:,1),sim.de(:,2),'k-','linewidth',3);
title('Elevator Deflection');
xlabel('Time [s]');
ylabel('Elevator Deflection \delta_e');
```